Precision measurement of the top-quark mass in lepton+jets final states

V. M. Abazov,[31] B. Abbott,[67] B. S. Acharya,[25] M. Adams,[46] T. Adams,[44] J. P. Agnew,[41] G. D. Alexeev,[31] G. Alkhazov,[35] A. Alton,[56,a] A. Askew,[44] S. Atkins,[54] K. Augsten,[7] C. Avila,[5] F. Badaud,[10] L. Bagby,[45] B. Baldin,[45] D. V. Bandurin,[73] S. Banerjee,[25] E. Barberis,[55] P. Baringer,[53] J. F. Bartlett,[45] U. Bassler,[15] V. Bazterra,[46] A. Bean,[53] M. Begalli,[2] L. Bellantoni,[45] S. B. Beri,[23] G. Bernardi,[14] R. Bernhard,[19] I. Bertram,[39] M. Besançon,[15] R. Beuselinck,[40] P. C. Bhat,[45] S. Bhatia,[58] V. Bhatnagar,[23] G. Blazey,[47] S. Blessing,[44] K. Bloom,[59] A. Boehnlein,[45] D. Boline,[64] E. E. Boos,[33] G. Borissov,[39] M. Borysova,[38,l] A. Brandt,[70] O. Brandt,[20] R. Brock,[57] A. Bross,[45] D. Brown,[14] X. B. Bu,[45] M. Buehler,[45] V. Buescher,[21] V. Bunichev,[33] S. Burdin,[39,b] C. P. Buszello,[37] E. Camacho-Pérez,[28] B. C. K. Casey,[45] H. Castilla-Valdez,[28] S. Caughron,[57] S. Chakrabarti,[64] K. M. Chan,[51] A. Chandra,[72] E. Chapon,[15] G. Chen,[53] S. W. Cho,[27] S. Choi,[27] B. Choudhary,[24] S. Cihangir,[45] D. Claes,[59] J. Clutter,[53] M. Cooke,[45,k] W. E. Cooper,[45] M. Corcoran,[72] F. Couderc,[15] M.-C. Cousinou,[12] D. Cutts,[69] A. Das,[71] G. Davies,[40] S. J. de Jong,[29,30] E. De La Cruz-Burelo,[28] F. Déliot,[15] R. Demina,[63] D. Denisov,[45] S. P. Denisov,[34] S. Desai,[45] C. Deterre,[41,c] K. DeVaughan,[59] H. T. Diehl,[45] M. Diesburg,[45] P. F. Ding,[41] A. Dominguez,[59] A. Dubey,[24] L. V. Dudko,[33] A. Duperrin,[12] S. Dutt,[23] M. Eads,[47] D. Edmunds,[57] J. Ellison,[43] V. D. Elvira,[45] Y. Enari,[14] H. Evans,[49] V. N. Evdokimov,[34] A. Fauré,[15] L. Feng,[47] T. Ferbel,[63] F. Fiedler,[21] F. Filthaut,[29,30] W. Fisher,[57] H. E. Fisk,[45] M. Fortner,[47] H. Fox,[39] S. Fuess,[45] P. H. Garbincius,[45] A. Garcia-Bellido,[63] J. A. García-González,[28] V. Gavrilov,[32] W. Geng,[12,57] C. E. Gerber,[46] Y. Gershtein,[60] G. Ginther,[45,63] O. Gogota,[38] G. Golovanov,[31] P. D. Grannis,[64] S. Greder,[16] H. Greenlee,[45] G. Grenier,[17] Ph. Gris,[10] J.-F. Grivaz,[13] A. Grohsjean,[15,c] S. Grünendahl,[45] M. W. Grünewald,[26] T. Guillemin,[13] G. Gutierrez,[45] P. Gutierrez,[67] J. Haley,[68] L. Han,[4] K. Harder,[41] A. Harel,[63] J. M. Hauptman,[52] J. Hays,[40] T. Head,[41] T. Hebbeker,[18] D. Hedin,[47] H. Hegab,[68] A. P. Heinson,[43] U. Heintz,[69] C. Hensel,[1] I. Heredia-De La Cruz,[28,d] K. Herner,[45] G. Hesketh,[41,f] M. D. Hildreth,[51] R. Hirosky,[73] T. Hoang,[44] J. D. Hobbs,[64] B. Hoeneisen,[9] J. Hogan,[72] M. Hohlfeld,[21] J. L. Holzbauer,[58] I. Howley,[70] Z. Hubacek,[7,15] V. Hynek,[7] I. Iashvili,[62] Y. Ilchenko,[71] R. Illingworth,[45] A. S. Ito,[45] S. Jabeen,[45,m] M. Jaffré,[13] A. Jayasinghe,[67] M. S. Jeong,[27] R. Jesik,[40] P. Jiang,[4] K. Johns,[42] E. Johnson,[57] M. Johnson,[45] A. Jonckheere,[45] P. Jonsson,[40] J. Joshi,[43] A. W. Jung,[45] A. Juste,[36] E. Kajfasz,[12] D. Karmanov,[33] I. Katsanos,[59] M. Kaur,[23] R. Kehoe,[71] S. Kermiche,[12] N. Khalatyan,[45] A. Khanov,[68] A. Kharchilava,[62] Y. N. Kharzheev,[31] I. Kiselevich,[32] J. M. Kohli,[23] A. V. Kozelov,[34] J. Kraus,[58] A. Kumar,[62] A. Kupco,[8] T. Kurča,[17] V. A. Kuzmin,[33] S. Lammers,[49] P. Lebrun,[17] H. S. Lee,[27] S. W. Lee,[52] W. M. Lee,[45] X. Lei,[42] J. Lellouch,[14] D. Li,[14] H. Li,[73] L. Li,[43] Q. Z. Li,[45] J. K. Lim,[27] D. Lincoln,[45] J. Linnemann,[57] V. V. Lipaev,[34] R. Lipton,[45] H. Liu,[71] Y. Liu,[4] A. Lobodenko,[35] M. Lokajicek,[8] R. Lopes de Sa,[45] R. Luna-Garcia,[28,g] A. L. Lyon,[45] A. K. A. Maciel,[1] R. Madar,[19] R. Magaña-Villalba,[28] S. Malik,[59] V. L. Malyshev,[31] J. Mansour,[20] J. Martínez-Ortega,[28] R. McCarthy,[64] C. L. McGivern,[41] M. M. Meijer,[29,30] A. Melnitchouk,[45] D. Menezes,[47] P. G. Mercadante,[3] M. Merkin,[33] A. Meyer,[18] J. Meyer,[20,i] F. Miconi,[16] N. K. Mondal,[25] M. Mulhearn,[73] E. Nagy,[12] M. Narain,[69] R. Nayyar,[42] H. A. Neal,[56] J. P. Negret,[5] P. Neustroev,[35] H. T. Nguyen,[73] T. Nunnemann,[22] J. Orduna,[72] N. Osman,[12] J. Osta,[51] A. Pal,[70] N. Parashar,[50] V. Parihar,[69] S. K. Park,[27] R. Partridge,[69,e] N. Parua,[49] A. Patwa,[65,j] B. Penning,[45] M. Perfilov,[33] Y. Peters,[41] K. Petridis,[41] G. Petrillo,[63] P. Pétroff,[13] M.-A. Pleier,[65] V. M. Podstavkov,[45] A. V. Popov,[34] M. Prewitt,[72] D. Price,[41] N. Prokopenko,[34] J. Qian,[56] A. Quadt,[20] B. Quinn,[58] P. N. Ratoff,[39] I. Razumov,[34] I. Ripp-Baudot,[16] F. Rizatdinova,[68] M. Rominsky,[45] A. Ross,[39] C. Royon,[15] P. Rubinov,[45] R. Ruchti,[51] G. Sajot,[11] A. Sánchez-Hernández,[28] M. P. Sanders,[22] A. S. Santos,[1,h] G. Savage,[45] M. Savitskyi,[38] L. Sawyer,[54] T. Scanlon,[40] R. D. Schamberger,[64] Y. Scheglov,[35] H. Schellman,[48] C. Schwanenberger,[41] R. Schwienhorst,[57] J. Sekaric,[53] H. Severini,[67] E. Shabalina,[20] V. Shary,[15] S. Shaw,[41] A. A. Shchukin,[34] V. Simak,[7] P. Skubic,[67] P. Slattery,[63] D. Smirnov,[51] G. R. Snow,[59] J. Snow,[66] S. Snyder,[65] S. Söldner-Rembold,[41] L. Sonnenschein,[18] K. Soustruznik,[6] J. Stark,[11] D. A. Stoyanova,[34] M. Strauss,[67] L. Suter,[41] P. Svoisky,[67] M. Titov,[15] V. V. Tokmenin,[31] Y.-T. Tsai,[63] D. Tsybychev,[64] B. Tuchming,[15] C. Tully,[61] L. Uvarov,[35] S. Uvarov,[35] S. Uzunyan,[47] R. Van Kooten,[49] W. M. van Leeuwen,[29] N. Varelas,[46] E. W. Varnes,[42] I. A. Vasilyev,[34] A. Y. Verkheev,[31] L. S. Vertogradov,[31] M. Verzocchi,[45] M. Vesterinen,[41] D. Vilanova,[15] P. Vokac,[7] H. D. Wahl,[44] M. H. L. S. Wang,[45] J. Warchol,[51] G. Watts,[74] M. Wayne,[51] J. Weichert,[21] L. Welty-Rieger,[48] M. R. J. Williams,[49,n] G. W. Wilson,[53] M. Wobisch,[54] D. R. Wood,[55] T. R. Wyatt,[41] Y. Xie,[45] R. Yamada,[45] S. Yang,[4] T. Yasuda,[45] Y. A. Yatsunenko,[31] W. Ye,[64] Z. Ye,[45] H. Yin,[45] K. Yip,[65] S. W. Youn,[45] J. M. Yu,[56] J. Zennamo,[62] T. G. Zhao,[41] B. Zhou,[56] J. Zhu,[56] M. Zielinski,[63] D. Zieminska,[49] and L. Zivkovic[14]

(D0 Collaboration)

[1]LAFEX, Centro Brasileiro de Pesquisas Físicas, Rio de Janeiro, Brazil
[2]Universidade do Estado do Rio de Janeiro, Rio de Janeiro, Brazil
[3]Universidade Federal do ABC, Santo André, Brazil
[4]University of Science and Technology of China, Hefei, People's Republic of China
[5]Universidad de los Andes, Bogotá, Colombia

[6]*Charles University, Faculty of Mathematics and Physics, Center for Particle Physics, Prague, Czech Republic*

[7]*Czech Technical University in Prague, Prague, Czech Republic*

[8]*Institute of Physics, Academy of Sciences of the Czech Republic, Prague, Czech Republic*

[9]*Universidad San Francisco de Quito, Quito, Ecuador*

[10]*LPC, Université Blaise Pascal, CNRS/IN2P3, Clermont, France*

[11]*LPSC, Université Joseph Fourier Grenoble 1, CNRS/IN2P3, Institut National Polytechnique de Grenoble, Grenoble, France*

[12]*CPPM, Aix-Marseille Université, CNRS/IN2P3, Marseille, France*

[13]*LAL, Université Paris-Sud, CNRS/IN2P3, Orsay, France*

[14]*LPNHE, Universités Paris VI and VII, CNRS/IN2P3, Paris, France*

[15]*CEA, Irfu, SPP, Saclay, France*

[16]*IPHC, Université de Strasbourg, CNRS/IN2P3, Strasbourg, France*

[17]*IPNL, Université Lyon 1, CNRS/IN2P3, Villeurbanne, France and Université de Lyon, Lyon, France*

[18]*III. Physikalisches Institut A, RWTH Aachen University, Aachen, Germany*

[19]*Physikalisches Institut, Universität Freiburg, Freiburg, Germany*

[20]*II. Physikalisches Institut, Georg-August-Universität Göttingen, Göttingen, Germany*

[21]*Institut für Physik, Universität Mainz, Mainz, Germany*

[22]*Ludwig-Maximilians-Universität München, München, Germany*

[23]*Panjab University, Chandigarh, India*

[24]*Delhi University, Delhi, India*

[25]*Tata Institute of Fundamental Research, Mumbai, India*

[26]*University College Dublin, Dublin, Ireland*

[27]*Korea Detector Laboratory, Korea University, Seoul, Korea*

[28]*CINVESTAV, Mexico City, Mexico*

[29]*Nikhef, Science Park, Amsterdam, the Netherlands*

[30]*Radboud University Nijmegen, Nijmegen, the Netherlands*

[31]*Joint Institute for Nuclear Research, Dubna, Russia*

[32]*Institute for Theoretical and Experimental Physics, Moscow, Russia*

[33]*Moscow State University, Moscow, Russia*

[34]*Institute for High Energy Physics, Protvino, Russia*

[35]*Petersburg Nuclear Physics Institute, St. Petersburg, Russia*

[36]*Institució Catalana de Recerca i Estudis Avançats (ICREA) and Institut de Física d'Altes Energies (IFAE), Barcelona, Spain*

[37]*Uppsala University, Uppsala, Sweden*

[38]*Taras Shevchenko National University of Kyiv, Kiev, Ukraine*

[39]*Lancaster University, Lancaster LA1 4YB, United Kingdom*

[40]*Imperial College London, London SW7 2AZ, United Kingdom*

[41]*The University of Manchester, Manchester M13 9PL, United Kingdom*

[42]*University of Arizona, Tucson, Arizona 85721, USA*

[43]*University of California Riverside, Riverside, California 92521, USA*

[44]*Florida State University, Tallahassee, Florida 32306, USA*

[45]*Fermi National Accelerator Laboratory, Batavia, Illinois 60510, USA*

[46]*University of Illinois at Chicago, Chicago, Illinois 60607, USA*

[47]*Northern Illinois University, DeKalb, Illinois 60115, USA*

[48]*Northwestern University, Evanston, Illinois 60208, USA*

[49]*Indiana University, Bloomington, Indiana 47405, USA*

[50]*Purdue University Calumet, Hammond, Indiana 46323, USA*

[51]*University of Notre Dame, Notre Dame, Indiana 46556, USA*

[52]*Iowa State University, Ames, Iowa 50011, USA*

[53]*University of Kansas, Lawrence, Kansas 66045, USA*

[54]*Louisiana Tech University, Ruston, Louisiana 71272, USA*

[55]*Northeastern University, Boston, Massachusetts 02115, USA*

[56]*University of Michigan, Ann Arbor, Michigan 48109, USA*

[57]*Michigan State University, East Lansing, Michigan 48824, USA*

[58]*University of Mississippi, University, Mississippi 38677, USA*

[59]*University of Nebraska, Lincoln, Nebraska 68588, USA*

[60]*Rutgers University, Piscataway, New Jersey 08855, USA*

[61]*Princeton University, Princeton, New Jersey 08544, USA*

[62]*State University of New York, Buffalo, New York 14260, USA*

[63]*University of Rochester, Rochester, New York 14627, USA*
[64]*State University of New York, Stony Brook, New York 11794, USA*
[65]*Brookhaven National Laboratory, Upton, New York 11973, USA*
[66]*Langston University, Langston, Oklahoma 73050, USA*
[67]*University of Oklahoma, Norman, Oklahoma 73019, USA*
[68]*Oklahoma State University, Stillwater, Oklahoma 74078, USA*
[69]*Brown University, Providence, Rhode Island 02912, USA*
[70]*University of Texas, Arlington, Texas 76019, USA*
[71]*Southern Methodist University, Dallas, Texas 75275, USA*
[72]*Rice University, Houston, Texas 77005, USA*
[73]*University of Virginia, Charlottesville, Virginia 22904, USA*
[74]*University of Washington, Seattle, Washington 98195, USA*

We measure the mass of the top quark in lepton + jets final states using the full sample of $p\bar{p}$ collision data collected by the D0 experiment in Run II of the Fermilab Tevatron Collider at $\sqrt{s} = 1.96$ TeV, corresponding to 9.7 fb^{-1} of integrated luminosity. We use a matrix element technique that calculates the probabilities for each event to result from $t\bar{t}$ production or background. The overall jet energy scale is constrained *in situ* by the mass of the W boson. We measure $m_t = 174.98 \pm 0.76$ GeV. This constitutes the most precise single measurement of the top-quark mass.

I. INTRODUCTION

Since the discovery of the top quark [1,2], the determination of its properties has been one of the main goals of the Fermilab Tevatron Collider and also, more recently, of the CERN Large Hadron Collider (LHC). The measurement of the top-quark mass m_t, a fundamental parameter of the standard model (SM), has received particular attention, since m_t, the mass of the W boson, M_W, and the mass of the Higgs boson are related through radiative corrections that provide

an internal consistency check of the SM [3]. Furthermore, m_t dominantly affects the stability of the SM Higgs potential, which has cosmological implications [4–6].

The world-average $m_t = 173.34 \pm 0.76$ GeV has reached a precision of about 0.5% [7–9], which has been limited for some time by systematic uncertainties. The main systematic uncertainties arise from the calibration of the jet energy scale (JES) and the modeling of $t\bar{t}$ events in Monte Carlo (MC) simulations.

In this manuscript, we present a measurement of m_t based on the full set of $p\bar{p}$ data at $\sqrt{s} = 1.96$ TeV recorded by the D0 detector in Run II of the Fermilab Tevatron Collider, corresponding to an integrated luminosity of 9.7 fb^{-1}. The analysis focuses on $t\bar{t}$ events identified in ℓ + jets final states with ℓ representing either an electron or a muon. This includes contributions from leptonic $\tau \to \ell \nu_\ell \nu_\tau$ decays. The top and antitop quark are assumed to always decay into a W boson and a b quark [10]. Thus, at leading order (LO) in perturbative quantum chromodynamics (QCD), one of the W bosons in the $W^+W^-b\bar{b}$ final state decays into a charged lepton and a neutrino, while the other decays into a pair of quarks, and all four quarks $(q\bar{q}'b\bar{b})$ evolve into jets. Such ℓ + jets events are characterized by an isolated electron or muon with large transverse momentum p_T, a large imbalance in transverse momentum caused by the undetected neutrino, and four high-p_T jets. We exploit this distinct signature in the event selection to discriminate $t\bar{t}$ events from background.

To extract the value of m_t, we utilize a matrix element (ME) technique that determines the probability of observing an event under both the $t\bar{t}$ signal and background hypotheses described by the relevant ME [11]. The overall JES is calibrated *in situ* through a constant factor k_{JES} by

taking into account all the kinematic information in a given event, while constraining the reconstructed invariant mass of the $W \rightarrow q\bar{q}'$ decay products to $M_W = 80.4$ GeV [12].

We provide a detailed description of the measurement that was presented previously in a Letter [13], and is an update and supersedes a previous D0 measurement of $m_t = 174.94 \pm 1.14(\text{stat} + \text{JES}) \pm 0.96(\text{syst})$ GeV [14] using 3.6 fb^{-1} of integrated luminosity. In the present measurement, we use not only a larger data sample to improve the statistical precision, but also refine the estimation of systematic uncertainties, resulting in a reduction of the uncertainty by 50%. This improvement is achieved through an updated detector calibration, in particular through improvements to b quark JES corrections [15] and through the use of recent improvements in modeling the $t\bar{t}$ signal. In the following, we point out the most important improvements of this analysis with respect to the previous measurement. The analysis is performed "blinded," i.e., with no reference to the resulting m_t, until the final approval of the analysis methodology.

As in all direct measurements of m_t, this analysis relies on simulated $t\bar{t}$ MC events, which are used for the absolute calibration of the response of the ME technique. Therefore, the extracted m_t corresponds to the generated m_t^{gen} parameter implemented in the LO MC event generator used to simulate $t\bar{t}$ events, which in our case is ALPGEN [16]. Although m_t^{gen} is not well defined at LO, it is expected to correspond within ≈ 1 GeV to the m_t defined in the pole-mass scheme [17]. There is currently no universal MC event generator available for simulating $t\bar{t}$ events at next-to-leading order (NLO) that includes the effects of parton showering and hadronization. Programs such as MC@NLO [18] or POWHEG [19], commonly referred to as NLO generators, simulate only the $q\bar{q} \rightarrow t\bar{t}$, $gg \rightarrow t\bar{t}$, and $qg \rightarrow t\bar{t}$ processes at NLO, whereas the decays of the top quark are simulated at LO through the narrow-width approximation.

This manuscript is arranged as follows. A brief description of the D0 detector is given in Sec. II, which is followed in Sec. III by a summary of simulations used to model signal and background events. The selection of $t\bar{t}$ candidate events is reviewed and the sample composition presented in Sec. IV. Section V discusses the ME technique used to extract m_t, with particular emphasis placed on the improvements since the previous publication [14]. This is followed in Sec. VI by the description of the measurement of the signal fraction f in data using the ME technique, including its calibration. The measurement of m_t and the calibration of the response of the ME technique in m_t is discussed in Sec. VII. After describing the evaluation of systematic uncertainties in Sec. VIII, we compare our measurement with previous results in Sec. IX, and conclude and give the final result with statistical and systematic uncertainties in Sec. X. Appendix A discusses the issue of initial and final state radiation, and Appendix B summarizes the parametrization of the detector response through transfer functions.

II. THE D0 DETECTOR

The D0 detector [20,21] contains a magnetic central tracking system, calorimetry, and a muon system. The central tracking system comprises a silicon microstrip tracker (SMT) and a central fiber tracker (CFT), both located within a 2 T superconducting solenoidal magnet. The SMT [22] has $\approx 800\,000$ individual strips, with typical pitch of 50–80 μm, and a design optimized for track and vertex finding within $|\eta| < 2.5$ [23]. The system has a six-barrel longitudinal structure, each with a set of four layers arranged axially around the beam pipe, and interspersed with radial disks. In 2006, a fifth layer, referred to as Layer 0, was installed close to the beam pipe [24]. The CFT has eight thin coaxial barrels, each supporting two doublets of overlapping scintillating fibers of 0.835 mm diameter, one doublet being parallel to the collision axis, and the other alternating by $\pm 3°$ relative to the axis. Light signals are transferred via clear fibers to solid-state visible-light photon counters (VLPCs) that have $\approx 80\%$ quantum efficiency.

Central and forward preshower detectors, located just outside of the superconducting coil (in front of the calorimetry), are constructed of several layers of extruded triangular scintillator strips that are read out using wave-length-shifting fibers and VLPCs. These detectors provide initial sampling of electromagnetic showers, and thereby help distinguish between incident electrons and jets. The next layer of detection involves three liquid-argon/uranium calorimeters: a central section (CC) covering up to $|\eta| \approx 1.1$, and two end calorimeters (EC) that extend coverage to $|\eta| \approx 4.2$, housed in separate cryostats. The electromagnetic (EM) section of the calorimeter is segmented into four layers, with transverse segmentation of the cells in pseudorapidity and azimuth of $\Delta\eta \times \Delta\phi = 0.1 \times 0.1$, except for the third layer, where the segmentation is 0.05×0.05. The hadronic portion of the calorimeter is located after the EM sections and consists of fine hadron-sampling layers, followed by more coarse hadronic layers. In addition, scintillators between the CC and EC cryostats provide sampling of developing showers for $1.1 < |\eta| < 1.4$.

A muon system [25] is located beyond the calorimetry, and consists of a layer of tracking detectors and scintillation trigger counters before 1.8 T iron toroid magnets, followed by two similar layers after the toroids. Tracking for $|\eta| < 1$ relies on 10 cm wide drift tubes, while 1 cm mini-drift tubes are used for $1 < |\eta| < 2$.

Luminosity is measured using plastic scintillator arrays located in front of the EC cryostats, covering $2.7 < |\eta| < 4.4$. The trigger and data acquisition systems are designed to accommodate the high instantaneous luminosities of the Tevatron [20,26]. Based on coarse information from tracking, calorimetry, and muon systems, the output of the first level of the trigger is used to limit the rate for accepted events to ≈ 2 kHz. At the next trigger

stage, with more refined information, the rate is reduced further to ≈ 1 kHz. These first two levels of triggering rely mainly on hardware and firmware. The third and final level of the trigger, with access to all of the event information, uses software algorithms and a computing farm, and reduces the output rate to ≈ 100 Hz, which is recorded.

III. THE DATA SAMPLE AND SIMULATIONS

The sample of $p\bar{p}$ collision data considered in this analysis was collected between April 2002 and September 2011 in Run II of the Fermilab Tevatron Collider. The sample is split into four data-taking epochs: "Run IIa", "Run IIb1", "Run IIb2", and "Run IIb3" corresponding to 1.1 fb^{-1}, 1.2 fb^{-1}, 3.0 fb^{-1}, and 4.4 fb^{-1} of integrated luminosity, respectively, after implementation of data-quality requirements. All MC simulations are split accordingly into epochs to model variations in the response of the detector, such as the insertion of Layer 0 into the SMT detector between Run IIa and Run IIb1 [24], and the dependence of the track reconstruction efficiency on instantaneous luminosity [27].

Simulated MC events for $t\bar{t}$ signal and the dominant $W +$ jets background, which are used to verify the agreement between data and simulations and to calibrate the measurement (described in Secs. VI A and VII A), are generated using the MC generator ALPGEN [16] to simulate the hard-scattering process with up to five additional partons, and PYTHIA [28,29] to simulate hadronization and shower evolution. The MLM matching scheme [30] is employed to avoid overlaps between components of the event belonging to the hard process, implemented through a ME, and parton evolution (showering) into jets. The $W +$ jets background samples are divided into two categories: (i) $W +$ hf which represents $W + c\bar{c}$ and $W + b\bar{b}$ production, possibly in association with u, d, s quarks, or gluons, and (ii) $W +$ lf which represents all other flavor configurations. The cross section for the $W +$ jets contribution provided by ALPGEN is multiplied by a factor of 1.3 to match the NLO calculations of the MCFM MC generator [31]. In addition, the heavy-flavor contributions of category (i) are multiplied by a factor of 1.47, using the same calculations.

We also consider other small background contributions on the order of few percent to improve the agreement between data and simulations. The $Z +$ jets background is simulated in the same way as $W +$ jets with ALPGEN, taking into account contributions from $Z +$ hf production, with rates normalized to NLO calculations [31]. PYTHIA is used to simulate diboson (WW, WZ, or ZZ) production, while COMPHEP + PYTHIA [32] is used for single top quark processes that are simulated for $m_t = 172.5$ GeV. The hard-scattering process for all signal and background MC samples is simulated using the CTEQ6L1 set of parton distribution functions (PDF), except for COMPHEP, which uses the NLO CTEQ6M set [33]. More details on the

MC simulations and their normalization can be found in Ref. [34].

The simulation of parton showers with PYTHIA uses tune A in combination with the CTEQ6L1 PDF set and with $\Lambda_{QCD} = 0.26$ GeV, also referred to as "D0 tune A". The detector response is fully simulated through GEANT3 [35]. To simulate the effects from additional $p\bar{p}$ interactions (pileup), events taken with minimal trigger requirements, selected from random $p\bar{p}$ crossings at the same instantaneous luminosity as the data, are overlaid on the fully simulated MC events. These events are then reconstructed using the same algorithms as used on data.

Events from multijet (MJ) production can pass our selection criteria, which happens typically when a jet mimics an electron or when a muon arising from semi-leptonic decay of a b or c quark appears isolated. The kinematic distributions from the MJ background are modeled using data events for which lepton isolation requirements are inverted. The absolute contribution of this background to each of the $e +$ jets and $\mu +$ jets final states is estimated using the "matrix method," described in Ref. [34]. This method uses the number of events with leptons originating from the hard interaction, $N_{\text{loose}}^{t\bar{t},W}$, and from MJ production, $N_{\text{loose}}^{\text{MJ}}$, both with less restrictive lepton-identification criteria, and relates them to the contributions to the sample of events that fulfil standard lepton identification criteria. This is calculated using the relation $N = \varepsilon^{t\bar{t},W} N_{\text{loose}}^{t\bar{t},W} + \varepsilon^{\text{MJ}} N_{\text{loose}}^{\text{MJ}}$, where $\varepsilon^{t\bar{t},W}$ and ε^{MJ} represent the efficiency of events that pass the loosened lepton identification criteria to also pass the standard identification criteria. The parameters $\varepsilon^{t\bar{t},W}$ and ε^{MJ} are measured, respectively, in control regions dominated by leptons originating from the hard interaction and by MJ events.

IV. EVENT SELECTION AND SAMPLE COMPOSITION

The trigger selects $\ell +$ jets events by requiring either at least one lepton (electron or muon), or at least one lepton and at least one jet, resulting in an efficiency of 95% for $t\bar{t}$ candidate events containing an electron and 80% for events containing a muon, before any offline selections are applied.

Selected $t\bar{t}$ candidate events are required to have at least one primary $p\bar{p}$ collision vertex (PV) with three or more tracks reconstructed within 60 cm of the center of the detector in the coordinate along the beam axis. In addition, there must be exactly four jets with $p_T > 20$ GeV within $|\eta| < 2.5$, with the leading jet further satisfying $p_T > 40$ GeV. Jets are reconstructed using an iterative cone algorithm [36] with a cone parameter of $R_{\text{cone}} = 0.5$. Jet energies are corrected to the particle level using calibrations derived from exclusive $\gamma +$ jet, $Z +$ jet, and dijet events [15]. These calibrations account for differences in detector response to jets originating from a gluon, a b quark, or u, d, s, and c quarks. Furthermore, we require the presence

TABLE I.   A summary of kinematic event selections.

One charged lepton	$p_T > 20$ GeV	$\vert\eta\vert < 1.1$ (e)
		$\vert\eta\vert < 2.0$ (μ)
Four jets	$p_T > 20$ GeV	$\vert\eta\vert < 2.5$
Jet with highest p_T	$p_T > 40$ GeV	$\vert\eta\vert < 2.5$
Imbalance in transverse momentum	$\not{p}_T > 20$ GeV	

of one isolated electron [37] or muon [27] with transverse momentum $p_T > 20$ GeV and $\vert\eta\vert < 1.1$ or $\vert\eta\vert < 2$, respectively. The electrons and muons are required to originate from within 1 cm of the PV in the coordinate along the beam axis and to be separated in $\Delta R \equiv \sqrt{(\Delta\eta)^2 + (\Delta\phi)^2}$ from the closest jet by $\Delta R > 0.5$, where $\Delta\eta$ is the difference in pseudorapidity and $\Delta\phi$ in azimuth (in rad) between the lepton and the jet. At least one neutrino is expected in the ℓ + jets final state, and an imbalance in transverse momentum of $\not{p}_T > 20$ GeV is required. The $\not{p}_T$ variable is defined as the opposite of the vector sum of the transverse energies in each calorimeter cell, corrected for the energy carried by identified muons and after applying the jet energy scale calibration. The kinematic selections are summarized in Table I.

Events containing an additional isolated charged lepton, i.e., an electron with $p_T > 10$ GeV and $\vert\eta\vert < 2.5$ or a muon with $p_T > 10$ GeV and $\vert\eta\vert < 2$, are rejected. In addition, any μ + jets events with an invariant mass $M_{\mu\mu}$ of the isolated muon and a second *loosely* isolated muon with $p_T > 15$ GeV within $70 < M_{\mu\mu} < 110$ GeV are rejected to suppress Z + jets events.

To reject μ + jets events where the momentum of the muon has been mismeasured, we require $\not{p}_T < 250$ GeV and $M_T^W < 250$ GeV, where M_T^W is the transverse mass of the W boson [38]. To further reduce contributions from such events, which is found at the % level, we use additional requirements on the significance of the curvature of the muon track, S_κ. It is defined as the curvature $\kappa \equiv 1/p_T$ divided by its uncertainty, where Q is the electric charge of the muon. We reject events with muons within one or both of the two regions where they are likely to be mismeasured, $S_\kappa < \Delta\phi(\mu, \not{p}_T) \times 25.5$–70 or $S_\kappa < \Delta\phi(\mu, \not{p}_T) \times 4.4 + 8.8$, where $\phi(\mu, \not{p}_T)$ is the difference in azimuth between the muon momentum and the direction of $\not{p}_T$.

To reduce the contribution from MJ production caused by the misidentification of a quark or gluon jet as a lepton, which changes the calculated $\not{p}_T$, we require $\Delta\phi(\ell, \not{p}_T) > 0.5$. Additional reduction of the MJ background is achieved by requiring $\Delta\phi(e, \not{p}_T) > 2.2 - \not{p}_T \times 0.045$ GeV^{-1} in the e + jets final state and $\Delta\phi(\mu, \not{p}_T) > 2.1 - \not{p}_T \times 0.035$ GeV^{-1} in the μ + jets final state.

Since two b-quark jets are expected in the final state, at least one jet per event is required to be tagged as originating from a b quark (b-tagged) through the use of a multivariate

algorithm [39]. The tagging efficiency in this analysis is $\approx 65\%$ for b-quark jets, while the mistag rate for gluons and for u, d, s quark jets is $\approx 5\%$.

We select 1502 events in the e + jets final state in data, while 1286 are selected in the μ + jets final state. To verify that the simulations agree with the data following all selections, we use the NNLO calculation, including next-to-next-to-leading-logarithmic (NNLL) corrections [40], to normalize the $t\bar{t}$ signal. The contribution from W + jets events is adjusted to normalize the absolute yield from our signal and background models to data before applying b jet identification criteria. The relative yields of contributions from $W + (b\bar{b}, n$lp) and $W + (c\bar{c}, n$lp) production and contributions from $W + n$lp production are further adjusted using data, as described in Ref. [34]. The number of observed events is compared to expectations in Table II, considering statistical uncertainties only.

The distribution in the invariant mass $m_{t\bar{t}}$ of the $t\bar{t}$ system is shown in Figs. 26(a) and 26(b) in Sec. VII C, together with predictions from our signal and background models. The distribution is generated with a mass of the top quark of $m_t^{\text{gen}} = 172.5$ GeV. The mass $m_{t\bar{t}}$ is constructed using $\not{p}_T$ as an initial estimate for p_T^ν of the neutrino, assuming $M_W = 80.4$ GeV, and solving the resulting quadratic equation for p_z^ν. When no solution exists, $\not{p}_T$ is scaled to obtain a solution. The resulting neutrino momentum is then combined with the momenta of the four jets and the charged lepton to obtain $m_{t\bar{t}}$. The invariant mass, M_W, of the two jets that match one of the W bosons is presented in Figs. 27(a) and 27(b) in Sec. VII C. The reconstruction of M_W in Fig. 27 is unique for events with two b-tagged jets, as the two other jets are assigned to the W boson. If only one jet is b-tagged, all possible assignments of jets to partons in the LO approximation of $t\bar{t}$ decays are tried, and the one yielding the smallest value of $\vert m_t - m_{\bar{t}}\vert$ is retained. If the b-tagged jet is matched to the top quark decaying into

TABLE II.   Comparison of the number of observed data events after all selections with the expectation from simulations, assuming $\sigma_{t\bar{t}} = 7.24$ pb^{-1} [40] and using $m_t^{\text{gen}} = 172.5$ GeV. The category "other backgrounds" encompasses Z + jets, WW, WZ, ZZ, and single top quark production, as well as dileptonic $t\bar{t}$ decays. The production of a W boson in association with at least one b or c quark is denoted as "W + hf", while "W + lf" stands for all other flavor configurations. The uncertainties are purely statistical.

Contribution	e + jets	μ + jets
$t\bar{t}$	918.1 ± 3.6	824.9 ± 3.5
Other backgrounds	97.8 ± 0.5	79.2 ± 0.9
W + hf	126.0 ± 2.1	162.2 ± 2.8
W + lf	77.9 ± 2.1	101.0 ± 2.9
Multijet	144.4 ± 24.2	48.2 ± 16.1
Expected	1364.1 ± 24.7	1215.5 ± 17.0
Observed	**1502**	**1286**

three jets, the two untagged jets matched to the same top quark form the W boson. If all three jets that are matched to this top quark are not b-tagged, the two lowest p_T jets are matched to the W boson. A similar matching algorithm is used if there are more than two b-tagged jets. The uncertainties in the predictions include the dominant sources of systematic uncertainty that change the shape of the kinematic distributions: JES, jet energy resolution, jet identification, flavor dependence of the detector response, b tagging, lepton identification, lepton momentum scale, trigger, as well as hadronization and higher-order effects for simulated $t\bar{t}$ events. Good agreement is observed between data and simulations. We verify that the agreement improves using the values for the signal fraction f, m_t, and k_{JES} measured in this analysis, as shown in Sec. VII C.

V. ANALYSIS METHOD

The extraction of m_t is based on the full kinematic and topological information in the event, and is performed through a likelihood technique using probability densities (PDs) for each event, described by the ME of the processes contributing to the observed events.

A. Matrix element technique

The ME technique was first suggested by Kondo [41], and was experimentally applied for the first time at the Tevatron in the measurement of m_t [11], and later in the determination of the helicity of the W boson [42] and in the first evidence obtained for production of single top quarks [43,44].

Assuming two noninterfering contributing processes, $t\bar{t}$ and W + jets production, the per-event PD is

$$P_{\text{evt}} = A(\vec{x})[fP_{\text{sig}}(\vec{x}; m_t, k_{\text{JES}}) + (1-f)P_{\text{bkg}}(\vec{x}; k_{\text{JES}})], \quad (1)$$

where the observed parameters f, m_t, and k_{JES}, are to be determined from data, $\vec{x}$ [45] represents a vector of the measured four-momenta of the four jets and the charged lepton, but not $\not{p}_T$ due to its limited experimental resolution, and $A(\vec{x})$ accounts for acceptance and efficiencies. The function P_{sig} describes the PD for $t\bar{t}$ production, while P_{bkg} describes the PD for W + jets production. W + jets events, i.e., the sum of W + hf and W + lf categories in Table II, represent the dominant background contribution of 14% in the e + jets and 20% in the μ + jets final states, derived with the normalization procedure described in Sec. IV. The next-to-dominant background contribution is from MJ events. It is accounted for in P_{evt} through P_{bkg}, since W + jets and MJ production have similar PDs in the selected kinematic region. The similarity of PDs for W + jets and MJ production can be understood in that the main difference between the two processes arises from the presence of the W boson in the W + jets production, while an energetic jet which is misidentified as an isolated lepton is present in MJ production. At the same time, both processes are characterized by the presence of four additional jets, which, together with the W boson for W + jets production or the jet misidentified as an isolated lepton for MJ production, set a similar momentum-transfer scale of the hard interaction process. The effect of including MJ production through P_{bkg} is accounted for by the calibration procedure outlined in Secs. VI and VII. The combined contribution from all other backgrounds amounts to about 6% in both final states (cf. Table II), and is therefore not included in the calculation of P_{evt}.

B. The signal probability

The probability density for $t\bar{t}$ production to yield a given set of partonic final-state four-momenta $\vec{y}$ [45] in the hard scattering of two massless quarks with four-momenta q_1 and q_2 is proportional to the differential cross section $d\sigma$ of the corresponding process, given by

$$d\sigma_{q\bar{q}\to t\bar{t}}(\vec{y}; m_t) = \frac{(2\pi)^4 |\mathcal{M}_{q\bar{q}\to t\bar{t}}|^2}{2g_{\mu\nu}q_1^\mu q_2^\nu} d\Phi_6, \quad (2)$$

where $\mathcal{M}_{q\bar{q}\to t\bar{t}}$ denotes the ME for the $q\bar{q} \to t\bar{t} \to b(\ell\nu)\bar{b}(q\bar{q}')$ process, $g_{\mu\nu}$ is the tensor of the Minkowski metric, and $d\Phi_6$ is an infinitesimal element of six-body phase space.

To obtain the differential cross section in $p\bar{p}$ collisions, the expression in Eq. (2) is convoluted with the corresponding PD for all possible flavor combinations of the colliding quark and antiquark, yielding

$$d\sigma_{p\bar{p}\to t\bar{t}}(\vec{y}; m_t) = \sum_{\substack{\text{quark} \\ \text{flavors } \vec{q}_1, \vec{q}_2}} \int d\vec{q}_1 d\vec{q}_2 f(\vec{q}_1)f(\vec{q}_2) \times d\sigma_{q\bar{q}\to t\bar{t}}(\vec{y}; m_t).$$

$$(3)$$

The longitudinal momentum PDFs, $f(q_{i,z})$, are taken from CTEQ6L1 [33], while the dependence of $f(q_{i,\text{x}})$ and $f(q_{i,\text{y}})$ on transverse momentum is taken from the PD in the PYTHIA simulation. Only quark-antiquark annihilation at LO is taken into account in $\mathcal{M}_{q\bar{q}\to t\bar{t}}$, and the differential cross section $d\sigma_{p\bar{p}\to t\bar{t}}$ therefore does not represent the full differential cross section for $t\bar{t}$ production in $p\bar{p}$ collisions. Effects from gluon-gluon and quark-gluon induced $t\bar{t}$ production, accounting for about 15% of the cross section, as well as from higher-order corrections from real emissions, are accounted for in the calibration procedure described in Secs. VI A and VII A.

In general, the set $\vec{x}$ of measured four-momenta is not identical to the set of corresponding partonic variables $\vec{y}$ because of finite detector resolution and the evolution of quarks into jets. As will be discussed in Sec. V D, this is taken into account through the transfer function (TF) $W(\vec{x}, \vec{y}, k_{\text{JES}})$, representing the probability density for the

measured set $\vec{x}$ to have arisen from the partonic set $\vec{y}$. Thus, the probability to observe a given reconstructed $t\bar{t}$ event characterized by $\vec{x}$ is obtained through a convolution with the TF in the calculation of the differential cross section

$$
\mathrm{d}\sigma_{p\bar{p}\to t\bar{t}}(\vec{x}; m_t, k_{\mathrm{JES}}) = \int_{\vec{y}} \mathrm{d}\vec{y}\mathrm{d}\sigma_{p\bar{p}\to t\bar{t}}(\vec{y}; m_t)
$$
$$
\times W(\vec{x}, \vec{y}; k_{\mathrm{JES}}). \qquad (4)
$$

The PD to observe a $t\bar{t}$ event with a set of kinematic quantities $\vec{x}$ observed in the detector is given by

$$
P_{\mathrm{sig}}(\vec{x}; m_t, k_{\mathrm{JES}}) = \frac{\mathrm{d}\sigma_{p\bar{p}\to t\bar{t}}(\vec{x}; m_t, k_{\mathrm{JES}})}{\sigma_{p\bar{p}\to t\bar{t},\mathrm{obs}}(m_t, k_{\mathrm{JES}})}, \qquad (5)
$$

where the total cross section for $t\bar{t}$ production observed in the detector, defined as

$$
\sigma_{p\bar{p}\to t\bar{t},\mathrm{obs}}(m_t, k_{\mathrm{JES}}) = \int_{\vec{x}} \mathrm{d}\vec{x}A(\vec{x})\mathrm{d}\sigma_{p\bar{p}\to t\bar{t}}(\vec{x}; m_t, k_{\mathrm{JES}}), \quad (6)
$$

ensures a proper normalization of $A(\vec{x})P_{\mathrm{sig}}$. Using Eqs. (2), (3), and (4), the PD to observe a $t\bar{t}$ event with four-momenta $\vec{x}$ in the detector can be written explicitly as

$$
P_{\mathrm{sig}}(\vec{x}; m_t, k_{\mathrm{JES}}) = \frac{1}{\sigma_{p\bar{p}\to t\bar{t},\mathrm{obs}}(m_t, k_{\mathrm{JES}})}
$$
$$
\times \sum_{\substack{\mathrm{quark} \\ \mathrm{flavors}}} \int_{\vec{q}_1, \vec{q}_2} \mathrm{d}\vec{q}_1 \mathrm{d}\vec{q}_2 f(\vec{q}_1) f(\vec{q}_2)
$$
$$
\times \frac{(2\pi)^4 |\mathcal{M}_{q\bar{q}\to t\bar{t}}|^2}{2g_{\mu\nu}q_1^\mu q_2^\nu} \mathrm{d}\Phi_6
$$
$$
\times W(\vec{x}, \vec{y}; k_{\mathrm{JES}}). \qquad (7)
$$

The parametrization of $|\mathcal{M}_{q\bar{q}\to t\bar{t}}|^2$ and $\sigma_{p\bar{p}\to t\bar{t},\mathrm{obs}}$ are discussed below, and the calculation of P_{sig} is given in Sec. V F.

1. Calculation of $|\mathcal{M}_{q\bar{q}\to t\bar{t}}|^2$

The LO matrix element for the $q\bar{q} \to t\bar{t}$ process [46,47] is given by

$$
|\mathcal{M}_{q\bar{q}\to t\bar{t}}|^2 = \frac{16\pi^2\alpha_s^2}{9} F\bar{F} \cdot (2 - \beta^2\sin^2(\theta_{qt})), \qquad (8)
$$

where α_s is the strong coupling, $\beta = |\vec{p}_t|/E_t$ represents the velocity of the t (or $\bar{t}$) quark in the $q\bar{q}$ rest frame, and θ_{qt} denotes the angle between the incoming parton and the outgoing top quark in the $q\bar{q}$ rest frame. The form factors $F\bar{F}$ are identical to those given in Eqs. (24) and (25) of Ref. [48].

2. Calculation of $\sigma_{p\bar{p}\to t\bar{t},\mathrm{obs}}$

The calculation of the total cross section for $t\bar{t}$ production observed in the detector defined in Eq. (6) is challenging,

because a double integral has to be performed over all possible partonic and measured configurations for each set of (m_t, k_{JES}). We therefore apply a MC integration technique, and factorize the partonic and measured parts of the calculation to obtain:

$$
\sigma_{p\bar{p}\to t\bar{t},\mathrm{obs}}(m_t) = \int_{\vec{y}} \mathrm{d}\vec{y}\mathrm{d}\sigma_{p\bar{p}\to t\bar{t}}(\vec{y}; m_t, k_{\mathrm{JES}})A(\vec{x})W(\vec{x}, \vec{y}; k_{\mathrm{JES}})
$$
$$
\approx \sigma_{p\bar{p}\to t\bar{t},\mathrm{tot}}(m_t) \times \langle A(m_t, k_{\mathrm{JES}})\rangle_{\vec{x}}, \qquad (9)
$$

where

$$
\sigma_{p\bar{p}\to t\bar{t},\mathrm{tot}}(m_t) = \int_{\vec{y}} \mathrm{d}\vec{y}\mathrm{d}\sigma_{p\bar{p}\to t\bar{t}}(\vec{y}; m_t, k_{\mathrm{JES}}) \qquad (10)
$$

is the total partonic cross section for $t\bar{t}$ production in $p\bar{p}$ collisions as shown in Fig. 1, and $\langle A(m_t, k_{\mathrm{JES}})\rangle_{\vec{x}}$ is the mean acceptance averaged over all possible configurations of $\vec{x}$ for a given set of (m_t, k_{JES}) parameters.

3. Calculation of the mean acceptance

The calculation of the mean acceptance $\langle A(m_t, k_{\mathrm{JES}})\rangle_{\vec{x}}$ proceeds in two steps:

(i) First, $\langle A(m_t, k_{\mathrm{JES}} \equiv 1)\rangle_{\vec{x}}$ is determined using MC events processed with the full simulation of the detector, according to

$$
\langle A(m_t, k_{\mathrm{JES}} \equiv 1)\rangle_{\vec{x}} = \frac{\sum_{i=1}^{N_{\mathrm{acc}}} w_{\mathrm{MC}}w_{\mathrm{exp}}}{\sum_{i=1}^{N_{\mathrm{gen}}} w_{\mathrm{MC}}}. \qquad (11)
$$

In this expression, N_{gen} denotes the total number of generated events, and N_{acc} represents the total number of events from within detector acceptance,
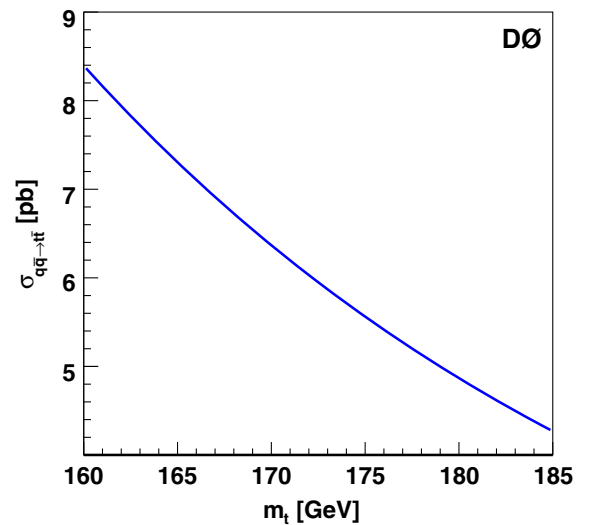

FIG. 1 (color online). The total partonic cross section for $t\bar{t}$ production in $p\bar{p}$ collisions through quark-antiquark annihilation at LO, as defined in Eq. (10).

while w_{MC} is the MC weight from ALPGEN, and $w_{\exp}$ the weight that accounts for experimental factors such as the trigger and identification efficiencies.

(ii) In the second step, the dependence of the mean acceptance on k_{JES} is derived using simulated parton level events, where the detector response is taken into account through the TF $W(\vec{x}, \vec{y}; k_{\mathrm{JES}})$ for the corresponding k_{JES} value.

The mean acceptance is shown for each data-taking epoch in Fig. 2 for $e + \mathrm{jets}$ and in Fig. 3 for $\mu + \mathrm{jets}$ final states.

C. The background probability

The differential partonic cross section for P_{bkg} is calculated according to

$$
\begin{aligned}
P_{\mathrm{bkg}}(\vec{x}; k_{\mathrm{JES}}) = {} & \frac{1}{\sigma_{p\bar{p}\to W+\mathrm{jets,obs}}(k_{\mathrm{JES}})} \\
& \times \sum_{\substack{\text{quark} \\ \text{flavors}}} \int_{q_{1,z}, q_{2,z}} dq_{1,z} dq_{2,z} f(q_{1,z}) f(q_{2,z}) \\
& \times \frac{(2\pi)^4 |\mathcal{M}_{q\bar{q}\to W+\mathrm{jets}}|^2}{2g_{\mu\nu} q_1^\mu q_2^\nu} d\Phi_6 \\
& \times W(\vec{x}, \vec{y}; k_{\mathrm{JES}}),
\end{aligned}
\tag{12}
$$

which is similar to P_{sig} in Eq. (7), with the exception that the initial-state partons are all assumed to have $p_T = 0$. The ME
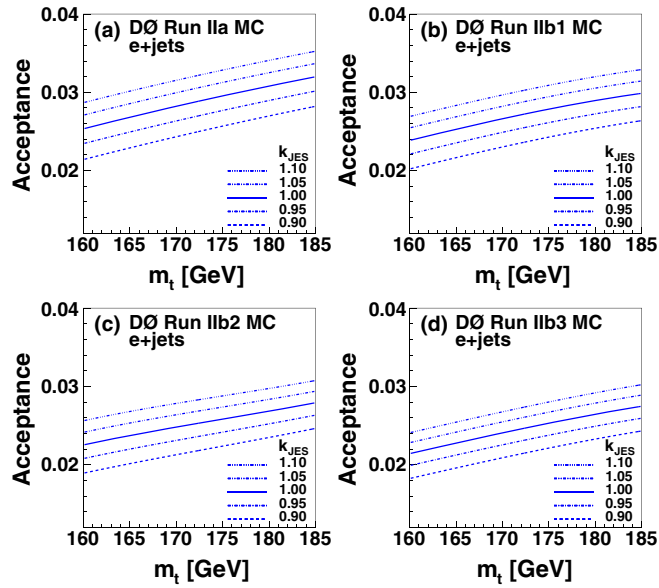

FIG. 2 (color online). Mean acceptance $\langle A(m_t, k_{\mathrm{JES}} \equiv 1) \rangle_{\vec{x}}$ with respect to the total partonic cross section for $p\bar{p} \to t\bar{t}$ production, as a function of m_t for different k_{JES} values in the $e + \mathrm{jets}$ final state, for (a) Run IIa, (b) Run IIb1, (c) Run IIb2, and (d) Run IIb3. The acceptance tends to decrease for later epochs due to a decreased reconstruction efficiency, which is mainly caused by the higher instantaneous luminosity in the second half of Run II and detector aging.
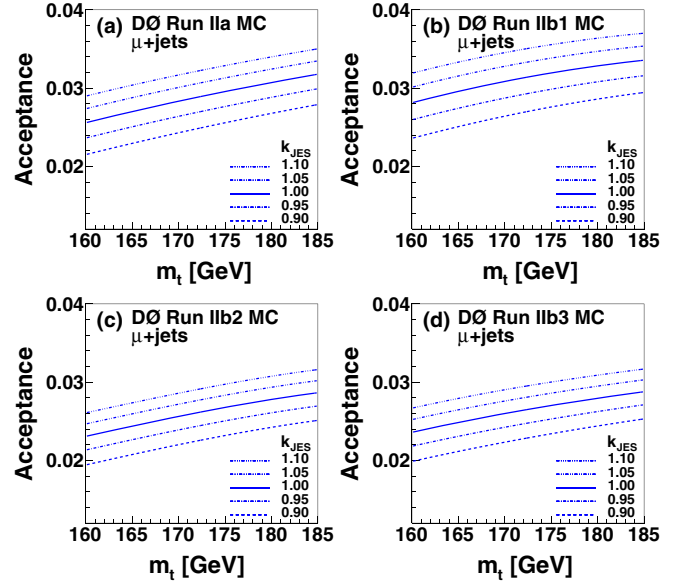
FIG. 3 (color online). Same as Fig. 2, but for the $\mu + \mathrm{jets}$ final state for (a) Run IIa, (b) Run IIb1, (c) Run IIb2, and (d) Run IIb3.

$\mathcal{M}_{q\bar{q}\to W+\mathrm{jets}}$ is calculated at LO using the ME for $W + 4\mathrm{jets}$ production as implemented in the VECBOS [49] program. Since VECBOS treats the final state quarks as massless, the same ME is used to model the production of W bosons in association with $u, d, s, c,$ and b-quark jets. By definition, P_{bkg} is independent of m_t. The dependence of P_{bkg} on k_{JES} is taken into account, as before, through the TF.

D. Modeling of detector response

Here, we describe the modeling of the detector response through the TF $W(\vec{x}, \vec{y}; k_{\mathrm{JES}})$. We use a parameterized TF, as a full simulation of the detector would not be computationally feasible.

In constructing the TF, we assume that the functions for individual final-state particles are not correlated. We therefore factorize the TF into contributions from the four jets and the charged lepton used to calculate P_{sig}. The resolution of the $\not{p}_T$ is worse than that of the p_T of jets and leptons, and is therefore not used in defining event probabilities. We assume that the directions of the e, μ, and jets in (η, ϕ) space are well-measured. The effect of finite detector resolutions in η and ϕ is studied for jets and found to be negligible. The TF for jet and charged lepton directions are therefore represented by δ functions, $\delta^2(\eta, \phi) \equiv \delta(\eta_y - \eta_x)\delta(\phi_y - \phi_x)$, thereby reducing the number of integration variables by $5 \times 2 = 10$. The finite resolutions on the energies of jets and charged leptons are explicitly taken into account, as described in Secs. V D 1, V D 2, and V D 3.

There is an inherent ambiguity in assigning measured jets to partons from $t\bar{t}$ decay. Consequently, all 24 jet-parton assignments that are possible in LO are considered.

The inclusion of b tagging information provides improved identification of the correct jet-parton assignment through weights. The weight w_i for the i-th jet-parton assignment is defined by a product of individual weights w_i^j for each jet j. For b tagged jets, w_i^j is equal to the per-jet tagging efficiency $\varepsilon_{\rm tag}(\alpha_k; E_T^j, \eta^j)$, where α_k labels the configurations where the jet is assigned to either (i) a b quark, (ii) a c quark, or (iii) a u, d, s quark or gluon. For untagged jets, the w_i^j factors are equal to $1 - \varepsilon_{\rm tag}(\alpha_k; E_T^j, \eta^j)$. Hence, the weights w_i are close to unity for those configurations that assign b-tagged jets to b quarks and untagged jets to u, d, s quarks or gluons, and $w_i \ll 1$ otherwise. Since the contributions to $W + {\rm jets}$ processes are parameterized by $\mathcal{M}_{q\bar{q} \to W+{\rm jets}}$ without regard to heavy-flavor content, the weights w_i for each of the 24 permutations in the background probability are all equal. The sum of weights is always normalized to unity: $\sum_{i=1}^{24} w_i = 1$.

We define the TF as

$$
W(\vec{x}, \vec{y}; k_{\rm JES}) = W_\ell(E_x, E_y)\delta_\ell^2(\eta, \phi)
$$
$$
\times \sum_{i=1}^{24} w_i \left\{ \prod_{j=1}^{4} \delta_{ij}^2(\eta, \phi) W_{\rm jet}(E_x^i, E_y^j; k_{\rm JES}) \right\},
$$
(13)

where E is the energy and $W_{\rm jet}$ is the TF appropriate for the energy resolution of jets, as discussed in Sec. V D 1, and W_ℓ is either W_e, the energy resolution for electrons, as discussed in Sec. V D 2, or W_μ, the resolution in the transverse momentum of muons, as discussed in Sec. V D 3.

1. Modeling of jet momentum

The TF for jets represents the probability that the jet energy E_x measured in the detector corresponds to a parent quark of energy E_y. It is parameterized in terms of a double Gaussian function whose means and widths depend on E_y. For $k_{\rm JES} \equiv 1$, it is given by

$$
W_{\rm jet}(E_x, E_y; k_{\rm JES} = 1) = \frac{1}{\sqrt{2\pi}(p_2 + p_3 p_5)}
$$
$$
\times \left\{ \exp\left(-\frac{[(E_x - E_y) - p_1]^2}{2p_2^2} \right) \right.
$$
$$
\left. + p_3 \exp\left(-\frac{[(E_x - E_y) - p_4]^2}{2p_5^2} \right) \right\},
$$
(14)

where the p_i are linear functions of the energy of the parent quark:

$$
p_i = a_i + b_i E_y. \tag{15}
$$

For $k_{\rm JES} \neq 1$, the jet TF changes to

$$
W_{\rm jet}(E_x, E_y; k_{\rm JES}) = \frac{W_{\rm jet}(\frac{E_x}{k_{\rm JES}}, E_y; 1)}{k_{\rm JES}}, \tag{16}
$$

where the $k_{\rm JES}$ factor in the denominator preserves the normalization $\int {\rm d}E_x W_{\rm jet}(E_x, E_y; k_{\rm JES}) = 1$.

The parameters a_i and b_i in Eq. (15) are determined from fully simulated $t\bar{t}$ events for each data-taking epoch, after applying the jet energy corrections and resolution smearing, which are required to match the detector response in data. To avoid potential bias from the kinematic selections, all the requirements described in Sec. IV are applied at detector level, except for having exactly four jets, at least one of which is b-tagged, and except the p_T threshold for the jets, which is lowered to 15 GeV. The parameters a_i and b_i are extracted from MC generated $t\bar{t}$ events with m_t values ranging between 150 and 190 GeV, for each data-taking epoch. We use an unbinned likelihood fit that maximizes the product of the $W_{\rm jet}$ terms for all jets in all events as a function of a_i and b_i. Separate sets of a_i and b_i parameters are derived for three categories of jets: (i) from light quarks (u, d, s) and charm, (ii) from b quarks with a muon of a relatively low p_T within the jet cone (soft muon tag), and (iii) for all other b quarks. This is done for four regions of η: $|\eta| \leq 0.4$, $0.4 < |\eta| \leq 0.8$, $0.8 < |\eta| \leq 1.6$, and $1.6 < |\eta| \leq 2.5$, to take into account the η dependence of the detector response. These same four regions are used to derive the correction for the flavor-dependence of the detector response to jets [15]. When deriving the TF, the matching of jets to partons is performed using a simple cone-matching algorithm, where a jet is considered uniquely matched to a parton if $\Delta R({\rm jet}, {\rm closest\ parton}) < R_{\rm cone}/2 = 0.25$. The cone-matching parameter is chosen to maximize the matching efficiency, while minimizing the mismatching rate of quarks to jets from pile up. The probability of a detector-level jet not to be matched to a particle-level jet is 2% per jet. Figure 4 illustrates the TF for jets from category (i) as a function of E_x for different values of E_y for Run IIb2, which is representative of all four data-taking epochs. The TF for jets from category (ii) is shown in Fig. 5, and for category (iii) in Fig. 6. The values of the a_i and b_i parameters for each of the four data-taking epochs are summarized in Appendix B.

To verify that the TF describes the detector response to jets, we use fully simulated $t\bar{t}$ MC events with all jet energy corrections and smearing needed to match resolutions in data. They must pass all selections summarized in Sec. IV, and each of the four jets needs to be uniquely matched to a quark. In Fig. 7 we compare the distributions in the invariant mass of the dijet system that matches the two quarks from the $W \to q\bar{q}'$ decay, and the invariant mass of those two quarks, smeared with the jet TF. We compare the distributions in the invariant mass of the trijet system
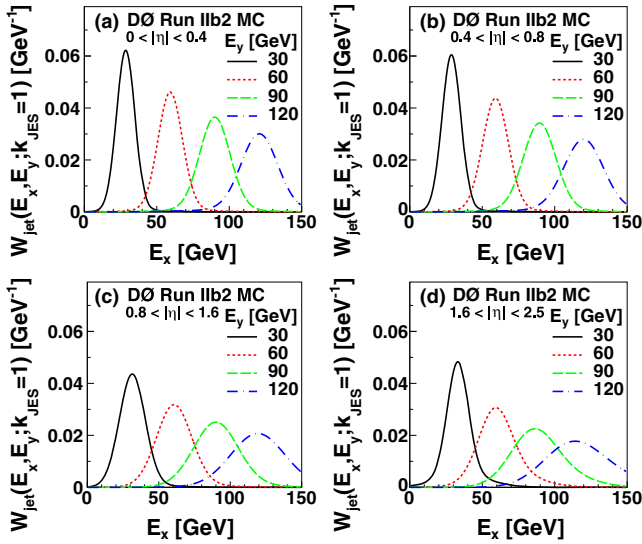
FIG. 4 (color online).   The TF $W_{\text{jet}}(E_x, E_y; k_{\text{JES}})$ for light-quark jets at $k_{\text{JES}} \equiv 1$ in Run IIb2, as a function of the measured jet energy E_x, for different parton energies E_y, as indicated in the legend. The TF are shown in four pseudorapidity regions: (a) $|\eta| \leq 0.4$, (b) $0.4 < |\eta| \leq 0.8$, (c) $0.8 < |\eta| \leq 1.6$, and (d) $1.6 < |\eta| \leq 2.5$. Energies $E_x > 150$ GeV are also considered, but not shown.

matched to one of the top quarks and the corresponding quarks smeared with the jet TF in Fig. 8. Both tests indicate that the jet TF well describe the jet resolutions. Any residual disagreements are taken into account through the calibration procedures, described in Secs. VI A and VII A.
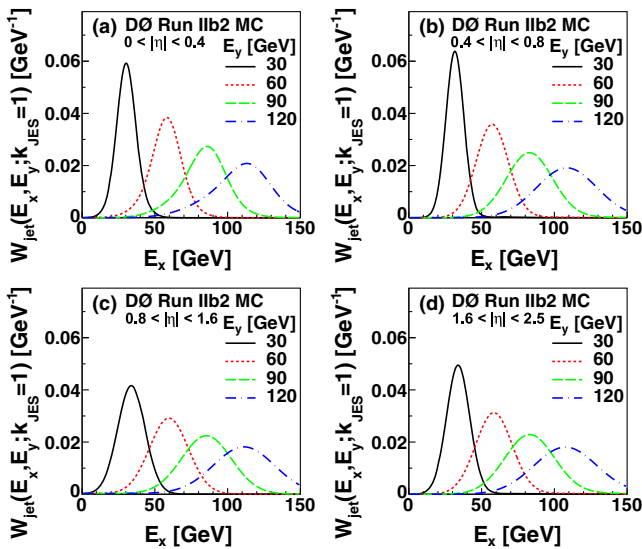
FIG. 5 (color online).   Same as Fig. 4, but for b-quark jets with at least one muon inside the jet cone. The TF are shown in four pseudorapidity regions: (a) $|\eta| \leq 0.4$, (b) $0.4 < |\eta| \leq 0.8$, (c) $0.8 < |\eta| \leq 1.6$, and (d) $1.6 < |\eta| \leq 2.5$.
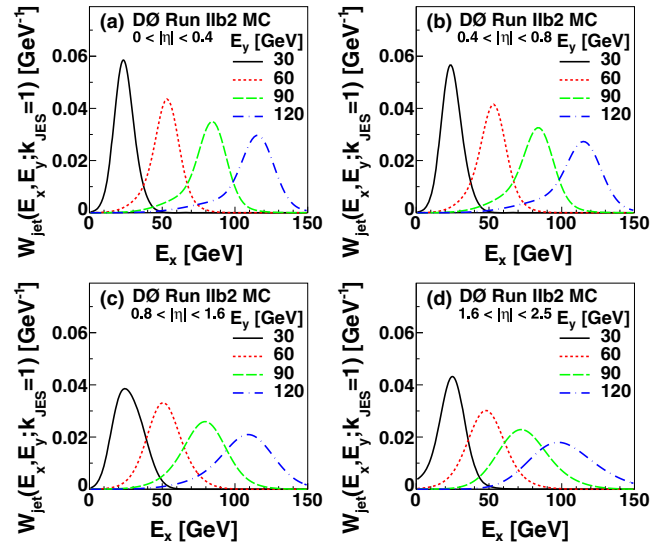
FIG. 6 (color online).   Same as Fig. 4, but for b-quark jets without muons inside the jet cone. The TF are shown in four pseudorapidity regions: (a) $|\eta| \leq 0.4$, (b) $0.4 < |\eta| \leq 0.8$, (c) $0.8 < |\eta| \leq 1.6$, and (d) $1.6 < |\eta| \leq 2.5$.

2. Modeling of electron momentum

The electron energy resolution is parameterized by the TF

$$W_e(E_x, E_y) = \frac{1}{\sqrt{2\pi}\sigma} \exp\left[-\frac{1}{2}\left(\frac{E_x - E_y'}{\sigma}\right)^2\right], \quad (17)$$
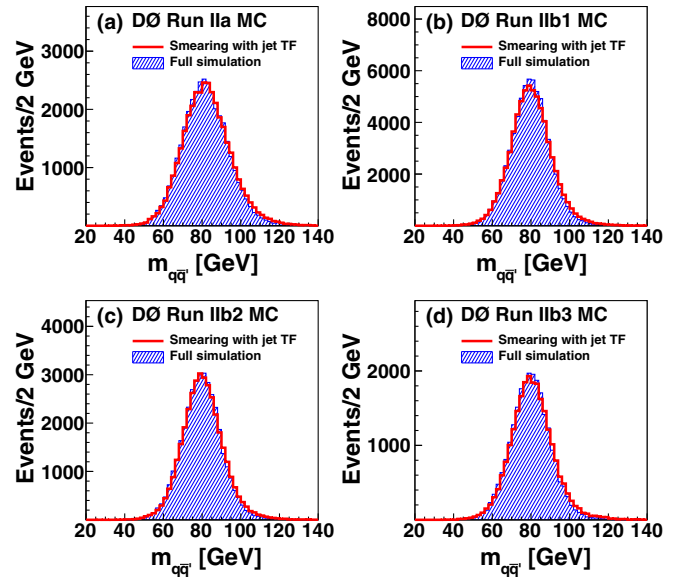
FIG. 7 (color online).   Invariant mass of the dijet system matched to the $W \to q\bar{q}'$ decay for (a) Run IIa, (b) Run IIb1, (c) Run IIb2, and (d) Run IIb3. Fully simulated jet-parton matched MC events passing all selection requirements are compared to partons with energies smeared using the jet TF, and then applying the same standard event selection criteria.
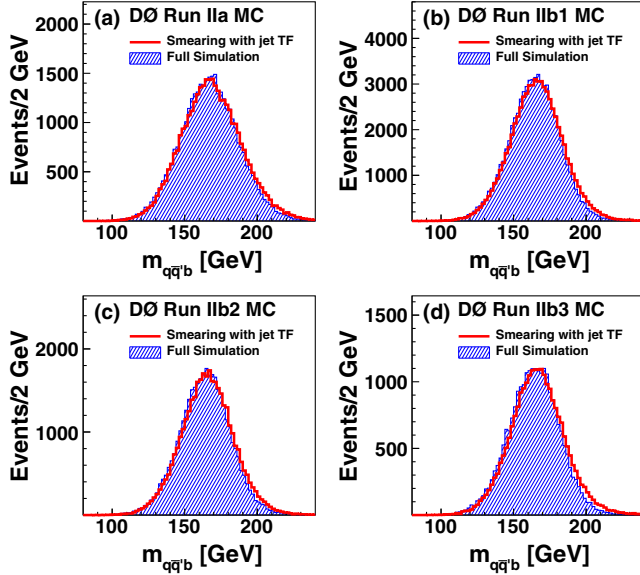
FIG. 8 (color online). Same as Fig. 7, but for the invariant mass of the trijet system matched to the hadronic decay of the top quark for (a) Run IIa, (b) Run IIb1, (c) Run IIb2, and (d) Run IIb3.

with

$$E_y' = E_y + 0.324 \text{ GeV}, \tag{18}$$

$$\sigma = \sqrt{(0.028 \cdot E_y')^2 + (S \cdot E_y')^2 + (0.4 \text{ GeV})^2}, \tag{19}$$

$$S = \frac{0.164 \text{ GeV}^{\frac{1}{2}}}{\sqrt{E_y'}} + \frac{0.122 \text{ GeV}}{E_y'} \exp\left(\frac{C}{\sin\theta_e}\right) - C, \tag{20}$$

$$C = 1.3519 - \frac{2.0956 \text{ GeV}}{E_y'} - \frac{6.9858 \text{ GeV}^2}{E_y'^2}, \tag{21}$$

where E_x is the reconstructed electron energy, E_y is the electron energy at parton level, and θ_e is the polar angle of the electron relative to the proton beam direction. These parameters are obtained from the modeling of electron energy response and resolution in Ref. [50] for Run IIa, and are used for all four data-taking epochs because they changed only marginally between the epochs.

3. Modeling of muon momentum

The resolution of the central tracker, which provides the measurement of the muon p_T, is described through the uncertainty on the curvature $\kappa \equiv 1/p_T$ of the muon track. The muon TF is parameterized as

$$W_\mu(\kappa_x, \kappa_y) = \frac{1}{\sqrt{2\pi}\sigma} \exp\left[-\frac{1}{2}\left(\frac{\kappa_x - \kappa_y}{\sigma}\right)^2\right], \tag{22}$$

where κ_x is the reconstructed muon curvature, and κ_y is the corresponding quantity at parton level.

TABLE III. Parameters of the muon TF for muons with at least three associated hits in the SMT and for all other tracks. These values are the same for all the four data-taking epochs.

Parameter	≥ 3 hits in the SMT	< 3 hits in the SMT
s_0 (GeV^{-1})	2.082×10^{-3}	3.620×10^{-3}
s_1	1.125×10^{-2}	1.388×10^{-2}
c_0 (GeV^{-1})	7.668×10^{-3}	2.070×10^{-2}
c_1	7.851×10^{-2}	7.042×10^{-2}

The resolutions

$$\sigma = \begin{cases} s & \text{for } |\eta| \leq 1.4 \\ \sqrt{s^2 + \{c \cdot (|\eta| - 1.4)\}^2} & \text{for } |\eta| > 1.4 \end{cases} \tag{23}$$

are obtained from muon tracks in simulated events, where the s and c parameters are linear functions of κ_y:

$$s = s_0 + s_1 \kappa_y, \tag{24}$$

$$c = c_0 + c_1 \kappa_y. \tag{25}$$

The values of these coefficients, which are the same for all four data-taking epochs are given in Table III for muon tracks with at least three associated hits in the SMT, and for all other tracks. This simplified parameterization of the momentum resolution is valid at high transverse momenta ($p_T > 20$ GeV) where the limitations in coordinate resolution dominate over the effects of multiple scattering.

E. Extraction of the parameters of interest

In this section, we discuss how the parameters f, m_t, and k_{JES} are extracted from a sample of N selected events that are characterized by their measured quantities $\mathbb{X}_N = \{\vec{x}_1, \vec{x}_2, ..., \vec{x}_N\}$. A likelihood function, $\mathcal{L}(\mathbb{X}_N; m_t, k_{\text{JES}}, f)$, is constructed at each grid point from the product of the individual P_{evt} values according to

$$\mathcal{L}(\mathbb{X}_N; m_t, k_{\text{JES}}, f) \equiv \prod_{i=1}^{N} P_{\text{evt}}(\vec{x}_i; m_t, k_{\text{JES}}, f). \tag{26}$$

To construct this likelihood from P_{evt}, P_{sig} is calculated on a grid in (m_t, k_{JES}) with spacings of (1 GeV, 0.01). For simulated $t\bar{t}$ events, it covers 25 points in m_t ranging between $m_t^{\text{gen}} - 12$ GeV and $m_t^{\text{gen}} + 12$ GeV, and 21 points in k_{JES} between $k_{\text{JES}}^{\text{gen}} - 0.1$ and $k_{\text{JES}}^{\text{gen}} + 0.1$. The ranges are chosen to ensure that they contain the numerically relevant part of the likelihood for all pseudo-experiments (cf. Secs. VI A and VII A). For data, the grid is extended to [153 GeV, 192 GeV] in m_t and to [0.85, 1.15] in k_{JES}. This choice is made because the values of m_t and k_{JES} in data are not known *a priori*, as the analysis is performed blinded, following the procedure to be described

in Sec. VII B. For simulated background events, the same grid is chosen as for data. Since P_{bkg} does not depend on m_t, it is calculated on a grid in k_{JES} only, with the same spacing and ranges as P_{sig}.

1. Extraction of the signal fraction

The likelihood is determined by the value of the signal fraction $\hat{f}(m_t, k_{\text{JES}})$ that maximizes $\mathcal{L}$ for every assumed pair of (m_t, k_{JES}) values from the grid on which $\mathcal{L}$ is calculated. As will be detailed in Secs. VI and VII, the measurement of the signal fraction is performed prior to the measurement of m_t and k_{JES}. To extract f^{fit} independently, the parameters m_t and k_{JES} are integrated over a uniform prior

$$f^{\text{fit}} = \frac{\int dm_t dk_{\text{JES}} \hat{f} \mathcal{L}(\mathbb{X}_N; m_t, k_{\text{JES}}, \hat{f})}{\int dm_t dk_{\text{JES}} \mathcal{L}(\mathbb{X}_N; m_t, k_{\text{JES}}, \hat{f})}, \qquad (27)$$

by summing over all points (m_t, k_{JES}) on the grid that reflect the numerically relevant part of the likelihood, cf. Sec. V E.

2. Extraction of the top-quark mass and k_{JES}

To obtain the best unbiased estimate of m_t^{fit}, the two-dimensional likelihood $\mathcal{L}(\mathbb{X}_N; m_t, k_{\text{JES}}) = \mathcal{L}(\mathbb{X}_N; m_t, k_{\text{JES}}, \hat{f}(m_t, k_{\text{JES}}))$ is projected onto the m_t axis

$$\mathcal{L}(\mathbb{X}_N; m_t) = \int dk_{\text{JES}} \mathcal{L}(\mathbb{X}_N; m_t, k_{\text{JES}}) \qquad (28)$$

using Simpson's rule [51]. The best unbiased estimate for m_t^{fit} is then given by

$$m_t^{\text{fit}} = \frac{\int dm_t m_t \mathcal{L}(\mathbb{X}_N; m_t)}{\int dm_t \mathcal{L}(\mathbb{X}_N; m_t)}, \qquad (29)$$

and its uncertainty by

$$\sigma_{m_t}^{\text{fit}} = \left\{ \frac{\int dm_t (m_t - m_t^{\text{fit}})^2 \mathcal{L}(\mathbb{X}_N; m_t)}{\int dm_t \mathcal{L}(\mathbb{X}_N; m_t)} \right\}^{\frac{1}{2}}. \qquad (30)$$

Thus, by construction, the statistical uncertainty on m_t includes the impact of the statistical uncertainty on k_{JES}. To obtain the best unbiased estimates for $k_{\text{JES}}^{\text{fit}}$ and $\sigma_{k_{\text{JES}}}^{\text{fit}}$, the same procedure is applied as to estimate m_t^{fit} and $\sigma_{m_t}^{\text{fit}}$, by replacing $k_{\text{JES}} \leftrightarrow m_t$ in Eqs. (28)–(30).

F. Calculation of the signal probability

In the calculation of P_{sig} in Eq. (7), a total of 24 variables are associated with the integration over the momenta of the two colliding quarks $d\vec{q}_1 d\vec{q}_2$ and over the phase space of the six-body final state, $d\Phi_6$. After taking into account the $\delta^2(\eta, \phi)$ functions for the directions of the four jets and the

charged lepton according to the TF of Eq. (13), the dimensionality of the integral is reduced by $2 \times 5 = 10$. Imposing energy-momentum conservation provides four additional constraints, resulting in a ten-dimensional integral that must be evaluated. The transverse momentum of the neutrinos is inferred from momentum conservation, resulting in up to eight solutions for the neutrino kinematics, which are averaged. The measurement of $\not{p}_T$ is not used because of its limited experimental resolution.

The integration in Eq. (7) is performed numerically using MC integration [52]. To reduce the computational demands of the integration, importance sampling [53] is used. To fully exploit importance sampling, we perform a Jacobian transformation of the nominal ten integration variables to optimized variables where prior information is either known or can be obtained easily. This prior information is then used in the importance sampling. Thus, the integration is performed over the masses of the top and antitop quarks, which are assumed to be equal, the masses of the W^+ and W^- bosons, the energy (curvature) of the electron (muon), $E_q/(E_q + E_{\bar{q}'})$ for the quarks from the $W \to q\bar{q}'$ decay in the LO approximation, and the transverse momenta $q_{1,\text{x}}, q_{1,\text{y}}, q_{2,\text{x}}, q_{2,\text{y}}$ of the colliding quarks. The constraint $M_W = 80.4$ GeV for the *in-situ* JES calibration is imposed by integrating over M_W according to a prior given by a Breit-Wigner distribution. More details about the motivation for the choice of integration variables can be found in Ref. [54].

The computation of P_{sig} in the previous version of this analysis [14], which is based on about $1/4$ of the full Run II integrated luminosity, and uses only one set of MC simulations, required two million CPU-hours [55]. To make our ME technique applicable to the full Run II data sample of 9.7 fb^{-1}, and to perform a calibration of the method with dedicated MC simulations for each of the four data-taking epochs, we implement two new approaches to reduce computational demand. These approaches are described in detail in Ref. [54], and are briefly summarized below.

(i) We utilize low-discrepancy sequences for the numerical MC integration of P_{sig} according to Eq. (7), instead of conventional pseudo-random numbers in order to benefit from the key property of low-discrepancy sequences of sampling the integration phase space in a maximally uniform way. This leads to a convergence rate of the estimated integral inversely proportional to N_{sample} [56], which is superior to $\sqrt{N_{\text{sample}}}$ expected for pseudo-random numbers [53], where N_{sample} is the number of samplings of the integrand. We utilize the implementation of Bratley and Fox [57] of the Sobol sequence [58], which is among the best performing low-discrepancy sequences.

An accurate, and computationally efficient estimate of the numerical precision of the integral is a key ingredient of numerical MC integration. Since

the standard error estimator based on the variance of the integrand is too pessimistic for low-discrepancy sequences, because of their superior convergence rate, we implement a dedicated estimator of the numerical uncertainty according to Ref. [59], which represents a novel treatment in the context of the ME technique.

The utilization of low-discrepancy sequences is of particular interest, as it is a procedure universally applicable to MC integration and independent of the computing hardware. Their implementation in our ME technique provides a reduction of about one order of magnitude in computation time, compared to pseudo-random numbers, for the same numerical accuracy.

(ii) We factorize the k_{JES} parameter from the ME computation, a novelty in the context the measurements of m_t with the ME technique. As described in Sec. V E, P_{sig} has to be calculated for $25 \times 21 = 525$ grid points in (m_t, k_{JES}) for simulated $t\bar{t}$ events. Instead of recalculating P_{sig} for each point in (m_t, k_{JES}), we calculate the integral

$$\sum_{\substack{\mathrm{quark} \\ \mathrm{flavors}}} \int_{\vec{q}_1, \vec{q}_2} \mathrm{d}\vec{q}_1 \mathrm{d}\vec{q}_2 f(\vec{q}_1) f(\vec{q}_2) \frac{(2\pi)^4 |\mathcal{M}_{q\bar{q}\to t\bar{t}}|^2}{2g_{\mu\nu} q_1^\mu q_2^\nu} \mathrm{d}\Phi_6$$

(31)

in Eq. (7) only once for a given m_t, and use the result to calculate P_{sig} for all $k_{\mathrm{JES}, i=1,2,\dots,21}$ through multiplication by $W(\vec{x}, \vec{y}; k_{\mathrm{JES}, i})$. This yields another order of magnitude reduction in computation time.

In total, we obtain a reduction of computation time from about 2 h per event, averaged over the sample of simulated $t\bar{t}$ events for $m_t = 172.5$ GeV, to about 80 s per event, i.e., by about two orders of magnitude. Both improvements are verified [54] to provide a performance of the ME technique consistent with that in Ref. [14]. They prove essential for a dramatic improvement in the precision of this analysis by allowing to increase the number of simulated MC events used for the calibration of the ME technique (cf. Secs. VI A and VII A), and for the evaluation of systematic uncertainties (cf. Sec. VIII).

VI. MEASUREMENT OF THE SIGNAL FRACTION

The ME technique calculates P_{evt} from first principles with a LO ME and a parameterized description of the detector response through $W(\vec{x}, \vec{y}; k_{\mathrm{JES}})$. The calculation of the parameters of interest, in this case f, has to be therefore calibrated through simulations. The calibration of the response of the ME technique in f and the subsequent extraction of f from data are the subject of this section.

A. Calibration of the method

Fully simulated $t\bar{t}$ events, as described in Sec. III, at $m_t^{\mathrm{gen}} = 172.5$ GeV and $k_{\mathrm{JES}}^{\mathrm{gen}} = 1$, expected from the standard JES calibration procedure [15], are used for calibrating the response of the ME technique in f. Similarly, fully simulated $W + \mathrm{jets}$ events at $k_{\mathrm{JES}}^{\mathrm{gen}} = 1$ are included to model the dominant background contribution from $W + \mathrm{jets}$ production. We refine the calibration procedure relative to that of Ref. [14] by explicitly accounting for the next-to-dominant contribution from MJ production by using a sample of events in data obtained as described in Sec. III. Since the detector response, and therefore its parametrization, changes between data-taking epochs and final states, this calibration is obtained for each epoch and final state.

At each of the five generated f^{gen} points, ranging between 0.5 and 0.9 in steps of 0.1, 1000 pseudo-experiments (PEs) are constructed, each with the same number of events as observed in data. Since the matrix method provides a normalization of the background contribution from MJ production, each PE contains the same number of randomly drawn MJ events as determined through the matrix method, as shown in Table II. The remaining number of background events is then drawn from the sample of simulated $W + \mathrm{jets}$ events, according to a binomial distribution in $1 - f^{\mathrm{gen}}$.

The PE ensembles at each of the five f^{gen} points are used to obtain a linear calibration for the response of the ME technique in f. This is achieved by parametrizing the signal fraction f^{fit}, extracted as for data in Sec. V E and averaged over the PEs for each given f^{gen} point, versus f^{gen}. The resulting linear parameterizations of the response of the ME technique in f are shown for each data-taking epoch in Fig. 9 for the $e + \mathrm{jets}$, and in Fig. 10 for the $\mu + \mathrm{jets}$ final states. Typical slope parameters are close to 0.75, while typical offsets are few percent at $f^{\mathrm{gen}} \approx 0.70$, as expected from Sec. IV.

B. Results

The extracted f^{fit} in data is calibrated using the results from the previous section for each final state and epoch according to

$$f = \frac{f^{\mathrm{fit}} - o_f}{s_f},$$

(32)

where o_f and s_f are the offset and slope parameters, respectively, as given in Figs. 9 and 10. The uncertainties on o_f and s_f are propagated to f assuming they are Gaussian distributed. The resulting f are given in Table IV, split by final state and by epoch. Averaging f over the entire Run II, weighting the contributions from data-taking epochs by their respective integrated luminosities, yields $f = 63\%$ in the $e + \mathrm{jets}$ and $f = 70\%$ in the
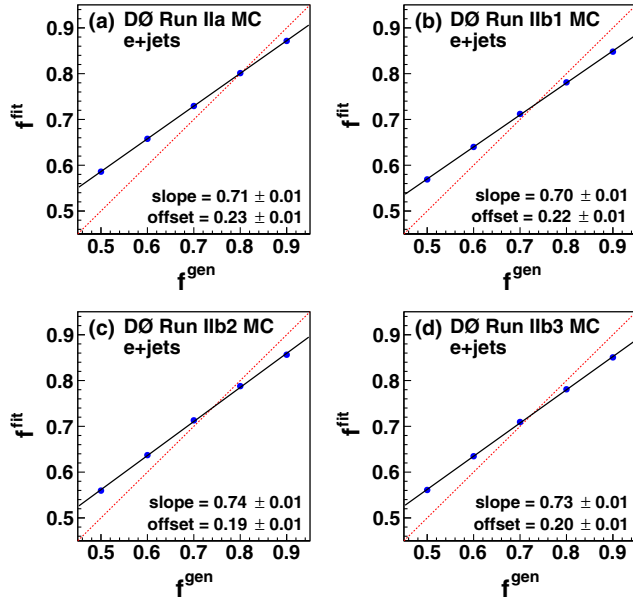
FIG. 9 (color online).   The response of the ME technique in f, derived from the average of f^{fit} over 1000 PEs at each f^{gen} point, for (a) Run IIa, (b) Run IIb1, (c) Run IIb2, and (d) Run IIb3 in the $e + \mathrm{jets}$ final state. The response is fitted with a linear function shown as a solid black line, whose slope and offset values are given at the bottom of the plots. The broken red line represents an ideal response.

$\mu + \mathrm{jets}$ final states, with an absolute uncertainty of 1% from the finite size of the data sample and the calibration.

As a cross-check we translate the measured f values into cross sections for $t\bar{t}$ production, which are also reported in Table IV. Combining them in a similar fashion to f, we find $\sigma_{t\bar{t}} = 7.8 \pm 0.1\,(\mathrm{stat})$ pb in the $e + \mathrm{jets}$ and
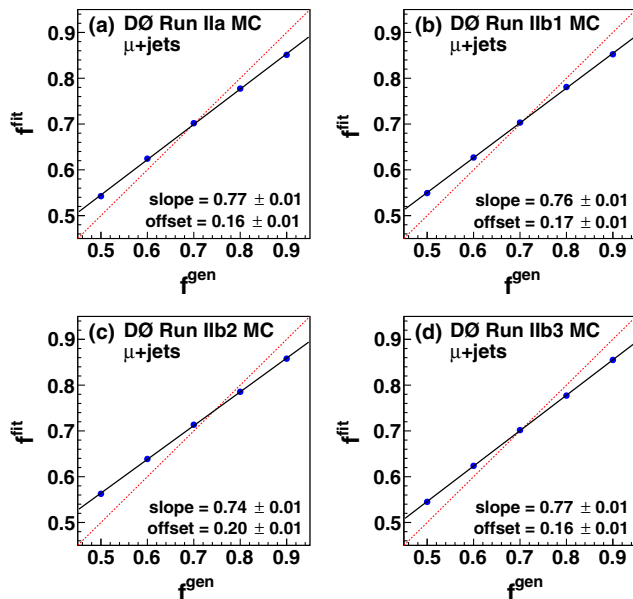

FIG. 10 (color online).   Same as Fig. 9, but in the $\mu + \mathrm{jets}$ final state, for (a) Run IIa, (b) Run IIb1, (c) Run IIb2, and (d) Run IIb3.

TABLE IV.   Signal fractions f measured in data after calibration, split by final state, and for each data-taking epoch as well as combined over the entire Run II. Also shown are the resulting measured cross sections for $t\bar{t}$ production. The combined uncertainty from limited statistical accuracy in data and from the finite number of simulated events used for calibration amounts to 1% for f.

Epoch	Final state	Signal fraction	$\sigma_{t\bar{t}}$ (pb)
Run IIa	$e + \mathrm{jets}$	0.72	8.9
	$\mu + \mathrm{jets}$	0.65	7.8
Run IIb1	$e + \mathrm{jets}$	0.77	7.6
	$\mu + \mathrm{jets}$	0.66	6.8
Run IIb2	$e + \mathrm{jets}$	0.68	7.8
	$\mu + \mathrm{jets}$	0.66	7.5
Run IIb3	$e + \mathrm{jets}$	0.56	7.6
	$\mu + \mathrm{jets}$	0.75	8.0
Run II	$e + \mathrm{jets}$	0.63	7.8
	$\mu + \mathrm{jets}$	0.70	7.6

$\sigma_{t\bar{t}} = 7.6 \pm 0.1\,(\mathrm{stat})$ pb in the $\mu + \mathrm{jets}$ final states. The cross sections determined with the ME technique are in good agreement with the prediction of $\sigma_{t\bar{t}} = 7.24^{+0.23}_{-0.27}$ pb (scale+PDF) from a NNLO calculation at $m_t = 172.5\,\mathrm{GeV}$, including NNLL corrections [40], and using the MSTW2008NNLO set of PDFs [60]. This is also in agreement with $\sigma_{t\bar{t}} = 7.78^{+0.77}_{-0.64}$ pb measured by the D0 Collaboration in 5.3 fb^{-1} of integrated luminosity [61].

VII. MEASUREMENT OF THE TOP-QUARK MASS

As described in Sec. VI, the response of the ME technique in m_t and k_{JES} has to be calibrated prior to the measurement of those parameters. In this section, we describe the calibration procedure, report the measured m_t and k_{JES} values, demonstrate that simulations with our measured values of f, m_t, and k_{JES} describe the data well, and draw comparisons to other measurements of m_t.

A. Calibration of the method

The calibration of the response of the ME technique in m_t and k_{JES} proceeds similarly to the calibration in f described in Sec. VI. It uses seven simulated samples of $t\bar{t}$ events, five at $m_t^{\mathrm{gen}} = 165, 170, 172.5, 175, 180$ GeV for $k_{\mathrm{JES}}^{\mathrm{gen}} = 1$, and two at $k_{\mathrm{JES}}^{\mathrm{gen}} = 0.95, 1.05$ for $m_t^{\mathrm{gen}} = 172.5$ GeV. These are complemented by three simulated samples of $W + \mathrm{jets}$ events at $k_{\mathrm{JES}}^{\mathrm{gen}} = 0.95, 1$, and 1.05. The calibration procedure is refined relative to Ref. [14] by accounting explicitly for the next-to-dominant contribution from MJ production. Together, the $t\bar{t}$, $W + \mathrm{jets}$, and MJ samples are used to obtain a linear calibration for the response of the ME technique in m_t and k_{JES}. The calibration is applied separately for each data-taking epoch and final state to account for varying detector response and sample composition.

At each of the generated $(m_t^{\mathrm{gen}}, k_{\mathrm{JES}}^{\mathrm{gen}})$ points, 1000 PEs are constructed, each containing the same number of events as observed in data, by randomly drawing simulated signal and background events according to the measured f for each data-taking epoch and final state, cf. Table IV. For each PE, the fraction of signal events is changed randomly according to a binomial distribution around the f value measured in data. Since the background contribution from MJ production is modeled using data, it is not changed for different generated $(m_t^{\mathrm{gen}}, k_{\mathrm{JES}}^{\mathrm{gen}})$ points.

The response of the ME technique in m_t and k_{JES} is obtained by extracting m_t^{fit} and $k_{\mathrm{JES}}^{\mathrm{fit}}$ for each pseudo-experiment as in data, i.e., according to the procedure described in Sec. V E. The averages $\langle m_t^{\mathrm{fit}} \rangle$ and $\langle k_{\mathrm{JES}}^{\mathrm{fit}} \rangle$ are determined from Gaussian fits to distributions in m_t^{fit} and $k_{\mathrm{JES}}^{\mathrm{fit}}$, respectively. A linear parametrization of the response in m_t is obtained by fitting $\langle m_t^{\mathrm{fit}} \rangle$ as a function of m_t^{gen}. Those parameterizations are shown for each epoch in Fig. 11 for the $e + \mathrm{jets}$ and in Fig. 12 for the $\mu + \mathrm{jets}$ final states, together with the offset and slope of the linear fits. The response in m_t is close to the ideal case of no offset and unit slope. At $m_t^{\mathrm{gen}} = 172.5$ GeV, which is close to the current world average of $m_t = 173.34$ GeV [9], the difference between the obtained and ideal response in m_t is ≈ 0.5 GeV, i.e., at the level of $\approx 0.25\%$–a very good performance given that a LO ME with parameterized detector response is used in the ME calculation. We verify that the ideal response of the ME technique is retained
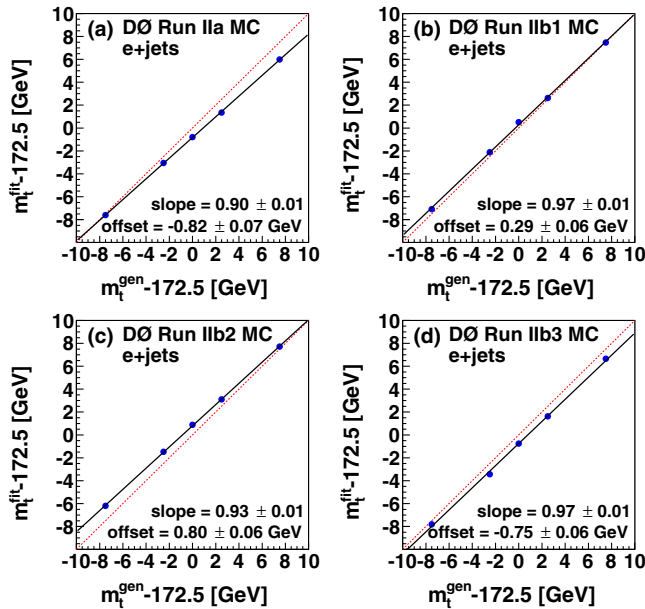

FIG. 12 (color online).   Same as Fig. 11, but in the $\mu + \mathrm{jets}$ final state, for (a) Run IIa, (b) Run IIb1, (c) Run IIb2, and (d) Run IIb3.

through ensemble studies using parton-level $t\bar{t}$ events generated with PYTHIA using a LO ME. In a similar fashion, we obtain a linear parametrization of the response of the ME technique in k_{JES}, as shown in Fig. 13 for the $e + \mathrm{jets}$ and in Fig. 14 for the $\mu + \mathrm{jets}$ final states. As for the case of m_t, the response is close to ideal. At $k_{\mathrm{JES}}^{\mathrm{gen}} = 1$ closest to the expectation from the standard JES correction [15], the difference between the obtained and ideal response is at the level of 1%.

To check the validity of the σ_{m_t} and $\sigma_{k_{\mathrm{JES}}}$ uncertainties extracted from the ME estimates described in Sec. V E, we calculate the pulls in m_t (π_{m_t}) and in k_{JES} ($\pi_{k_{\mathrm{JES}}}$), according to

$$\pi_{m_t} = \frac{m_t^{\mathrm{fit}} - \langle m_t^{\mathrm{fit}} \rangle}{\sigma_{m_t}^{\mathrm{fit}}}, \qquad (33)$$

$$\pi_{k_{\mathrm{JES}}} = \frac{k_{\mathrm{JES}}^{\mathrm{fit}} - \langle k_{\mathrm{JES}}^{\mathrm{fit}} \rangle}{\sigma_{k_{\mathrm{JES}}}^{\mathrm{fit}}}. \qquad (34)$$

For an ideal response, the pull should follow a Gaussian distribution of unit width centered at zero. In our case, both π_{m_t} and $\pi_{k_{\mathrm{JES}}}$ are Gaussian distributed, and centered within uncertainties at zero. For each of the simulated (m_t, k_{JES}) points, we determine the pull widths from the σ parameters of Gaussian fits to π_{m_t} and $\pi_{k_{\mathrm{JES}}}$. The average width of π_{m_t} is then obtained from a constant fit of the distribution of pull width versus m_t^{gen}, as shown for each epoch in Fig. 15 for $e + \mathrm{jets}$ and in Fig. 16 for $\mu + \mathrm{jets}$ final states. The average width of $\pi_{k_{\mathrm{JES}}}$ is obtained in the same way and is given for each epoch in Fig. 17 for $e + \mathrm{jets}$ and in Fig. 18 for $\mu + \mathrm{jets}$ final states. Typically, pull widths are $\approx 20\%$ higher than unity, indicating that the uncertainties $\sigma_{m_t}^{\mathrm{fit}}$ and $\sigma_{k_{\mathrm{JES}}}^{\mathrm{fit}}$ estimated with the ME

FIG. 11 (color online).   The response of the ME technique in m_t, obtained using simulations from the average of m_t^{fit} in 1000 PEs at each m_t^{gen} point, as a function of m_t^{gen}, for (a) Run IIa, (b) Run IIb1, (c) Run IIb2, and (d) Run IIb3 in the $e + \mathrm{jets}$ final state. The response is fitted with a linear function shown as a solid black line, whose slope and offset values are summarized at the bottom of the plots. The red broken line represents an ideal response.
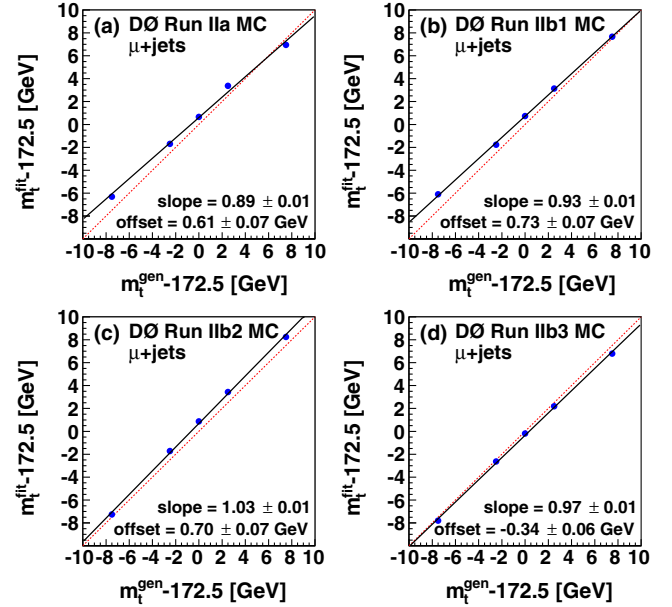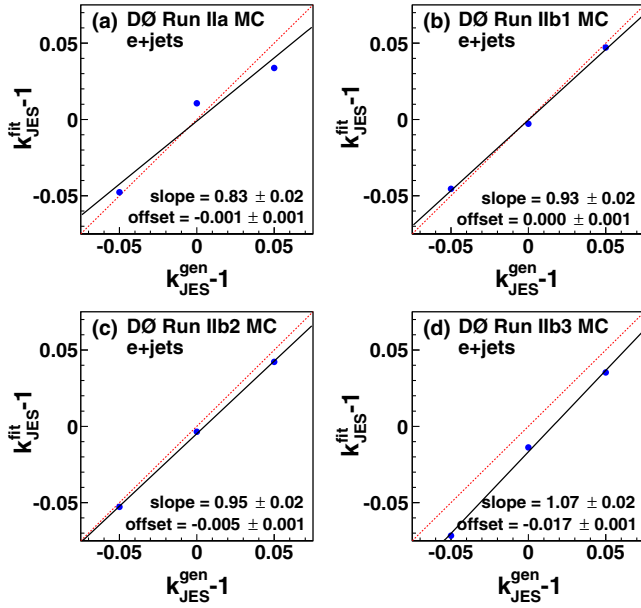
FIG. 13 (color online). The response of the ME technique in k_{JES}, obtained using simulations from the average of k_{JES}^{fit} in 1000 PEs at each k_{JES}^{gen} point, as a function of k_{JES}^{gen}, for (a) Run IIa, (b) Run IIb1, (c) Run IIb2, and (d) Run IIb3 in the $e+$ jets final state. The response is fitted with a linear function shown as a solid black line, whose slope and offset values are summarized at the bottom of the plots. The red broken line represents an ideal response. The poor compatibility of data with the linear fit displayed in panel (a) likely to occur if many fits, in our case, 16, are performed.
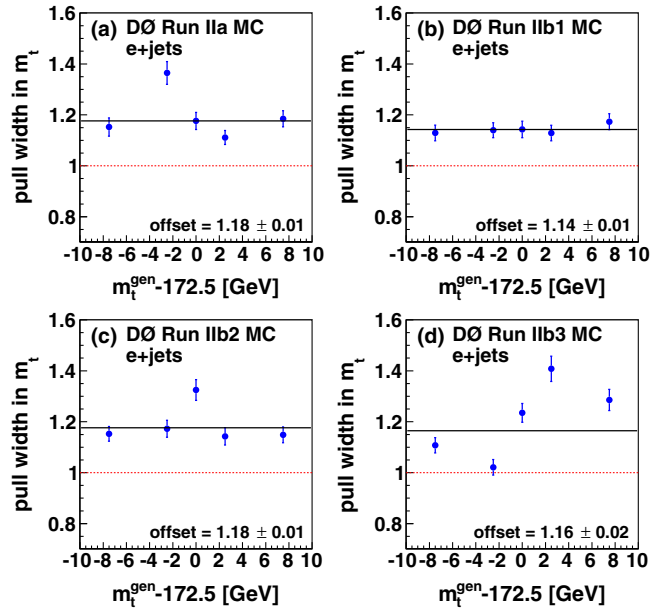
FIG. 15 (color online). The width of the distribution of the pull in m_t, obtained using simulations at each m_t^{gen} point, as a function of m_t^{gen}, for (a) Run IIa, (b) Run IIb1, (c) Run IIb2, and (d) Run IIb3 in the $e+$ jets final state. The error bars are given by the uncertainty on the width of the distribution in π_{m_t}, which is not corrected for the effect that the same event can appear in many PEs, and therefore somewhat underestimated. The pull is fitted with a constant shown as a solid black line, whose value is given at the bottom of the plots. The red broken line represents an ideal pull width of unity.

FIG. 14 (color online). Same as Fig. 13, but in the $\mu+$jets final state, for (a) Run IIa, (b) Run IIb1, (c) Run IIb2, and (d) Run IIb3.

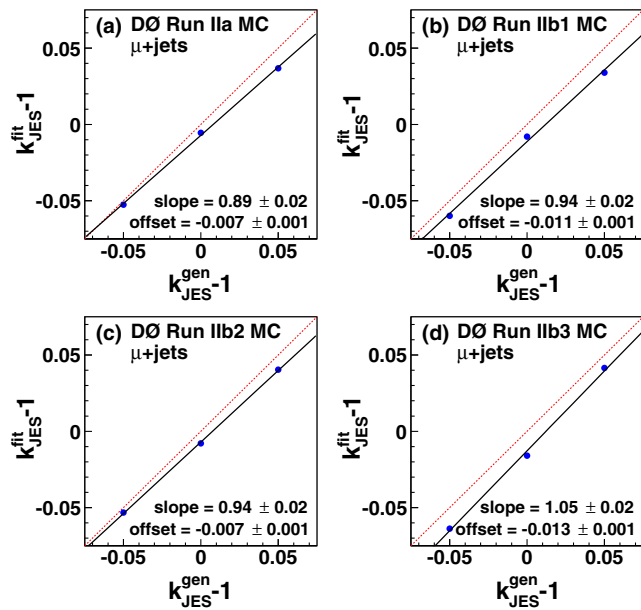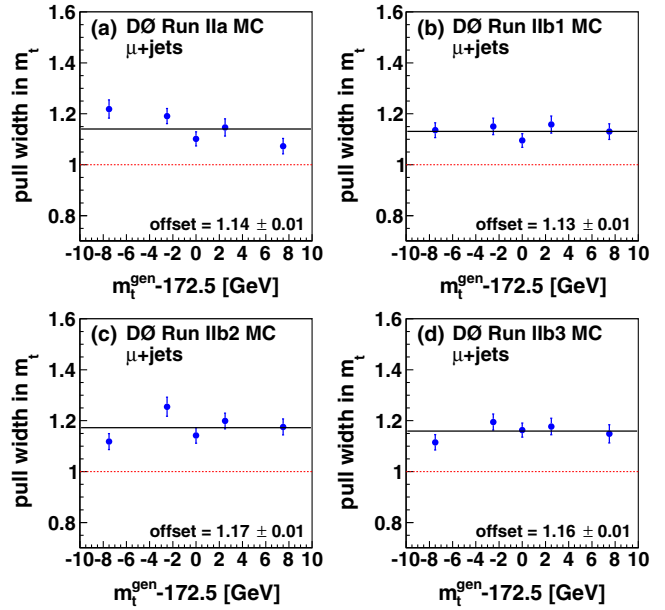FIG. 16 (color online). Same as Fig. 15, but in the $\mu+$ jets final state, for (a) Run IIa, (b) Run IIb1, (c) Run IIb2, and (d) Run IIb3.
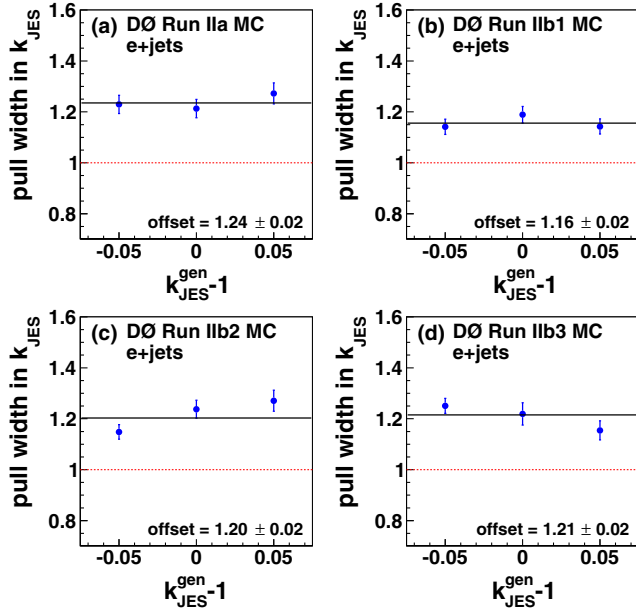
FIG. 17 (color online). The width of the distribution of the pull in k_{JES}, derived using simulations at each $k_{\mathrm{JES}}^{\mathrm{gen}}$ point, as a function of $k_{\mathrm{JES}}^{\mathrm{gen}}$, for (a) Run IIa, (b) Run IIb1, (c) Run IIb2, and (d) Run IIb3 in the $e+$ jets final state. The error bars are given by the uncertainty on the width of the distribution in $\pi_{k_{\mathrm{JES}}}$, which is not corrected for the effect that the same event can appear in many PEs, and therefore somewhat underestimated. The pull is fitted with a constant shown as a solid black line, whose value is given at the bottom of the plots. The broken line represents the case of ideal pull width of unity.
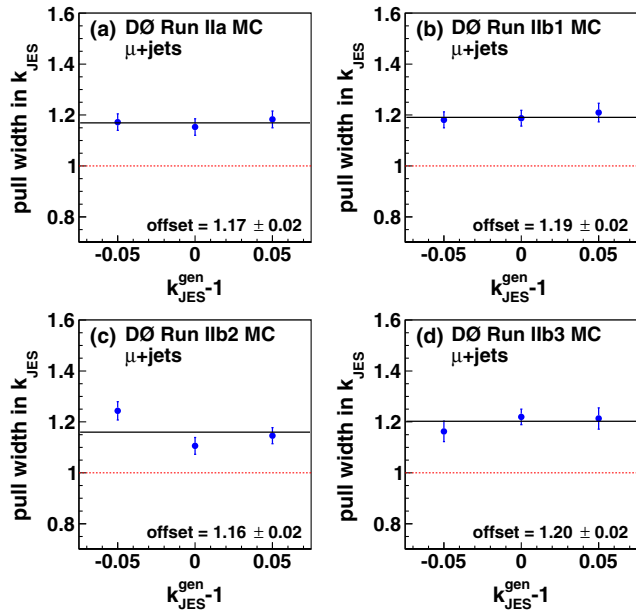

FIG. 18 (color online). Same as Fig. 15, but in the $\mu+$ jets final state, as derived for (a) Run IIa, (b) Run IIb1, (c) Run IIb2, and (d) Run IIb3.

technique are somewhat underestimated. They are therefore corrected by inflating by the value of the pull width found for the respective epoch and final state.

B. Results

Here, we present the results of our application of the ME technique to the full Run II data sample corresponding to 9.7 fb^{-1} of integrated luminosity. The analysis is performed blinded in m_t by adding a constant unknown offset to the extracted m_t value. The offset is drawn according to a uniform distribution in the range $[-2\,\mathrm{GeV}, 2\,\mathrm{GeV}]$. This interval roughly corresponds to $[-3\sigma_{\mathrm{WA}}, 3\sigma_{\mathrm{WA}}]$, where $\sigma_{\mathrm{WA}} = 0.76$ GeV denotes the total uncertainty on the current world average in m_t.

The method to extract m_t and k_{JES} is described in Sec. V E. The linear calibrations from Sec. VII A are applied to data through the likelihoods $\mathcal{L}(\mathbb{X}_N; m_t)$, defined in Eq. (28), and $\mathcal{L}(\mathbb{X}_N; k_{\mathrm{JES}})$ by transforming the m_t and k_{JES} parameters according to

$$m_t \to m_t' = \frac{(m_t - 172.5\,\mathrm{GeV}) - o_{m_t}}{s_{m_t}} + 172.5\,\mathrm{GeV}, \quad (35)$$

$$k_{\mathrm{JES}} \to k_{\mathrm{JES}}' = \frac{(k_{\mathrm{JES}} - 1) - o_{k_{\mathrm{JES}}}}{s_{k_{\mathrm{JES}}}} + 1, \quad (36)$$

where the offset and slope parameters are given in Figs. 11–14. The direct calibration of the likelihoods $\mathcal{L}(\mathbb{X}_N; m_t)$ and $\mathcal{L}(\mathbb{X}_N; k_{\mathrm{JES}})$ takes into account the effect of slopes $\neq 1$ when estimating the statistical uncertainties σ_{m_t} and $\sigma_{k_{\mathrm{JES}}}$ Subsequently, the slope-corrected uncertainties σ_{m_t} are calibrated by multiplying them with the average widths of the distributions in π_{m_t}, summarized in Fig. 15 for $e+$ jets and in Fig. 16 for $\mu+$ jets final states. Similarly, the uncertainties $\sigma_{k_{\mathrm{JES}}}$ are calibrated with the average widths in $\pi_{k_{\mathrm{JES}}}$, given in Figs. 17 and 18.

The m_t measurements are summarized in Fig. 19, along with their statistical uncertainties, which include the statistical contribution from k_{JES}. The observed statistical uncertainty is compared with expectations from pseudo-experiments for $m_t^{\mathrm{gen}} = 172.5$ GeV in Fig. 20 for $e+$ jets and in Fig. 21 for $\mu+$ jets final states. The observed uncertainties are consistent with expectations from simulation. We obtain the combined m_t for the full Run II data set of 9.7 fb^{-1} by calculating the uncertainty-weighted mean, which is the best linear unbiased estimator in case of Gaussian uncertainties, according to

$$\langle m_t \rangle \equiv \frac{\sum_{i=1}^{8} \frac{m_{t,i}}{\sigma_{m_t,i}^2}}{\sum_{i=1}^{8} \frac{1}{\sigma_{m_t,i}^2}}, \qquad \langle \sigma \rangle \equiv \left(\sum_{i=1}^{8} \frac{1}{\sigma_{m_t,i}^2} \right)^{-\frac{1}{2}}, \quad (37)$$

where i runs over all final states and epochs. The combined result after unblinding is $m_t = 174.98 \pm 0.58(\mathrm{stat+JES})$ GeV. To verify that the values measured in each epoch
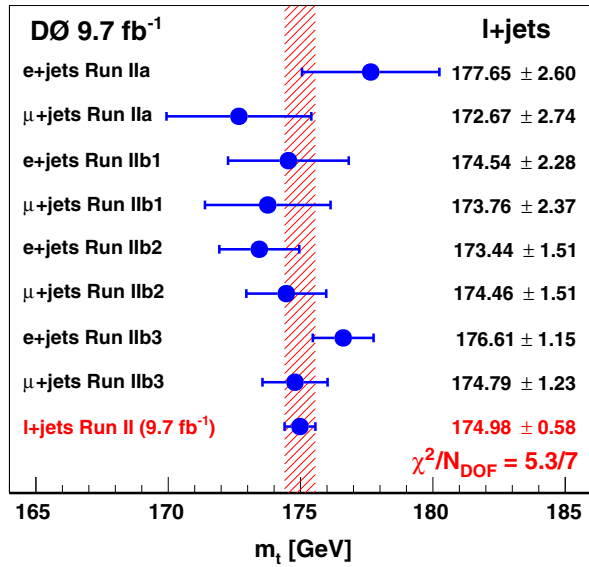
FIG. 19 (color online). Summary of the measured m_t values with their statistical uncertainties for each data-taking epoch and split according to final state. The red-shaded band indicates the statistical uncertainty on the combined m_t value in Run II data corresponding to 9.7 fb^{-1} of integrated luminosity.

FIG. 21 (color online). Same as Fig. 20, in μ + jets final states in (a) Run IIa, (b) Run IIb1, (c) Run IIb2, and (d) Run IIb3.

and final state are consistent within their statistical (stat + JES) uncertainties, we calculate the value of the χ^2 distribution for 7 degrees of freedom, which yields a probability of 62%.

The measured k_{JES} values are shown in Fig. 22 together with their statistical uncertainties. We also compare the observed values of $\sigma_{k_{JES}}$ with expectations from simulation, and find consistency. We obtain a combined value of $k_{JES} = 1.025 \pm 0.005 (\text{stat} + m_t)$ by applying Eq. (37) after replacing $k_{JES} \leftrightarrow m_t$. The individual measured k_{JES} are consistent with a χ^2 probability of 54%. The total JES uncertainty for $t\bar{t}$ events after all selections is between 2.0% and 2.1%, depending on the epoch, consistent with our measured k_{JES} at the level of 1.3 standard deviations (SD). Due to the busy environment of $t\bar{t}$ events containing four jets, a higher fraction of the event's energy is expected in jet cones

FIG. 20 (color online). Distribution of expected statistical uncertainties σ_{m_t} in e + jets final states in (a) Run IIa, (b) Run IIb1, (c) Run IIb2, and (d) Run IIb3, obtained in 1000 PEs at $m_t^{\text{gen}} = 172.5$ GeV and $k_{JES} = 1$, after calibrating for nonunit width of the distribution in π_{m_t}. The observed statistical uncertainties in data are indicated by arrows.

FIG. 22 (color online). Same as Fig. 19, but for the k_{JES} parameter.

FIG. 23 (color online). Two-dimensional likelihood $\mathcal{L}(\mathbb{X}_N; m_t, k_{\mathrm{JES}})/\mathcal{L}_{\max}$ for data. Fitted contours of equal probability are overlaid as solid lines. The maximum is marked with a cross. Note that the bin boundaries do not necessarily correspond to the grid points on which $\mathcal{L}$ is calculated.

leading to a higher k_{JES} according to Eq. (16)), which is not the case in $\gamma + $ jet and dijet samples where the JES is derived.

Figure 23 presents the two-dimensional likelihood density in (m_t, k_{JES}), which is obtained by multiplying the calibrated likelihood densities for each data-taking epoch and each final state. We compare the m_t and k_{JES} values obtained from the minimum of the double-Gaussian fit to the two-dimensional likelihood density in Fig. 23 and find them to match at the level of 10^{-4}. In Fig. 24 we compare the observed statis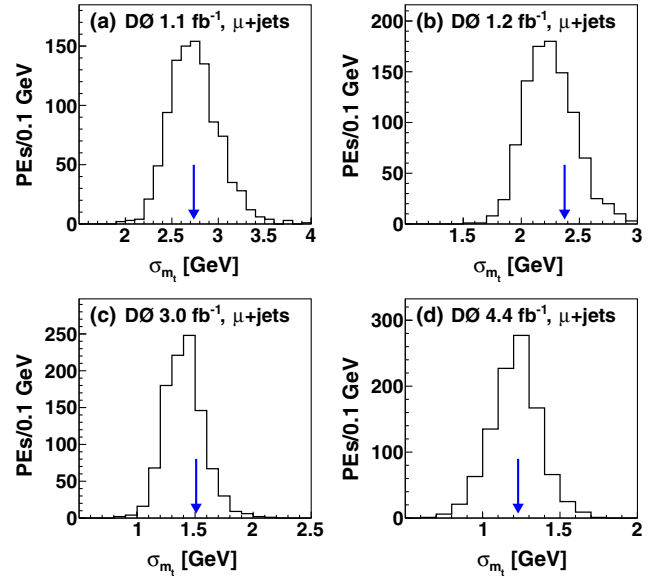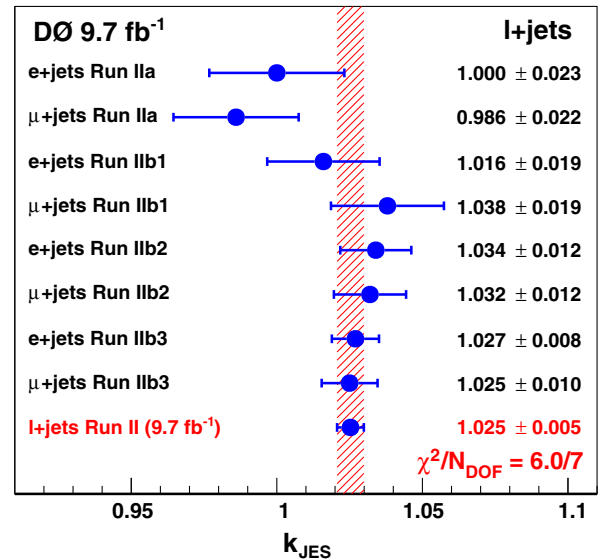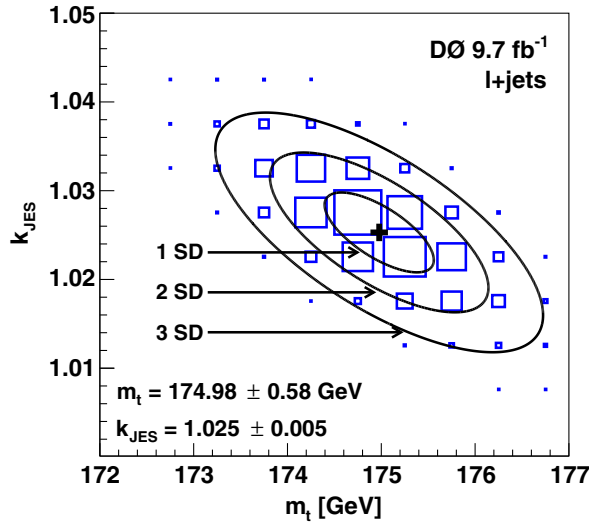tical uncertainties on m_t and k_{JES} with expectations from PE studies using $t\bar{t}$ samples for $m_t^{\mathrm{gen}} = 172.5$ GeV and $k_{\mathrm{JES}}^{\mathrm{gen}} = 1$. The observed uncertainty is consistent with the expectation.

The values of m_t and k_{JES} measured in $e + $ jets and $\mu + $ jets final states using 9.7 fb^{-1} of integrated luminosity are
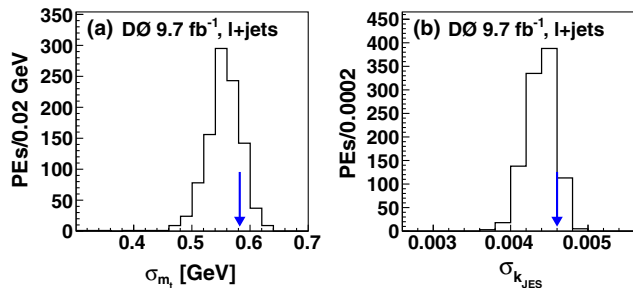
FIG. 24 (color online). (a) Distribution of the expected uncertainty on m_t, as obtained using PEs where the $t\bar{t}$ contribution is taken at $m_t^{\mathrm{gen}} = 172.5$ GeV and $k_{\mathrm{JES}} = 1$, after calibration. The observed statistical uncertainty is indicated by an arrow. (b) Same for uncertainty on k_{JES}.
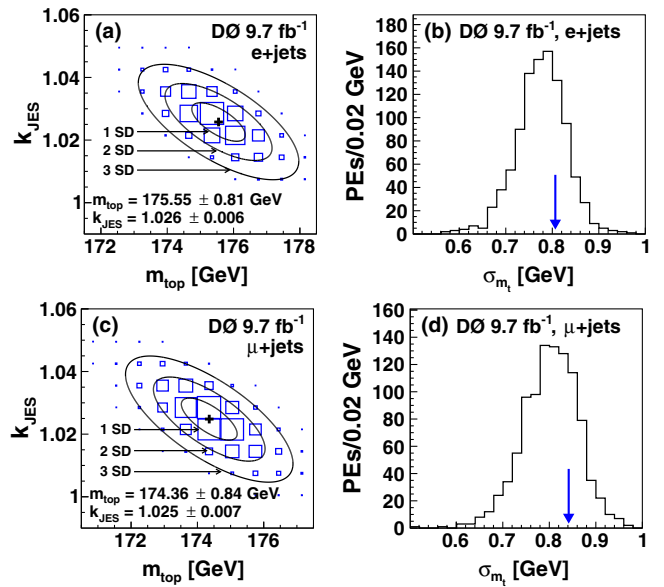
FIG. 25 (color online). (a) Two-dimensional likelihood $\mathcal{L}(\mathbb{X}_N; m_t, k_{\mathrm{JES}})/\mathcal{L}_{\max}$ for data in the $e + $ jets final state. Fitted contours of equal probability are overlaid as solid lines. The maximum is marked with a cross. (b) Distribution in expected uncertainty on m_t in $e + $ jets final states, obtained using PEs where the $t\bar{t}$ contribution is taken at $m_t^{\mathrm{gen}} = 172.5$ GeV and $k_{\mathrm{JES}} = 1$, after calibration. The observed statistical uncertainty in data is indicated by the arrow. (c) Same as (a), but for the $\mu + $ jets channel. (d) Same as (b), but for the $\mu + $ jets channel.

$$m_t^{e+\mathrm{jets}} = 175.55 \pm 0.81 \ (\mathrm{stat} + \mathrm{JES}) \ \mathrm{GeV},$$
$$k_{\mathrm{JES}}^{e+\mathrm{jets}} = 1.026 \pm 0.006 \ (\mathrm{stat} + m_t),$$
$$m_t^{\mu+\mathrm{jets}} = 174.36 \pm 0.84 \ (\mathrm{stat} + \mathrm{JES}) \ \mathrm{GeV},$$
$$k_{\mathrm{JES}}^{\mu+\mathrm{jets}} = 1.025 \pm 0.007 \ (\mathrm{stat} + m_t).$$

The corresponding two-dimensional likelihood densities in (m_t, k_{JES}) and the comparison between the expected statistical uncertainty for each final state and the observation are shown in Fig. 25. The results in $e + $ jets and $\mu + $ jets channels are consistent at the level of 1 SD considering just statistical uncertainties, and the corresponding p value is 0.30.

We repeat the measurement assuming $k_{\mathrm{JES}} = 1$, i.e., by evaluating the one-dimensional likelihood $\mathcal{L}(\mathbb{X}_N; m_t, k_{\mathrm{JES}} \equiv 1)$, and find $m_t^{k_{\mathrm{JES}} \equiv 1} = 176.88 \pm 0.41$ GeV, which is consistent with the final results obtained by maximizing $\mathcal{L}(\mathbb{X}_N; m_t, k_{\mathrm{JES}})$ as a function of (m_t, k_{JES}), considering the measured k_{JES}. Separating the statistical uncertainty σ_{m_t} into two components, one from m_t and the other from k_{JES}, we obtain $m_t = 174.98 \pm 0.41(\mathrm{stat}) \pm 0.41(\mathrm{JES})$ GeV.

In contrast to the previous measurement [14], we do not use the JES determined in exclusive $\gamma + $ jet and dijet events with an uncertainty of $\approx 2\%$ to constrain k_{JES}. We follow this strategy because the statistical uncertainty on the

measured k_{JES} value is smaller than the typical uncertainty on the JES and because k_{JES} relates jet energies at detector level to parton energies, while JES relates jet energies at detector level to jet energies at particle level.

C. Comparison of data with simulations using the measured f, m_t, and k_{JES} values

In this section, we demonstrate that our simulations agree with the data for the measured m_t and k_{JES} parameters. We use a sample of simulated $t\bar{t}$ events at $m_t^{gen} = 175$ GeV and scale the energies of jets by $k_{JES} = 1.025$, while adjusting the magnitude of the three-momentum $|\vec{p}|$

to preserve the invariant mass of the jet. The fraction of signal events, f, is set to our measured values of 63% in the $e + $ jets and 70% in the $\mu + $ jets final states (cf. Sec. VI B). We consider the same systematic uncertainties as in Sec. IV: JES, jet energy resolution, jet identification, flavor dependence of the detector response, b tagging, lepton identification, lepton momentum scale, trigger, as well as hadronization and higher-order effects for $t\bar{t}$ events.

Distributions in the invariant mass of the $t\bar{t}$ system and in the invariant mass of the jet pair matched to one of the W bosons are shown in Figs. 26(c)–26(d)
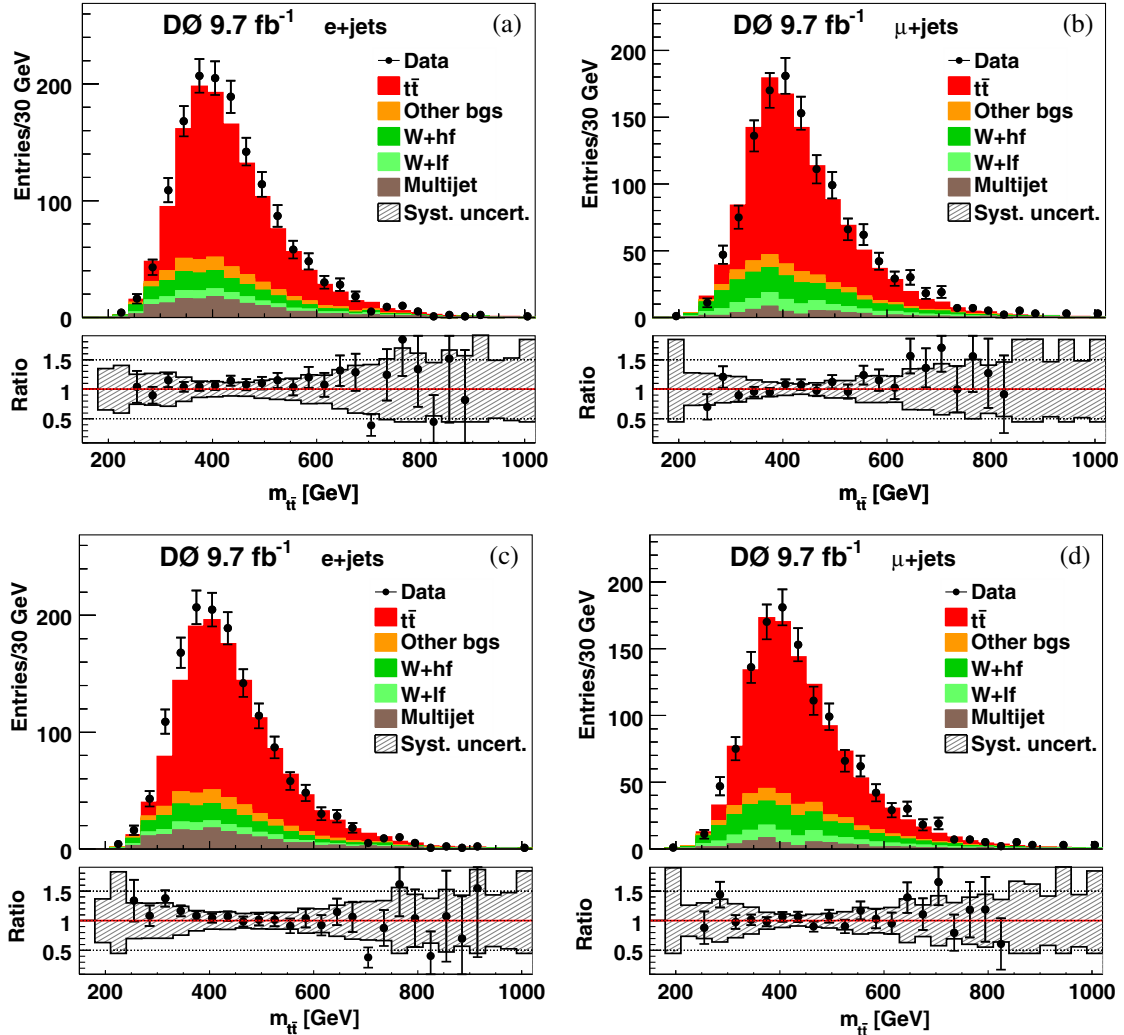
FIG. 26 (color online).   The invariant mass of the $t\bar{t}$ system in the (a) $e + $ jets and (b) $\mu + $ jets final states, assuming $m_t^{gen} = 172.5$ GeV, $k_{JES} = 1$, and $\sigma_{t\bar{t}} = 7.24$ pb^{-1} [40]. The same observable in the (c) $e + $ jets and (d) $\mu + $ jets final states for $m_t^{gen} = 175$ GeV, with energies of jets scaled up by $k_{JES} = 1.025$, corresponding to their measured values. The fractions of signal events, f, are set to their measured values of 63% in the $e + $ jets and 70% in the $\mu + $ jets final states in (c) and (d) (cf. Sec. VI B). The category "Other bgs" encompasses $Z + $ jets, WW, WZ, ZZ, and single top quark production, as well as dileptonic $t\bar{t}$ decays. The production of a W boson in association with at least one b or c quark is denoted as "$W + $ hf", while "$W + $ lf" stands for all other flavor configurations. The last bin includes overflow events. The ratio shows the number of observed events divided by the number of expected events in a given bin. The band of systematic uncertainty is indicated by the shaded area in the ratio plots, and includes contributions from dominant sources: JES, jet energy resolution, jet identification, flavor dependence of the detector response, b tagging, lepton identification, lepton momentum scale, trigger, as well as hadronization and higher-order effects for $t\bar{t}$ events.

and Figs. 27(c)–27(d), respectively, together with the predictions from our signal and background models. The observables $m_{t\bar{t}}$ and M_W are reconstructed with the same algorithm as described in Sec. IV. As expected, the agreement between data and simulations improves compared to Figs. 26(a)–26(b) and Figs. 27(a)–27(b) when we use the measured values of f, m_t, and k_{JES}.

In Fig. 28, we study the distribution in H_T, which is defined as the scalar sum of E_T of the four jets, the transverse momentum of the $t\bar{t}$ system, and the transverse momentum of the top quarks. The observable $p_T^{t\bar{t}}$ is given by the transverse coordinates of the four-momentum vector used to calculate $m_{t\bar{t}}$, while p_T^{top} is obtained from the four-momenta of final state particles used to reconstruct $m_{t\bar{t}}$. These are combined to give the four-momenta of the t and $\bar{t}$ quarks that minimize the $|m_t - m_{\bar{t}}|$ mass difference.

The transverse momenta of the electrons and muons, the distributions of $\not{p}_T$, and the transverse mass of the $W \to \ell\nu_\ell$ decay are shown in Fig. 29. The invariant of the trijet system matched to the hadronic decay of the top quark, reconstructed from the same four-momenta used in the reconstruction of $m_{t\bar{t}}$ and M_W, is shown in Fig. 30. Notable improvement due to reduced backgrounds is observed relative to the Run I measurement [62].

Good agreement between data and simulations is observed in all variables except $p_T^{t\bar{t}}$, where ALPGEN + PYTHIA predicts fewer events with $p_T^{t\bar{t}} < 10$ GeV than observed in data, for which a systematic uncertainty is evaluated in Sec. VIII A 2. The variable p_T^{top}, for which agreement within uncertainties is observed, is shown at detector level. However, some discrepancy between measured $d\sigma_{t\bar{t}}/dp_T^{\mathrm{top}}$ corrected for detector effects, and SM calculations is present in our data [34].
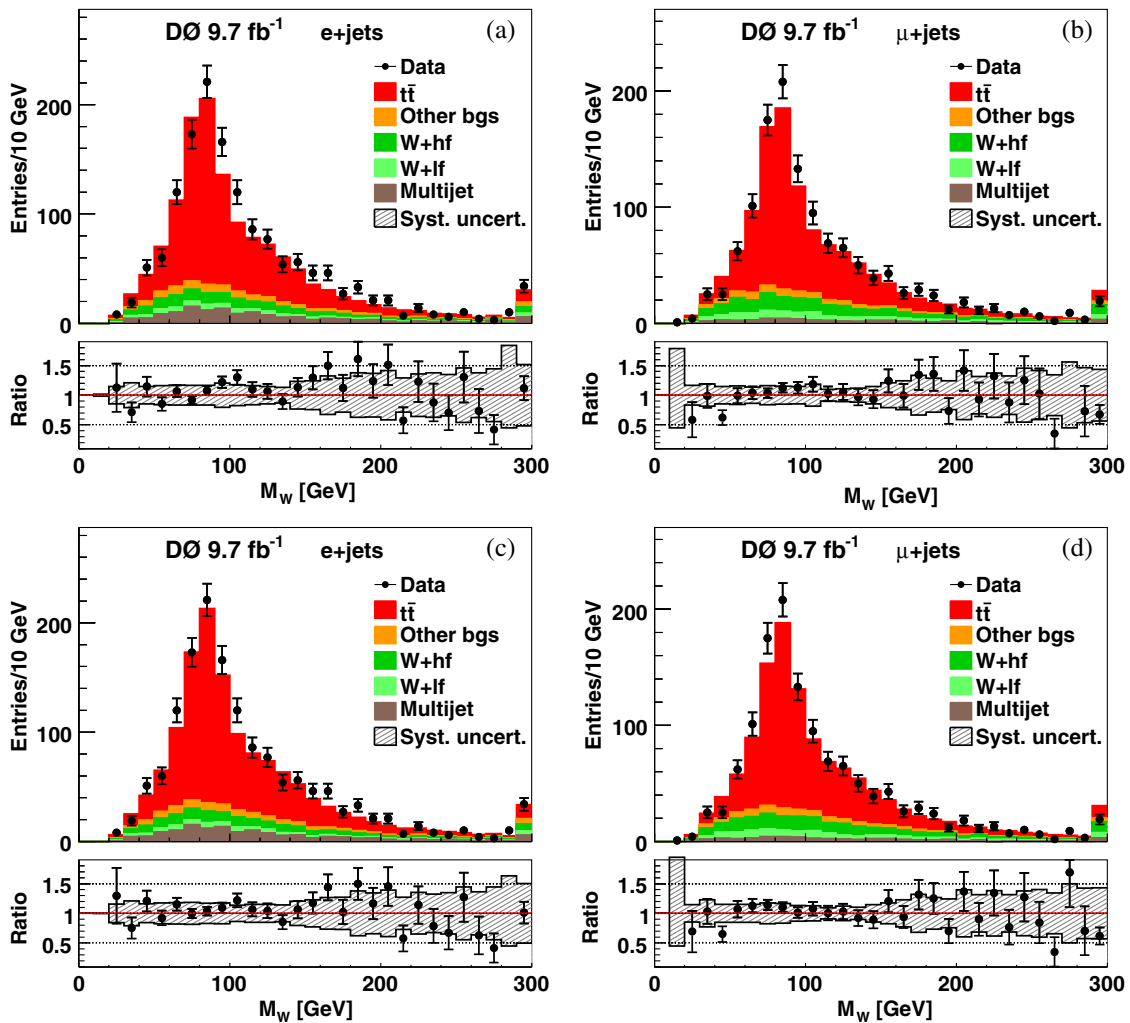
FIG. 27 (color online). Same as Fig. 26, but for the invariant mass of the dijet system matched to the W boson, assuming $m_t^{\mathrm{gen}} = 172.5$ GeV, $k_{\mathrm{JES}} = 1$, and $\sigma_{t\bar{t}} = 7.24$ pb^{-1} [40] in the (a) e + jets and (b) μ + jets final states, and for $m_t^{\mathrm{gen}} = 175$ GeV, $k_{\mathrm{JES}} = 1.025$, and f corresponding to their measured values in the (c) e + jets and (d) μ + jets final states.
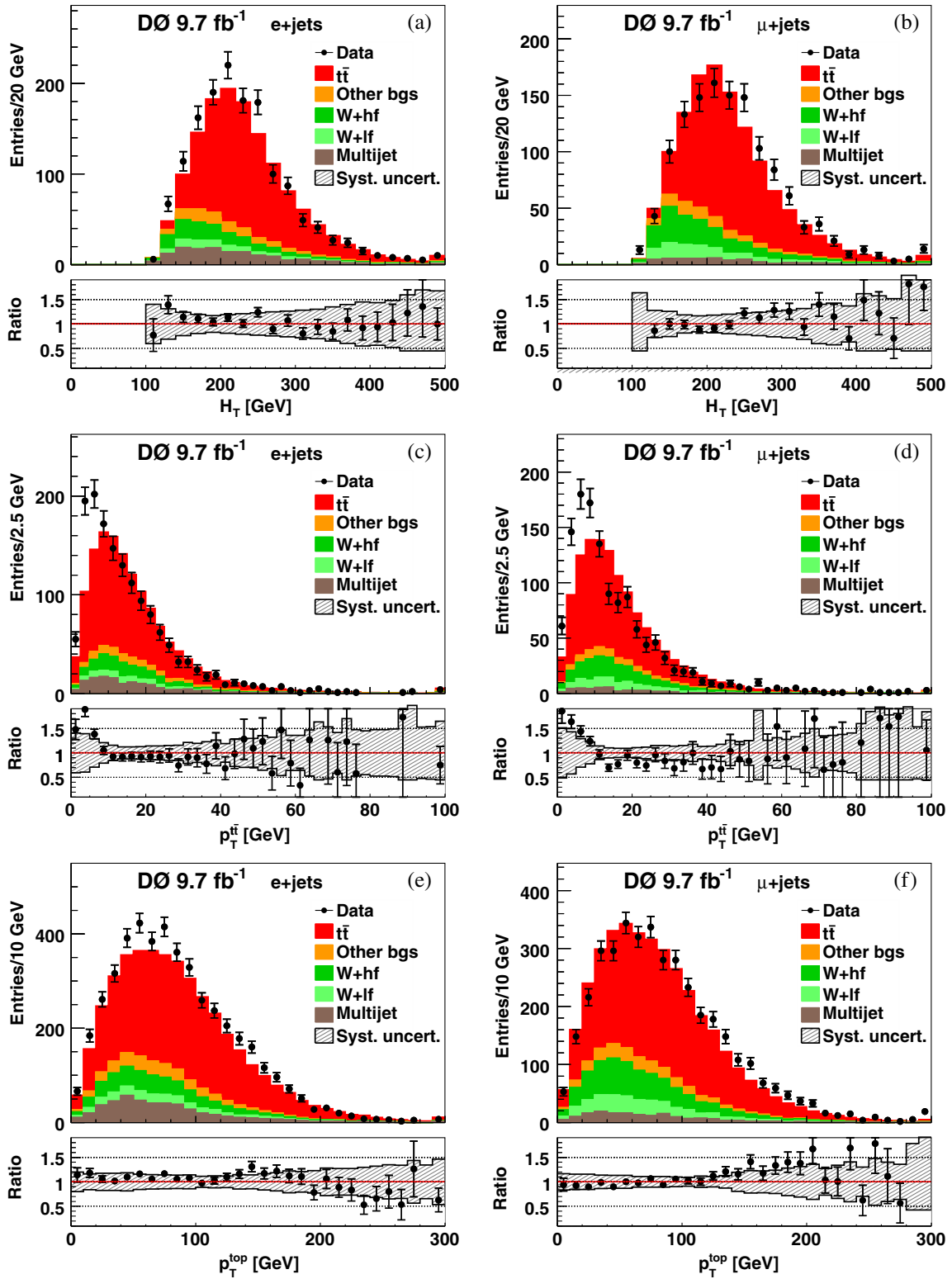
FIG. 28 (color online).   The scalar sum of E_T of the four jets H_T in (a) $e +$ jets and (b) $\mu +$ jets final states, for the transverse momentum of the $t\bar{t}$ system in (c) $e +$ jets and (d) $\mu +$ jets final states, as well as for the transverse momentum of the top quarks in (a) $e +$ jets or (b) $\mu +$ jets final states. All panels are for $m_t^{\mathrm{gen}} = 175$ GeV, with energies of jets scaled up by $k_{\mathrm{JES}} = 1.025$, corresponding to their measured values. The fractions of signal events, f, are set to their measured values of 63% in the $e +$ jets and 70% in the $\mu +$ jets final states in (c) and (d) (cf. Sec. VI B). The list of included background contributions and sources of systematic uncertainties considered are identical to those from Fig. 26. Panels (e) and (f) have two entries per event, one for each of the t and $\bar{t}$ quarks.
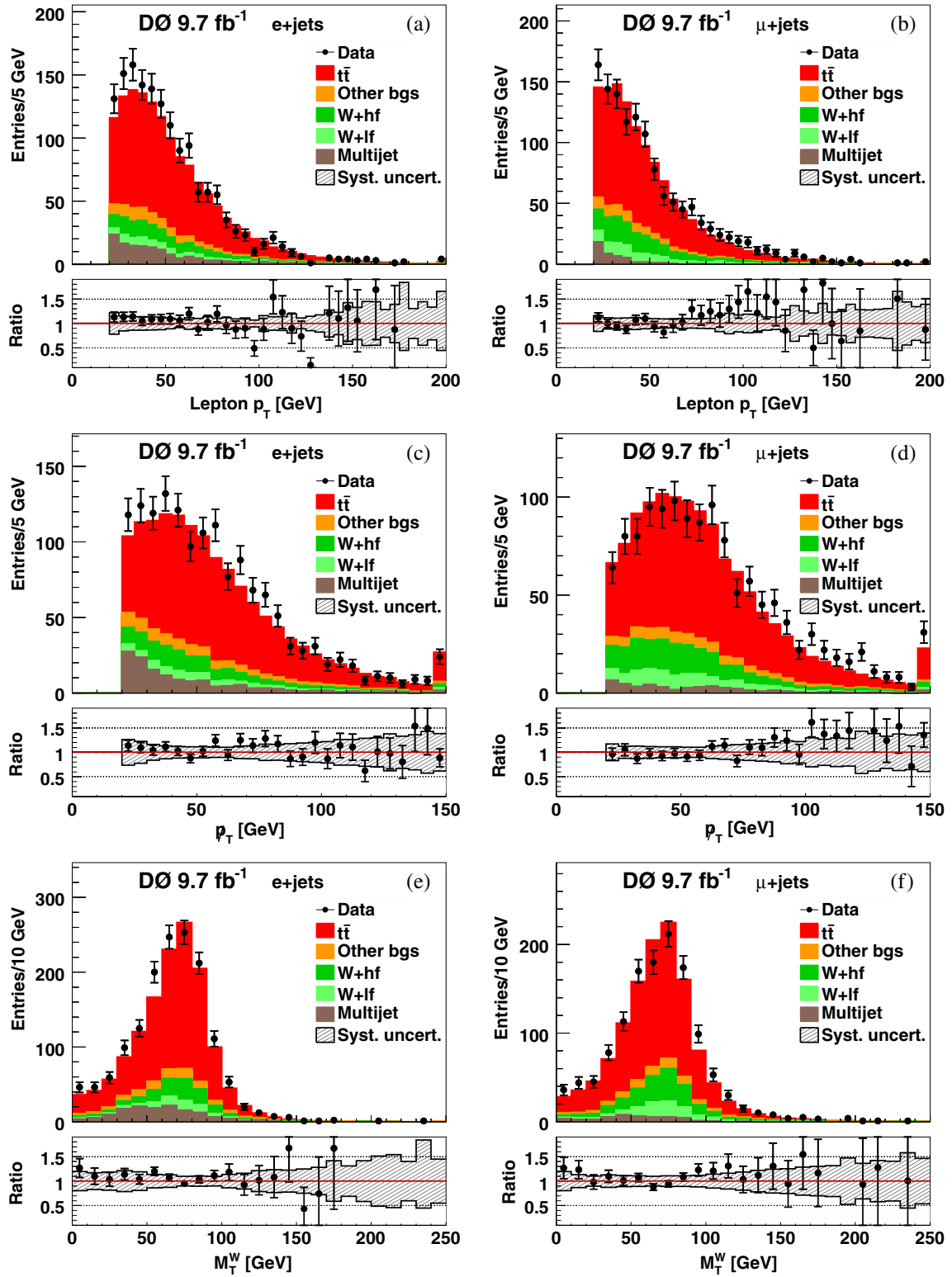
FIG. 29 (color online).   Same as Fig. 28, but for the transverse momentum of the (a) electron or (b) muon, for the missing transverse momentum in (c) e + jets and (d) μ + jets final states, as well as for the transverse mass of the $W \to \ell\nu_\ell$ decay in (e) e + jets and (f) μ + jets final states.
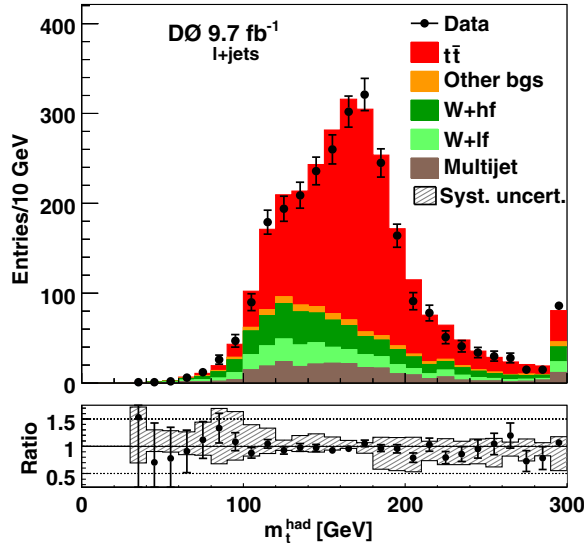
FIG. 30 (color online).   Same as Fig. 28, but for the invariant mass of the trijet system matched to the hadronic decay of the top quark in $\ell +$ jets final states.

VIII. SYSTEMATIC UNCERTAINTIES

Systematic uncertainties are evaluated using sets of PEs constructed from simulated signal and background events, for three categories of sources:

(i) modeling of signal and background events,
(ii) simulation of the detector response, and
(iii) analysis procedures and assumptions.

The contributions from these sources listed in Table V are evaluated individually and combined in quadrature to obtain the total systematic uncertainty.

All sources of systematic uncertainties are considered fully correlated between $e +$ jets and $\mu +$ jets final states, except for the uncertainties from the lepton momentum scale and the calibration of the method. In comparison to the previous analysis using 3.6 fb^{-1} of integrated luminosity [14], the number of simulated $t\bar{t}$ events used for the calibration of the ME technique and for the evaluation of systematic uncertainties has increased significantly since the computation time for P_{sig} has been reduced by two orders of magnitude, as discussed in Sec. V F. As a result, the statistical components of systematic uncertainties are ≈ 0.05 GeV in each of the first four sources listed in Table V, namely those from higher-order corrections, initial and/or final-state radiation, hadronization and the underlying event (UE), and color reconnection, and are ≈ 0.01 GeV for the heavy-flavor scale factor, residual jet energy scale, flavor-dependent response to jets, lepton momentum scale, jet energy resolution, jet identification efficiency, and modeling of multijet events. The statistical components are negligible for all the other sources of systematic uncertainty. The uncertainties from the first four sources are evaluated for $m_t^{\text{gen}} = 172.5$ GeV and $k_{\text{JES}}^{\text{gen}} = 1$ by comparing results for m_t using different models for

TABLE V.   Summary of uncertainties on the measured m_t. One-sided sources of uncertainty or sources dominated by a one-sided component are signed, indicating the direction of m_t change when using an alternative instead of the central model. Two-sided uncertainties or uncertainties dominated by a two-sided component are marked with a $\pm$ or $\mp$ symbol.

Source of uncertainty	Effect on m_t (GeV)
Signal and background modeling:	
Higher-order corrections	$+0.15$
Initial/final state radiation	∓ 0.06
Transverse momentum of the $t\bar{t}$ system	-0.07
Hadronization and underlying event	$+0.26$
Color reconnection	$+0.10$
Multiple $p\bar{p}$ interactions	-0.06
Heavy-flavor scale factor	∓ 0.06
Modeling of b-quark jet	$+0.09$
Parton distribution functions	± 0.11
Detector modeling:	
Residual jet energy scale	± 0.21
Flavor-dependent response to jets	∓ 0.16
Tagging of b jets	∓ 0.10
Trigger	± 0.01
Lepton momentum scale	± 0.01
Jet energy resolution	± 0.07
Jet identification efficiency	-0.01
Method:	
Modeling of multijet events	$+0.04$
Signal fraction	± 0.08
MC calibration	± 0.07
Total systematic uncertainty	± 0.49
Statistical uncertainty	± 0.58
Total uncertainty	± 0.76

signal. All other systematic uncertainties are evaluated by applying a recalibration using simulations that reflect an alternative model to data. The statistical components due to the finite number of simulated events are never larger than the net difference between the central and alternative models for any of the sources of systematic uncertainty.

Unless stated otherwise, the systematic uncertainties are evaluated using fully simulated events. Background events are always included, as described in Secs. VI A and VII A. The signal fraction used to compose PEs is kept fixed at the value obtained for that data-taking epoch and final state, as summarized in Table IV, except in evaluating the systematic uncertainty from f. The systematic uncertainties from category (iii), which are associated with analysis procedures and assumptions, are evaluated including the MJ background in the ensemble tests. The estimate of all other systematic uncertainties is not expected to be affected by the inclusion of the MJ background contribution in the ensemble tests, which is therefore neglected. We quote signed uncertainties for one-sided sources of uncertainty or sources dominated by a one-sided component in Table V, indicating the direction of m_t change when using an alternative instead of the central model. Two-sided

uncertainties or uncertainties dominated by a two-sided component are marked with a $\pm$ or $\mp$ symbol. For one-sided sources of systematic uncertainty, the full magnitude of the effect is taken in each direction when calculating the total quadrature sum to obtain the total systematic uncertainty, in accordance with Ref. [7].

A. Signal and background modeling

1. Higher-order corrections

We calibrate the response of the ME technique using $t\bar{t}$ events generated with the LO ALPGEN program, which accounts for real corrections to the Born level process up to second-order in α_s through the ME, i.e., for 0, 1, or 2 additional light partons. To evaluate the effect of higher-order virtual corrections on m_t, we use signal events generated with the MC@NLO program [18], which calculates the processes $q\bar{q} \to t\bar{t}$, $gg \to t\bar{t}$, and $qg \to t\bar{t}$ at NLO, as an alternative model. Because MC@NLO is interfaced to HERWIG [63] for simulating the contributions from leading-logarithmic (LL) corrections and fragmentation to the hard process of interest, we use ALPGEN + HERWIG events as the central model for this comparison to avoid double-counting the uncertainty from a different showering model. Performing the ensemble tests for $m_t = 172.5$ GeV, we find a shift of $+0.15$ GeV, which we assign as the systematic uncertainty due to higher-order corrections.

2. Initial/final state radiation

The modeling of extra jets from initial/final state radiation (ISR/FSR) can affect the measurement of m_t. To evaluate the contribution from this source, we adjust the amount of radiation by changing the `ktfac` parameter [64] that defines the renormalization scale in the CKKW scale-setting procedure, from its standard value of `ktfac = 1` in our ALPGEN + PYTHIA simulations described in Sec. III, as suggested in Ref. [64]. We constrain changes in the amount of ISR/FSR by studying the cross section for Drell-Yan events ($q\bar{q} \to Z/\gamma^* \to \ell^+\ell^-$) measured differentially in the ϕ^* variable [65], which is related to the p_T of the Z/γ^* boson, and has sensitivity to the amount of QCD radiation. Our studies, documented in Appendix A, indicate that changes in the `ktfac` parameter by a factor of ± 1.5 cover the excursion of MC simulations from data, which results in an uncertainty of ∓ 0.06 GeV on m_t. Previously, the systematic uncertainty from modeling of ISR/FSR was evaluated using a pure LO generator, PYTHIA, and changes made in shower-evolution parameters. The new procedure is more accurate, as it uses a larger data sample for deriving the ISR/FSR dependence, and employs the same generator setup as for simulating the default $t\bar{t}$ sample.

3. Transverse momentum of the $t\bar{t}$ system

The distribution in the transverse momentum of the $t\bar{t}$ system, $p_T^{t\bar{t}}$, is not modeled well as shown in Fig. 28, and a dedicated systematic uncertainty is assigned. This mis-modeling is corrected by reweighting the contribution from $t\bar{t}$ events differentially in $p_T^{t\bar{t}}$ to achieve agreement between the simulations and data. Propagating this effect to m_t using ensemble tests, we find a shift of -0.07 GeV.

4. Hadronization and underlying event

The choice of a model for the parton-shower (PS) evolution, the hadronization, and the underlying event (UE) can lead to a bias on the measured m_t value. To evaluate the size of this effect, we compare MC samples where PS evolution, hadronization, and UE are simulated using PYTHIA with HERWIG as an alternative model. In both cases, the ALPGEN generator is used to simulate the hard process. The comparison of ALPGEN + HERWIG with ALPGEN + PYTHIA will give a convolution of four terms:

  (i) a statistical component due to the limited size of the MC samples,

 (ii) a difference in kinematic spectra, most notably in $p_T^{t\bar{t}}$, between ALPGEN+HERWIG and ALPGEN+PYTHIA,

(iii) a difference in the response of the detector to jets simulated with HERWIG and PYTHIA, and

(iv) a difference in the modeling of the PS evolution, hadronization, and UE when using ALPGEN + HERWIG and ALPGEN + PYTHIA.

We are interested in the effect from source (iv), since (ii) is already accounted for in the systematic uncertainty from modeling of ISR/FSR, and (iii) is taken into account in the systematic uncertainties from modeling of the detector response. We reduce the contributions from sources (i), (ii), and (iii) as follows:

  (i) The contribution from source (i) is reduced to ≈ 0.05 GeV, about a factor of five smaller than the previous m_t measurement [14], by increasing the size of MC samples by a factor of ≈ 25.

 (ii) Reshuffling of momenta between the hard and soft part of the event [66] causes the $p_T^{t\bar{t}}$ distribution in ALPGEN + HERWIG to differ significantly from ALPGEN + PYTHIA, as shown in Fig. 31. To isolate this effect in the evaluation of the systematic uncertainty, we reweight ALPGEN + PYTHIA in $p_T^{t\bar{t}}$ to match the ALPGEN + HERWIG simulation, which results in a shift of 0.05 GeV in m_t. The uncertainty from modeling of transverse momentum of the $t\bar{t}$ system already accounts for the potential impact on m_t of this difference, as discussed in Sec. VIII A 3.

(iii) The JES calibration is derived using PYTHIA with D0 tune A [15], and is therefore valid only for this specific configuration. The contribution from source (iii) would not be present if a dedicated JES derived with HERWIG was available. Like the default JES calibration using PYTHIA, the alternative calibration using HERWIG would be affected by similar uncertainties accounted for in the "detector modeling"
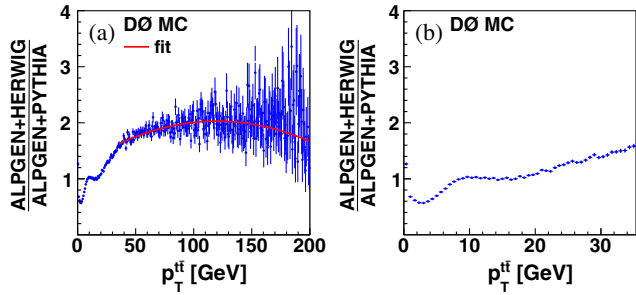
FIG. 31 (color online).   (a) The ratio of predicted differential cross sections from ALPGEN + HERWIG to those from ALPGEN + PYTHIA as a function of $p_T^{t\bar{t}}$ at particle level. Also shown is the fit with a second-order polynomial used for reweighting ALPGEN + PYTHIA events in $p_T^{t\bar{t}}$ for 35 GeV $< p_T^{t\bar{t}} < 200$ GeV. Below that range the reweighting is performed according to the histogram, and above with a constant factor of 1.67. Uncertainties are only statistical. (b) Same ratio in the range $p_T^{t\bar{t}} < 35$ GeV.

category of Table V. Including the difference of the JES derived with PYTHIA and HERWIG in the evaluation of the uncertainty from the choice PS evolution, hadronization, and UE models would lead to double-counting. To eliminate the contribution from the response of the detector, we use particle-level jet energies. The standard selection as described in Sec. IV is applied at detector level to take into account any potential effects from the trigger or selection requirements, and the detector-level jets are matched to particle-level jets. The matching is done in (η, ϕ) space, using the requirement of $\Delta R(j_{\text{detector}}, j_{\text{particle}}) < R_{\text{cone}}/2 = 0.25$. The energy of each detector-level jet is replaced by the energy of the matched particle-level jet, and the magnitude of the three-momentum $|\vec{p}|$ of the detector-level jet is adjusted to preserve its original η, ϕ, and m parameters. Those modified four-momenta of jets are then used, together with all other detector-level information in the event, to extract m_t with the ME technique just as in data.

Reducing the contribution from source (i), and factorizing out contributions from sources (ii) and (iii), as described above, we find an effect of $+0.26$ GeV from the choice of the model for PS evolution, hadronization, and UE. We verify that $k_{\text{JES}}^{\text{ALPGEN+HERWIG}}$ and $k_{\text{JES}}^{\text{ALPGEN+PYTHIA}}$ are consistent within uncertainties, as expected at particle level, indicating that the effect of JES has been factorized out.

As a cross-check, we also evaluate the impact of a different PS model and a change in the models for hadronization and UE by comparing $t\bar{t}$ events simulated with ALPGEN and interfaced to either PYTHIA with D0 tune A (the standard MC setup), or PYTHIA with the Perugia 2011C tune [67]. While the former is based on a Q^2 ordered PS model, the latter is p_T^2 ordered [28,29]. Furthermore, the

latter is a recent tune from the Perugia 2011 family that includes LHC data, which is recommended for this comparison [68]. Both use the CTEQ6L1 set of PDFs. We verify that the Perugia 2011 family describes the transverse jet shapes sufficiently well and is therefore applicable to Tevatron data dominated by quark jets, despite being tuned including LHC data dominated by wider gluon jets. For simplicity, we carry out the comparison between PYTHIA with D0 tune A and PYTHIA with Perugia 2011C at detector level, and find a change of $+0.30$ GeV in m_t, which serves as an upper estimate of the effect evaluated with particle-level jet energies, as for the comparison of ALPGEN + HERWIG with ALPGEN + PYTHIA.

5. Color reconnection

Our standard PYTHIA tune, D0 tune A, does not include an explicit model for color reconnection (CR). Color reconnection is sometimes confused with strong color correlation between the hard scattering process and the underlying event. The latter is an integral part of PYTHIA D0 tune A, as not including it would violate confinement. Recently, research has been carried out to include CR in PYTHIA [69]. To evaluate the CR effect, we compare identical ALPGEN events interfaced to PYTHIA with two different tunes, Perugia 2011 and Perugia 2011NOCR. While the former tune includes an explicit CR model, the latter does not. The Perugia 2011 tune rather than Perugia 2011C is used as an alternative model because Perugia 2011 uses the same set of CTEQ5L PDFs as the reference model Perugia 2011NOCR, while Perugia 2011C uses CTEQ6L1. This choice of generator setup is advised in Ref. [68], since Perugia includes a better, more phenomenologically-motivated CR model than the ACRpro tune [70]. The new tune models the color-string survival probability depending on the distance in rapidity between the beginning and the end of the color string, whereas the previous model uses only an overall approximation. We find an effect of $+0.10$ GeV on m_t from this source of systematic uncertainty.

To cross-check the impact of modeling of multiple parton interactions (MPI) on the measurement, we compare events generated with ALPGEN interfaced to PYTHIA with the Perugia 2011mpiHi and Perugia 2011 tunes, where the former features harder MPI, albeit at a smaller rate, compared to the latter. We find an effect of 0.14 GeV, with a statistical component of ≈ 0.15 GeV due to limited MC event statistics. Since HERWIG and PYTHIA use different models for MPI, an uncertainty from the choice of a model for MPI is already included in the uncertainty from modeling of hadronization and the UE discussed in Sec. VIII A 4. In addition, it is at least partly included in the comparison between the Perugia 2011 and Perugia 2011NOCR tunes discussed above, since the latter, without CR, must simultaneously adjust the amount of MPI to

describe data. Therefore, the comparison between Perugia 2011mpiHi and Perugia 2011 is treated as a cross-check.

6. Multiple $p\bar{p}$ interactions

Multiple $p\bar{p}$ interactions can potentially influence the measurement of m_t. We reweight the spectrum in instantaneous luminosity of our simulated MC samples to the instantaneous luminosity profile found in data for the respective data-taking epoch and final state. This default correction is derived for each data-taking stream, while the instantaneously luminosity profile in a subset of this data can differ due to the trigger and selection requirements. To evaluate this systematic uncertainty, we obtain an alternative calibration where an additional reweighting in instantaneous luminosity is applied after all selections to bring its spectra in $t\bar{t}$ simulations and in data into agreement. We find a change in m_t of -0.06 GeV.

7. Heavy-flavor scale factor

As mentioned in Sec. III, a heavy-flavor scale factor of $k_{bb,cc} = 1.47$ is applied to the $Wb\bar{b}$ and $Wc\bar{c}$ cross sections to correct the heavy-flavor content of the $W + $ jets MC samples to expectations from NLO calculations. The uncertainty on $k_{bb,cc}$ is $\approx 15\%$ [34]. Moreover, there is an additional uncertainty of $\approx 12\%$ on the $W + c$ content of the sample [34]. These uncertainties are combined linearly and rounded to 30%. The effect of $k_{bb,cc}$ variations is propagated to m_t using PEs. This introduces variations in the kinematic distributions of the combined contribution from $W + $ jets production. As we are interested only in the effect of the changed background composition, we do not change f when constructing the pseudo-experiments. We find an effect of ∓ 0.06 GeV due to this source of systematic uncertainty.

8. Modeling of b-quark jet

Uncertainties in the simulation of b quark fragmentation can affect the measurement of m_t through several aspects of the analysis such as b tagging and the TF. Such effects are studied by reweighting the simulated $t\bar{t}$ events according to other possible fragmentation models for b quarks. The standard $t\bar{t}$ MC samples consist of events reweighted from the standard PYTHIA b fragmentation function to a Bowler scheme [71] that has been tuned to LEP (ALEPH, OPAL, and DELPHI) data [72]. To evaluate the potential bias from this source, $t\bar{t}$ events are further reweighted to account for differences in SLD [72] and LEP data, resulting in a shift of $+0.08$ GeV in the measured m_t.

The detector response to b-quark jets can be different in the presence of semileptonic decays of b or c quarks. The incorrect simulation of semileptonic branching ratios in b and c quark decays can thus result in a systematic effect on m_t. We take an uncertainty of 0.05 GeV determined in Ref. [48] as the contribution from this source. Quadratically

combining the two sources of uncertainty, we find a shift in m_t of $+0.09$ GeV.

9. Parton distribution functions

To evaluate the uncertainty from the choice of PDFs, the standard ALPGEN + PYTHIA sample at $m_t^{\text{gen}} = 172.5$ GeV is reweighted to match possible excursions in the PDF parameters provided in CTEQ6M [33]. Ensemble tests are repeated for each of these changes and the total uncertainty is evaluated using the following formula [33]:

$$\delta_{m_t} = \frac{1}{2} \left\{ \sum_{i=1}^{20} [\Delta m_t(S_i^+) - \Delta m_t(S_i^-)]^2 \right\}^{\frac{1}{2}}, \quad (38)$$

where the sum runs over PDF uncertainties in the positive (S_i^+) and negative (S_i^-) excursions. We find changes in m_t of ± 0.11 GeV due to this source of systematic uncertainty. The effect on m_t from replacing the central PDF set from CTEQ6M by that from CTEQ6L1 is much smaller.

B. Detector modeling

1. Residual jet energy scale

The overall jet energy scale factor k_{JES} is fitted simultaneously with m_t, and the corresponding contribution to the statistical uncertainty is included in σ_{m_t}. However, k_{JES} does not account for possible effects from uncertainties in the JES corrections that are differential in E or η of the jet. To estimate the potential bias on m_t from the residual JES uncertainty, we use a variety of approaches:

  (i) As for the 3.6 fb^{-1} analysis, we parameterize the dependence of the upper side of the uncertainty of the JES on energy E of the jet, in four bins in η, as in Ref. [15]. This parameterization is applied to scale up jet energies and to provide an alternative calibration. A single constant offset is added to the parameterization across all four η bins, such that the average correction applied to the energies of all the jets in the sample is zero to avoid double-counting of acceptance effects. We find an effect of $+0.13$ GeV on m_t.

 (ii) We also apply the downward changes, and find an effect of -0.08 GeV on m_t.

(iii) We apply the positive JES changes directly, i.e., the momentum of each jet is increased by its 1 SD uncertainty, without any parametrization. In contrast to (i) and (ii), the jet energies are not rescaled on average, and the method is expected to account for the change in the overall JES through the k_{JES} parameter in the two-dimensional likelihood fit, at the cost of some double-counting of acceptance effects. We find a change in m_t of -0.20 GeV with this procedure, while k_{JES} changes by -0.018, as expected.

(iv) The energies of jets are increased using a linear parameterization, which is unity for $E = 0$ GeV and increases linearly with E, such that it tangentially approaches the upper limit of uncertainty of the JES. The linear parameterization is obtained separately for each data-taking epoch, and changes slightly due to changes in the JES uncertainty. No overall rescaling of the jet energies is applied. We find -0.21 GeV with this approach for the impact on m_t.

As only one dependence of the true JES on E and η of the jet is realized within the uncertainty corridor, we take the maximum envelope of the above uncertainties of 0.21 GeV and assign it as the systematic uncertainty due to the residual JES correction. In previous analyses [14,48], only approach (i) was used, which corresponds to an uncertainty of 0.13 GeV using our results.

2. Flavor-dependent response to jets

The standard JES calibration used in this measurement contains a flavor-dependent jet response correction, which is responsible for bringing the simulation of calorimeter response to jets into agreement with that observed in data for a given jet flavor [15]. The flavor-dependent correction is given by

$$F_{\text{corr}} = \frac{1}{\langle F \rangle_{\gamma+\text{jet}}} \cdot \frac{\sum_i E_i \cdot R_i^{\text{data}}}{\sum_i E_i \cdot R_i^{\text{MC}}}, \qquad (39)$$

where the index i runs over all constituent particles that belong to a particle jet, and R_i is the detector response to particle i, given differentially in p_T and η of that particle. The factor $\langle F \rangle_{\gamma+\text{jet}}$ ensures that the flavor-averaged part of the JES calibration, extracted from exclusive γ + jet events, is preserved. The correction F_{corr} is largest for b-quark jets and gluon jets, and is relatively small for light quark jets, compared to the flavor-averaged JES, as shown in Fig. 34 of Ref. [15]. We are in a position to apply such a correction in a straightforward way, since the JES is corrected to particle level both for data and MC. To propagate the effect of the uncertainty on F_{corr} to our measured m_t value, we change F_{corr} by ± 1 SD for each data-taking epoch and final state. We apply this factor to the jets in our signal MC samples to get alternative calibrations, resulting in a systematic uncertainty of ∓ 0.16 GeV after symmetrization. This uncertainty accounts for the difference in detector response to different jet flavors, in particular b-quark jets versus light quark jets.

We perform additional studies beyond those done in Ref. [15] to verify that F_{corr} is correctly estimated:

(i) The derivation of F_{corr} requires *a priori* input for the relative contributions of b quark, gluon, and light quark jets to the samples of γ + jets and dijet events that are used for its derivation. A variation on the assumption of these relative contributions would result in somewhat different fitted R_i^{data} in Eq. (39). The relative contributions from different jet flavors

to the sample are taken from PYTHIA with D0 tune A. To estimate the effect of this assumption, we exploit the fact that γ + jets and dijet samples show a rather different sample composition in terms of jet flavor, and obtain F_{corr} in those two samples independently, rather than simultaneously in the standard procedure. We find that the results for F_{corr} in γ + jets and dijet events are consistent with each other within assigned uncertainties.

(ii) Similarly, *a priori* input about the particle composition of the jet is needed for the derivation of F_{corr}, which is also taken from PYTHIA with D0 tune A. A variation of the composition of the jet would result in a change to the numerator and the denominator of Eq. (39) because the sum in i runs over all the particles in the jet, and to R_i^{data}, which are determined from a fit to data in γ + jets and dijet events. To estimate an upper limit on the impact of the particle composition on F_{corr} for b-quark jets, for which F_{corr} is largest, we use simulated $t\bar{t}$ events to study the ratio

$$Q_{\text{corr}}^b = \frac{F_{\text{corr,ALPGEN+HERWIG}}^b}{F_{\text{corr,ALPGEN+PYTHIA}}^b}, \qquad (40)$$

where $F_{\text{corr,ALPGEN+PYTHIA}}^b$ is the default correction from Ref. [15], and $F_{\text{corr,ALPGEN+HERWIG}}^b$ takes the particle composition of the jet predicted by ALPGEN + HERWIG as input, but uses the same R_i^{data} and R_i^{MC} as in the default case. The ratio Q_{corr}^b is shown for ℓ + jets final states in Fig. 32. The excursion of the
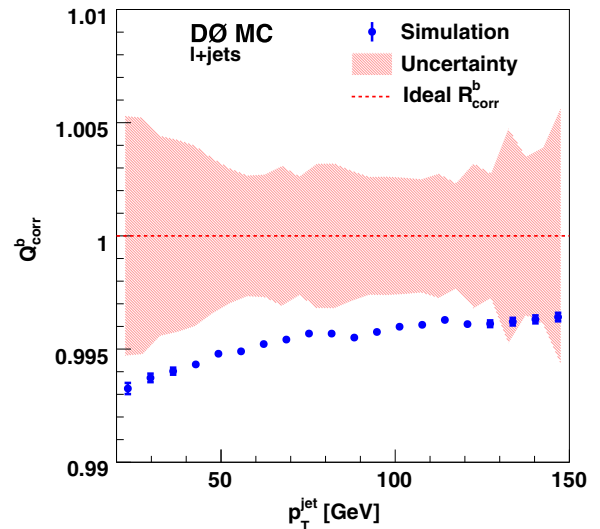
FIG. 32 (color online). The ratio $Q_{\text{corr}}^b = F_{\text{corr,ALPGEN+HERWIG}}^b / F_{\text{corr,ALPGEN+PYTHIA}}^b$ for b-quark jets in simulated $t\bar{t}$ events and ℓ + jets final state as a function of the p_T of the jet. The ideal Q_{corr}^b of unity is indicated as the broken line. The uncertainties on the points reflect the finite size of the MC sample. The total uncertainty on the standard flavor-dependent correction for ALPGEN + PYTHIA is indicated as the band around unity.

ratio from unity is within 0.5% for the p_T spectrum of b-quark jets in $t\bar{t}$ events.

The ratio Q_{corr}^b can only provide an upper limit on the impact of the assumption of the particle composition of the jet on the flavor-dependent calorimeter response, as it does not involve a coherent JES calibration using $\gamma + \text{jet}$ and dijet events. In particular, R_i^{data}, which are determined with PYTHIA, are unchanged, while a calibration of the single particle responses using HERWIG would bring $F_{\text{corr,ALPGEN+HERWIG}}^b$ into better agreement with $\gamma + \text{jet}$ and dijet data, which $F_{\text{corr,ALPGEN+PYTHIA}}^b$ is also tuned to, resulting in a Q_{corr}^b that is closer to unity. Given these findings, we conclude that the uncertainty on m_t from flavor dependence of the calorimeter response to jets of ∓ 0.16 GeV covers the effect from different parton shower and hadronisation models in PYTHIA and HERWIG. Taking our upper limit estimate using Eq. (40) at face value would increase the systematic uncertainty on m_t from flavor dependence of the calorimeter response to jets to ∓ 0.24 GeV, and the total uncertainty of the measurement to 0.78 GeV.

(iii) We perform another cross check of the energy scale for b-quark jets using a similar approach to Ref. [73], by studying the ratio of transverse momenta of b-tagged jets to jets without a b tag. For events with ≥ 2 b-tagged jets, this ratio is defined as

$$R_{bq} = \frac{p_T^{b_1} + p_T^{b_2}}{p_T^{q_1} + p_T^{q_2}}, \quad (41)$$

where b_i refers to the b-tagged jets with the highest p_T, and similarly q_i for the other two jets. In events with one b-tagged jet, the ratio

$$R_{bq} = \frac{2p_T^b}{p_T^{q_1} + p_T^{q_2}} \quad (42)$$

is computed. The distribution of R_{bq} after all selections is shown in Fig. 33 for $m_t = 175$ GeV and $\sigma_{t\bar{t}} = 7.7$ pb, as provided by the ME technique. Good agreement between data and simulations is observed. We extract the overall b quark JES k_{bJES} by performing a template fit to the distribution in R_{bq}, and obtain

$$k_{\text{bJES}} = 1.008 \pm 0.0195(\text{stat})^{+0.037}_{-0.031}(\text{syst}). \quad (43)$$

The systematic uncertainties include dominant sources like JES, jet energy resolution, jet identification, flavor dependence of the detector response, and b tagging, which provides the main contribution. The measured k_{bJES} value is consistent with unity, and underlines the correctness of F_{corr} from Eq. (39).
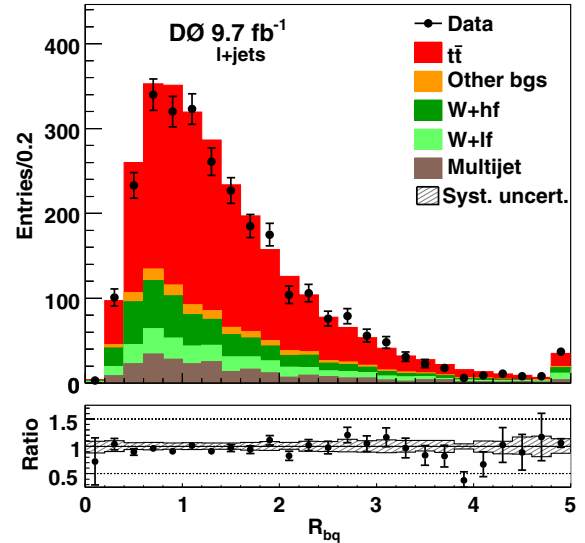
FIG. 33 (color online). The ratio $R_{bq} = (p_T^{b_1} + p_T^{b_2})/(p_T^{j_1} + p_T^{j_2})$ for events with ≥ 2 b-tagged jets, and $R_{bq} = 2p_T^b/(p_T^{j_1} + p_T^{j_2})$ for events with one b-tagged jet, after all selections. The category "Other bgs" encompasses $Z + \text{jets}$, WW, WZ, ZZ, and single top quark production, as well as dileptonic $t\bar{t}$ decays. The production of a W boson in association with at least one b or c quark is denoted as "$W + \text{hf}$", while "$W + \text{lf}$" stands for all other flavor configurations. The last bin includes overflow events. The ratio shows the number of observed events divided by the number of expected events in a given bin. The band of systematic uncertainty is indicated as a shaded area in the ratio plots, and includes dominant sources: JES, jet energy resolution, jet identification, flavor dependence of the detector response, and b tagging.

3. Tagging of b jets

Discrepancies in the b tagging efficiency between data and MC simulations can lead to a systematic shift in the extracted m_t. To evaluate the effect of possible discrepancies, the standard corrections to b tagging rates of u, d, s quark jets and gluons, c quark jets, and b-quark jets, which depend on η and p_T, are changed within their uncertainties. We evaluate the uncertainty from those corrections by simultaneously decreasing the b tagging efficiencies for b and c quark jets within their uncertainties, while increasing the efficiencies for jets from all other quarks, and find ∓ 0.10 GeV after symmetrizing their impact on m_t.

4. Trigger

To evaluate the impact of the trigger on our analysis, we apply trigger weights that simulate the impact of the lepton plus jet trigger differentially in p_T, η, and ϕ of the lepton. An alternative calibration with those trigger weights applied is obtained, resulting in a change in the extracted m_t of ± 0.01 GeV.

5. Lepton momentum scale

The momentum scale of electrons and muons is known with some finite precision. To evaluate the impact of this

effect, we change the momentum scale of a given lepton flavor, while keeping the momentum scale of the other flavor constant, and combine in quadrature the effects found for the two flavors. To evaluate the impact for a given lepton flavor, we assume the worst case, where the momentum scale is shifted in the same direction for all data-taking epochs. We perform this for the up and down changes, and find an effect that is consistent with zero within uncertainties for electrons, and corresponding to 0.01 GeV for muons. Combining the two values in quadrature yields 0.01 GeV, which we quote for this source of systematic uncertainty.

6. Jet energy resolution

An additional smearing of jet energies is applied to all MC samples as part of the JES calibration in order to achieve better agreement of MC simulations and data [15]. To evaluate the possible effect of disagreement between data and MC simulations in jet energy resolutions on m_t, we produce simulated MC samples where the jet energy resolution correction is changed up and down by its uncertainty. Event probabilities are then re-calculated and ensemble tests are repeated. We find an effect of ± 0.07 GeV on m_t from jet energy resolution, after symmetrizing the excursions.

7. Jet identification efficiency

The efficiency for the identification of jets is slightly higher in MC simulation than in data, and is therefore corrected as part of the JES calibration [15] to achieve better agreement between MC simulations and data in jet identification efficiencies. To evaluate the potential impact from this source on m_t, the jet identification efficiencies in the signal MC sample are decreased according to their uncertainties. Subsequently, event probabilities are recalculated and ensemble tests are repeated. The extracted value of m_t using this alternative calibration differs from the central value by -0.01 GeV, which is quoted as systematic uncertainty.

C. Method

1. Modeling of multijet events

Since we require four jets, and at least one of them b-tagged, the contribution of the MJ background to our sample of $t\bar{t}$ candidate events is small (cf. Table II). Nonetheless, we explicitly account for the next-to-dominant contribution from this background when constructing the PEs for the calibration of the ME technique, as described in Secs. VI A and VII A. This was not done in the previous measurement using 3.6 fb^{-1} of integrated luminosity [14]. To evaluate a systematic uncertainty from the modeling of MJ background, we do not include it in the ensemble tests for an alternative calibration in m_t, which yields a change in m_t of $+0.04$ GeV.

2. Signal fraction

We apply the f values measured in each data-taking epoch and final state, as summarized in Table IV, to construct the PEs used for calibrating the response of the ME technique in m_t and k_{JES}. To evaluate the systematic uncertainty from f, we use alternative calibrations in m_t and k_{JES}, where f is changed by $\pm 5\%$, simultaneously for all data-taking epochs and final states. The 5% value is motivated by the magnitude of the systematic uncertainty on the measured $t\bar{t}$ production cross section in the D0 data [61], ignoring the uncertainty from integrated luminosity. We obtain ± 0.08 GeV as an effect from this source of systematic uncertainty.

3. MC calibration

The statistical uncertainties due to the limited size of MC samples that are used to construct PEs to study the response of the ME technique, as discussed in Secs. VI A and VII A, contribute an uncertainty on the final calibrated value of m_t that is statistical in nature. To determine this contribution, we note the uncertainties on the offset and slope parameters of the linear calibrations in Figs. 11 and 12, and propagate them, assuming Gaussian uncorrelated uncertainties, to the extracted m_t values in each of the data-taking epochs and final states. Combining the individual m_t results for the up and down changes and symmetrizing, we find an uncertainty of ± 0.07 GeV due to the limited size of MC samples.

D. Summary of uncertainties

Quadratically combining contributions from all sources of systematic uncertainties from Table V, we obtain a total systematic uncertainty of 0.49 GeV. The total uncertainty of the measurement of 0.76 GeV is obtained by combining the total systematic uncertainty and the statistical uncertainty of 0.58 GeV. The statistical uncertainty consists of two parts: 0.41 GeV from m_t alone and 0.41 GeV from k_{JES}. Considering the latter as a source of systematic uncertainty, as is done for the Tevatron combination [8], the total systematic uncertainty including the statistical contribution from the *in situ* constraint on the JES is 0.64 GeV.

IX. COMPARISON WITH PREVIOUS MEASUREMENTS

A. Comparison with the Tevatron average

Our result is included in the Tevatron combination from July 2014 [8], which takes into account ten published and two preliminary results from the CDF and D0 Collaborations using $p\bar{p}$ collision data from Run I and Run II of the Fermilab Tevatron Collider. Considering correlations between sources of systematic uncertainty as described in detail in Ref. [7], the final result is $m_t = 174.34 \pm 0.64$ GeV, with a relative weight of 67% from the D0 measurement. An overview of the input
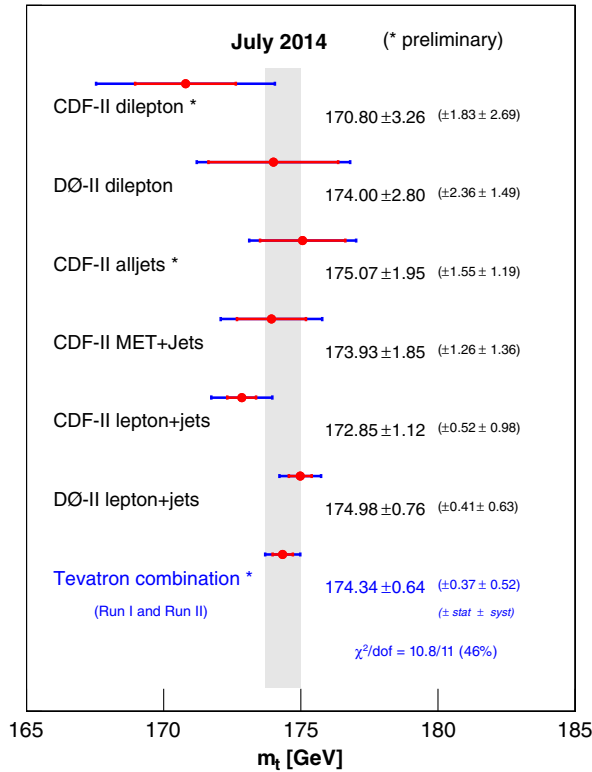
FIG. 34 (color online). Summary of the measurements performed in Run II of the Tevatron which are used as inputs to the Tevatron combination [8]. The inner error bars indicate the statistical uncertainties, while the outer bars represent the total uncertainties. The Tevatron average value of m_t obtained using input measurements from Run I and Run II is given at the bottom and its uncertainty is shown by the band. The Figure is adapted from Ref. [8].

measurements performed using Run II data is presented in Fig. 34. All measurements from Run I and Run II are consistent with $\chi^2 = 10.8$ for 11 degrees of freedom, which corresponds to a χ^2 probability of 46%.

B. Comparison with the world average

Our result can be compared with the current world average of $m_t = 173.34 \pm 0.76$ GeV [9], which encompasses 11 measurements from the ATLAS, CDF, CMS, and D0 Collaborations, excluding this measurement. We do this comparison considering the full uncertainty in the world combination and only the statistical uncertainty in our measurement, which provides a reasonable approximation, given the large correlation among the experiments for most sources of systematic uncertainty. Furthermore, we use the simplifying assumption that there is no correlation between the statistical uncertainty of our new measurement and of the world average. We find consistency at the 1.7 SD level. Due to the complicated correlation of systematic uncertainties, a more detailed comparison should be performed in a separate document, with participation from all the collaborations supplying measured m_t values as inputs, and include all updates since the publication of Ref. [9].

X. SUMMARY

In summary, we have performed a measurement of the mass of the top quark using the matrix element technique in $t\bar{t}$ candidate events in lepton + jets final states using 9.7 fb^{-1} of Run II integrated luminosity collected by the D0 detector at the Fermilab Tevatron $p\bar{p}$ Collider. The result,

$$m_t = 174.98 \pm 0.58 \; (\text{stat} + \text{JES}) \pm 0.49 (\text{syst}) \text{ GeV, or}$$

$$m_t = 174.98 \pm 0.76 \text{ GeV},$$

is consistent with the values given by the current Tevatron and world combinations of the top-quark mass [8,9] and achieves by itself a similar precision. With an uncertainty of 0.43%, it constitutes the most precise single measurement of the top-quark mass, and is $\approx$70% more precise than the next-to-most precise single measurement [74]. The total systematic uncertainty of our result is smaller than that of any other single measurement.

APPENDIX A: CONSTRAINING THE AMOUNT OF RADIATION USING DRELL-YAN EVENTS

Because of the limited statistics in $t\bar{t}$ candidate events recorded by D0 in Run II, it is difficult to use $t\bar{t}$ events directly to study ISR and FSR. We therefore take an alternative approach using the $Z/\gamma^* \to \ell^+\ell^-$ process to experimentally constrain ISR and FSR. In the following, we motivate this approach, briefly review the measurement of $Z/\gamma^* \to \ell^+\ell^-$ production [65] that we use to obtain the dependence of ISR and FSR, and present our results.

1. Motivation

At the Tevatron, $t\bar{t}$ pairs are dominantly produced via $q\bar{q}$ annihilation. The ISR will stem therefore dominantly from the process where an initial-state quark radiates a gluon, which can be described by the $P_{q\to qg}$ splitting function. In the LO picture of the $t\bar{t}$ process, the final-state partons are also quarks, and FSR is therefore described by the same $P_{q\to qg}$ splitting function. At the same time, the production of Z bosons at the Tevatron is also dominated by $q\bar{q}$ annihilation, and ISR in $Z/\gamma^* \to \ell^+\ell^-$ can be also described by the $P_{q\to qg}$ splitting function. A measurement of ISR in $Z/\gamma^* \to \ell^+\ell^-$ events can therefore be used to constrain ISR and FSR in $t\bar{t}$ events.

The experimental approach outlined above was first proposed in Ref. [75]. Beyond Ref. [75], we use the ϕ^* variable [65], which is more sensitive to soft ISR. Since this measurement is corrected for detector effects, it can be used to compare directly generated $Z/\gamma^* \to \ell^+\ell^-$ events with data.

2. The measurement of the $Z/\gamma^* \to \ell^+\ell^-$ cross section

The ϕ^* observable used to establish sensitivity to ISR in Ref. [65] is defined as

$$\phi^* = \tan\left(\phi_{\text{acop}}/2\right)\sin(\theta_\eta^*), \qquad \text{(A1)}$$

where ϕ_{acop} is the acoplanarity angle, given by $\phi_{\text{acop}} = \pi - \Delta\phi^{\ell^+\ell^-}$, and $\Delta\phi^{\ell^+\ell^-}$ is the difference in azimuthal angle between the two lepton candidates. The variable θ_η^* is a measure of the scattering angle of the leptons relative to the proton beam direction in the rest frame of the dilepton system, and is defined as

$$\cos(\theta_\eta^*) = \tanh\left(\frac{\eta^- - \eta^+}{2}\right), \qquad \text{(A2)}$$

where η^- and η^+ are the laboratory pseudorapidities of the negatively and positively charged lepton, respectively.

The measurement of $d\sigma_{Z/\gamma^*\to\ell^+\ell^-}/d\phi^*$ is corrected for detector effects, and performed in the fiducial region defined by the presence of the two oppositely charged

TABLE VI. Summary of kinematic requirements used to define the measurement of $d\sigma_{Z/\gamma^*\to\ell^+\ell^-}/d\phi^*$ in the fiducial region of Ref. [65].

Charged leptons:	$p_T > 20\,\text{GeV}$	$\|\eta\| < 1.1$ or $1.5 < \|\eta\| < 3.0$ (e)
	$p_T > 15\,\text{GeV}$	$\|\eta\| < 2.0$ (μ)
$\ell^+\ell^-$ system:	$60\,\text{GeV} < m_{\ell^+\ell^-} < 120\,\text{GeV}$	

leptons, as summarized in Table VI. The electron four-momentum is defined as the sum of the four-momenta of all electrons and photons in the $\Delta R < 0.2$ cone around the detector-level electron. No cone summation is applied to muons. The measurement is performed in three bins of rapidity of the boson of $0 < |y| < 1$, $1 < |y| < 2$, and $|y| > 2$ in e^+e^-, and in two bins of rapidity, $0 < |y| < 1$ and $1 < |y| < 2$ in $\mu^+\mu^-$ final states. This ensures that $P_{q\to qg}$ is probed in different kinematic regimes of the square of the four-momentum transfer Q^2.

3. Results

As described in Sec. III, ALPGEN+PYTHIA is used to generate $t\bar{t}$ MC events, where Feynman diagrams accounting for hard radiation from the initial or final state partons up to second-order in α_s are introduced through the hard ME in ALPGEN, i.e., in bins of 0, 1, and 2 additional light partons, which are then combined according to their cross sections. For consistency, we use an identical setup for generating $Z \to \ell^+\ell^-$ events. The ratio of unfolded $d\sigma_{Z/\gamma^*\to\ell^+\ell^-}/d\phi^*$ data to the predictions from ALPGEN+PYTHIA at particle level, is shown in Fig. 35 for the e^+e^- and in Fig. 36 for the $\mu^+\mu^-$ final states. The ALPGEN+PYTHIA model is not able to describe the data over the entire spectrum in ϕ^*, but the overall agreement is reasonable. In the analysis, we identify up and down changes in the radiation rate that cover the excursions of nominal MC predictions from the data.

Modifying parameters such as Λ_{QCD} or α_s adjusting the rate of ISR/FSR in the PS, as is done in stand-alone PYTHIA, leads to unphysical results for ALPGEN+PYTHIA, since the MLM matching of the PS to the hard ME calculation partly compensates for such effects in the PS [64]. Thus, the preferred approach is to change the amount of ISR/FSR through rescaling of the renormalization scale in the CKKW scale-setting procedure `ktfac` from its default of unity, as suggested in Ref. [64]. Our studies indicate that changing the `ktfac` parameter by a factor of ± 1.5 provide coverage for the excursions of the nominal MC predictions from the data. This is demonstrated in Fig. 35 for the e^+e^- and in Fig. 36 for the $\mu^+\mu^-$ final states. Based on these studies, we evaluate the systematic uncertainty from ISR/FSR in $t\bar{t}$ events by setting the `ktfac` parameter to 2/3 for the up and 3/2 for the down point.
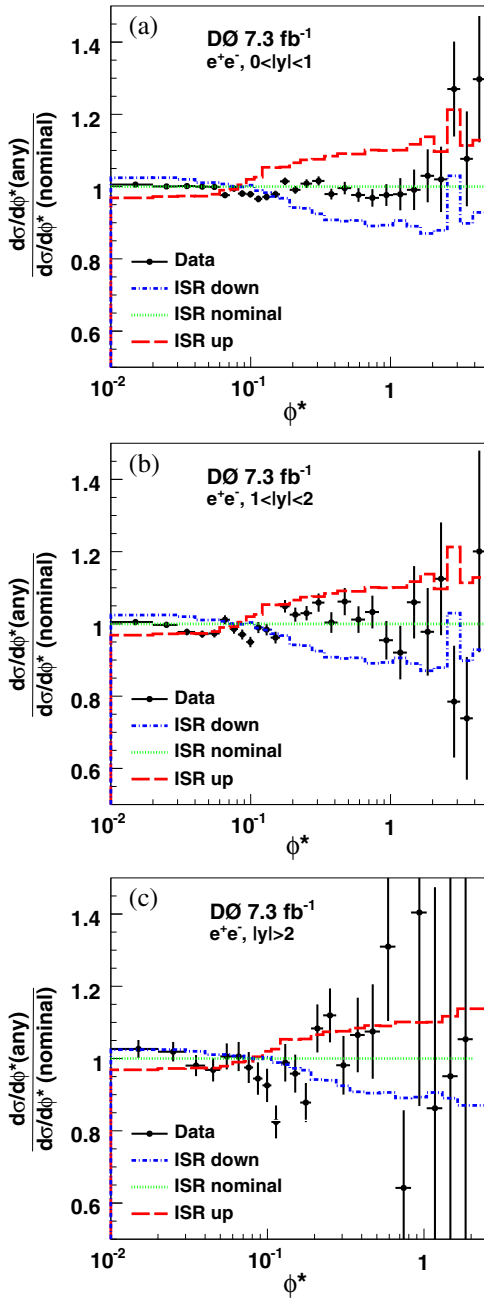
FIG. 35 (color online). (a) Ratio of the unfolded differential cross section $d\sigma_{Z/\gamma^* \to e^+ e^-}/d\phi^*$ and the nominal predictions from ALPGEN+PYTHIA for $0 < |y| < 1$, where the error bars represent the total uncertainties in the data. The ratios of predictions determined with ALPGEN+PYTHIA where the amount of radiation is changed up and down relative the nominal predictions from ALPGEN+PYTHIA are shown, respectively, as red broken and blue dash-dotted lines. The statistical uncertainties from the finite number of simulated MC events are negligible compared to the uncertainties in the data. (b) Same as (a), but for $1 < |y| < 2$. (c) Same as (a), but for $|y| > 2$.
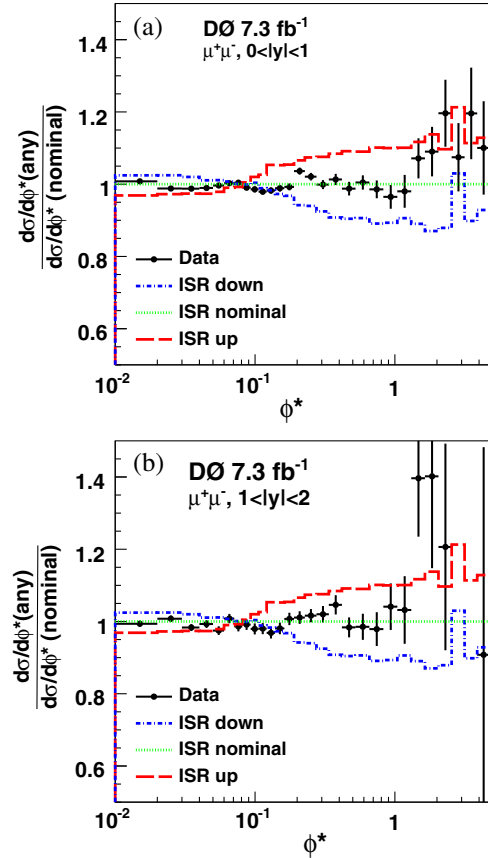
FIG. 36 (color online). (a) Ratio of the unfolded differential cross section $d\sigma_{Z/\gamma^* \to \mu^+ \mu^-}/d\phi^*$ and the nominal predictions from ALPGEN+PYTHIA for $0 < |y| < 1$, where the error bars represent the total uncertainties in the data. The ratios of predictions obtained with ALPGEN+PYTHIA where the amount of radiation is changed up and down relative the nominal predictions from ALPGEN+PYTHIA are shown, respectively, as red broken and blue dash-dotted lines. The statistical uncertainties from the finite number of simulated MC events are negligible compared to the uncertainties in the data. (b) Same as (a), but for $1 < |y| < 2$.

APPENDIX B: TRANSFER FUNCTION PARAMETERS

In Tables VII–XXII of this appendix we summarize the jet transfer function parameters a_i and b_i defined in Eq. (15) as a function of data-taking epoch, jet flavor, and pseudorapidity bin. Jet flavor is denoted as "light jets" for u, d, c, s quark jets, "b_μ jets" for b-quark jets with a soft muon tag, and "b jets" for all other b-quark jets. The parameter a_3 is fixed to 0 in order to improve the convergence of the double-Gaussian fit function. The parameter values are given in units of GeV (a_1), 1 (b_1), GeV (a_2), 1 (b_2), 1 (a_3), GeV^{-1} (b_3), GeV (a_4), 1 (b_4), GeV (a_5), and 1 (b_5).

TABLE VII.   Jet TF parameters a_i and b_i for Run IIa and $|\eta| \leq 0.4$.

	Light jets		b jets		b_μ jets	
i	a_i	b_i	a_i	b_i	a_i	b_i
1	$-1.29 \times 10^{+0}$	2.21×10^{-2}	$2.92 \times 10^{+0}$	-1.91×10^{-1}	$6.06 \times 10^{+0}$	-1.40×10^{-1}
2	$4.04 \times 10^{+0}$	1.09×10^{-1}	$2.77 \times 10^{+0}$	2.07×10^{-1}	$1.67 \times 10^{+0}$	1.65×10^{-1}
3	0	2.35×10^{-4}	0	4.09×10^{-2}	0	8.68×10^{-5}
4	$2.37 \times 10^{+1}$	-1.70×10^{-1}	$-9.96 \times 10^{+0}$	4.68×10^{-2}	$4.60 \times 10^{+1}$	-4.15×10^{-1}
5	$1.89 \times 10^{+1}$	9.64×10^{-2}	$3.82 \times 10^{+0}$	9.23×10^{-2}	$1.83 \times 10^{+1}$	1.44×10^{-1}

TABLE VIII.   Jet TF parameters a_i and b_i for Run IIa and $0.4 < |\eta| \leq 0.8$.

	Light jets		b jets		b_μ jets	
i	a_i	b_i	a_i	b_i	a_i	b_i
1	-6.87×10^{-1}	8.60×10^{-4}	$4.34 \times 10^{+0}$	-2.11×10^{-1}	$6.88 \times 10^{+0}$	-1.56×10^{-1}
2	$3.64 \times 10^{+0}$	1.19×10^{-1}	$3.13 \times 10^{+0}$	2.03×10^{-1}	$1.71 \times 10^{+0}$	1.65×10^{-1}
3	0	2.73×10^{-4}	0	3.40×10^{-2}	0	9.12×10^{-5}
4	$2.48 \times 10^{+1}$	-1.73×10^{-1}	$-8.77 \times 10^{+0}$	2.43×10^{-2}	$4.71 \times 10^{+1}$	-3.41×10^{-1}
5	$1.89 \times 10^{+1}$	9.84×10^{-2}	$3.45 \times 10^{+0}$	9.94×10^{-2}	$2.09 \times 10^{+1}$	1.07×10^{-1}

TABLE IX.   Jet TF parameters a_i and b_i for Run IIa and $0.8 < |\eta| \leq 1.6$.

	Light jets		b jets		b_μ jets	
i	a_i	b_i	a_i	b_i	a_i	b_i
1	$4.53 \times 10^{+0}$	-7.58×10^{-2}	$1.29 \times 10^{+1}$	-1.58×10^{-1}	$6.00 \times 10^{+0}$	-1.08×10^{-1}
2	$3.32 \times 10^{+0}$	1.55×10^{-1}	$5.24 \times 10^{+0}$	2.40×10^{-1}	$6.04 \times 10^{+0}$	1.30×10^{-1}
3	0	4.28×10^{-3}	0	1.76×10^{-1}	0	1.00×10^{-3}
4	$9.02 \times 10^{+0}$	7.90×10^{-2}	$-5.98 \times 10^{+0}$	-6.28×10^{-2}	$6.00 \times 10^{+1}$	-7.50×10^{-1}
5	$1.30 \times 10^{+1}$	8.39×10^{-2}	$1.63 \times 10^{+0}$	1.82×10^{-1}	$1.00 \times 10^{+1}$	2.00×10^{-1}

TABLE X.   Jet TF parameters a_i and b_i for Run IIa and $1.6 < |\eta| \leq 2.5$.

	Light jets		b jets		b_μ jets	
i	a_i	b_i	a_i	b_i	a_i	b_i
1	$1.62 \times 10^{+1}$	-2.28×10^{-1}	$1.07 \times 10^{+1}$	-3.07×10^{-1}	$3.28 \times 10^{+1}$	-4.28×10^{-1}
2	$2.78 \times 10^{+0}$	1.46×10^{-1}	$3.61 \times 10^{+0}$	1.23×10^{-1}	$8.34 \times 10^{+0}$	7.76×10^{-2}
3	0	6.15×10^{-3}	0	6.98×10^{-3}	0	7.06×10^{-3}
4	$1.86 \times 10^{+1}$	-1.30×10^{-3}	$5.35 \times 10^{+0}$	-4.33×10^{-2}	$2.07 \times 10^{+1}$	-1.31×10^{-1}
5	$1.47 \times 10^{+1}$	8.60×10^{-2}	$1.38 \times 10^{+1}$	9.66×10^{-2}	$1.18 \times 10^{+1}$	1.08×10^{-1}

TABLE XI.   Jet TF parameters a_i and b_i for Run IIb1 and $|\eta| \leq 0.4$.

	Light jets		b jets		b_μ jets	
i	a_i	b_i	a_i	b_i	a_i	b_i
1	$-2.17 \times 10^{+0}$	2.39×10^{-2}	8.74×10^{-1}	-1.86×10^{-1}	$5.26 \times 10^{+0}$	-1.29×10^{-1}
2	$4.08 \times 10^{+0}$	6.66×10^{-2}	$2.67 \times 10^{+0}$	1.82×10^{-1}	$1.45 \times 10^{+0}$	1.51×10^{-1}
3	0	2.77×10^{-4}	0	4.41×10^{-2}	0	2.13×10^{-4}
4	$1.27 \times 10^{+1}$	-1.76×10^{-1}	$-8.38 \times 10^{+0}$	4.36×10^{-2}	$3.78 \times 10^{+1}$	-5.31×10^{-1}
5	$1.46 \times 10^{+1}$	1.73×10^{-1}	$4.01 \times 10^{+0}$	5.24×10^{-2}	$1.85 \times 10^{+1}$	1.06×10^{-1}

TABLE XII.   Jet TF parameters a_i and b_i for Run IIb1 and $0.4 < |\eta| \leq 0.8$.

	Light jets		b jets		b_μ jets	
i	a_i	b_i	a_i	b_i	a_i	b_i
1	$-1.65 \times 10^{+0}$	9.52×10^{-3}	$2.67 \times 10^{+0}$	-2.07×10^{-1}	$5.00 \times 10^{+0}$	-1.15×10^{-1}
2	$3.79 \times 10^{+0}$	7.95×10^{-2}	$2.79 \times 10^{+0}$	1.82×10^{-1}	$1.33 \times 10^{+0}$	1.46×10^{-1}
3	0	2.71×10^{-4}	0	3.65×10^{-2}	0	4.99×10^{-4}
4	$1.61 \times 10^{+1}$	-2.06×10^{-1}	$-7.79 \times 10^{+0}$	3.40×10^{-2}	$4.00 \times 10^{+1}$	-8.00×10^{-1}
5	$1.47 \times 10^{+1}$	1.72×10^{-1}	$3.42 \times 10^{+0}$	6.41×10^{-2}	0	4.00×10^{-1}

TABLE XIII.   Jet TF parameters a_i and b_i for Run IIb1 and $0.8 < |\eta| \leq 1.6$.

	Light jets		b jets		b_μ jets	
i	a_i	b_i	a_i	b_i	a_i	b_i
1	$6.21 \times 10^{+0}$	-1.65×10^{-1}	$7.16 \times 10^{+0}$	-2.28×10^{-1}	$8.00 \times 10^{+0}$	-1.33×10^{-1}
2	8.73×10^{-1}	1.57×10^{-1}	$4.31 \times 10^{+0}$	1.78×10^{-1}	$6.04 \times 10^{+0}$	1.08×10^{-1}
3	0	1.77×10^{-2}	0	2.11×10^{-2}	0	1.00×10^{-3}
4	$2.57 \times 10^{+0}$	2.67×10^{-2}	$-9.69 \times 10^{+0}$	9.76×10^{-3}	$6.00 \times 10^{+1}$	-7.50×10^{-1}
5	$1.01 \times 10^{+1}$	6.36×10^{-2}	$3.41 \times 10^{+0}$	9.95×10^{-2}	$1.00 \times 10^{+1}$	2.00×10^{-1}

TABLE XIV.   Jet TF parameters a_i and b_i for Run IIb1 and $1.6 < |\eta| \leq 2.5$.

	Light jets		b jets		b_μ jets	
i	a_i	b_i	a_i	b_i	a_i	b_i
1	$5.79 \times 10^{+0}$	-1.07×10^{-1}	$1.69 \times 10^{+0}$	-2.27×10^{-1}	$2.80 \times 10^{+1}$	-3.99×10^{-1}
2	$2.98 \times 10^{+0}$	1.40×10^{-1}	$3.09 \times 10^{+0}$	1.27×10^{-1}	$7.99 \times 10^{+0}$	7.81×10^{-2}
3	0	2.61×10^{-3}	0	5.69×10^{-3}	0	7.00×10^{-3}
4	$9.11 \times 10^{+0}$	4.16×10^{-2}	$-1.08 \times 10^{+1}$	2.90×10^{-2}	$9.46 \times 10^{+0}$	-9.70×10^{-2}
5	$1.72 \times 10^{+1}$	5.85×10^{-2}	$1.33 \times 10^{+1}$	8.71×10^{-2}	$8.78 \times 10^{+0}$	1.13×10^{-1}

TABLE XV.   Jet TF parameters a_i and b_i for Run IIb2 and $|\eta| \leq 0.4$.

	Light jets		b jets		b_μ jets	
i	a_i	b_i	a_i	b_i	a_i	b_i
1	$-2.19 \times 10^{+0}$	2.49×10^{-2}	$1.22 \times 10^{+0}$	-1.92×10^{-1}	$1.60 \times 10^{+0}$	-4.93×10^{-2}
2	$4.23 \times 10^{+0}$	6.91×10^{-2}	$2.55 \times 10^{+0}$	1.87×10^{-1}	$3.66 \times 10^{+0}$	8.15×10^{-2}
3	0	2.63×10^{-4}	0	4.37×10^{-2}	0	7.81×10^{-3}
4	$1.41 \times 10^{+1}$	-1.81×10^{-1}	$-8.57 \times 10^{+0}$	3.83×10^{-2}	$7.48 \times 10^{+0}$	-1.91×10^{-1}
5	$1.48 \times 10^{+1}$	1.80×10^{-1}	$3.85 \times 10^{+0}$	5.67×10^{-2}	$4.56 \times 10^{+0}$	1.59×10^{-1}

TABLE XVI.   Jet TF parameters a_i and b_i for Run IIb2 and $0.4 < |\eta| \leq 0.8$.

	Light jets		b jets		b_μ jets	
i	a_i	b_i	a_i	b_i	a_i	b_i
1	$-1.68 \times 10^{+0}$	1.37×10^{-2}	$2.19 \times 10^{+0}$	-2.02×10^{-1}	$6.00 \times 10^{+0}$	-1.46×10^{-1}
2	$4.12 \times 10^{+0}$	7.83×10^{-2}	$2.53 \times 10^{+0}$	1.86×10^{-1}	$1.38 \times 10^{+0}$	1.60×10^{-1}
3	0	2.80×10^{-4}	0	3.43×10^{-2}	0	1.50×10^{-4}
4	$1.68 \times 10^{+1}$	-2.16×10^{-1}	$-8.54 \times 10^{+0}$	3.46×10^{-2}	$3.75 \times 10^{+1}$	-3.59×10^{-1}
5	$1.56 \times 10^{+1}$	1.66×10^{-1}	$3.59 \times 10^{+0}$	6.47×10^{-2}	$1.59 \times 10^{+1}$	1.87×10^{-1}

TABLE XVII.   Jet TF parameters a_i and b_i for Run IIb2 and $0.8 < |\eta| \leq 1.6$.

| | Light jets | | b jets | | b_μ jets | |
i	a_i	b_i	a_i	b_i	a_i	b_i
1	$2.20 \times 10^{+0}$	-2.52×10^{-2}	$6.75 \times 10^{+0}$	-2.27×10^{-1}	$8.00 \times 10^{+0}$	-1.39×10^{-1}
2	$5.77 \times 10^{+0}$	1.07×10^{-1}	$4.14 \times 10^{+0}$	1.78×10^{-1}	$5.54 \times 10^{+0}$	1.28×10^{-1}
3	0	3.57×10^{-4}	0	1.93×10^{-2}	0	1.43×10^{-4}
4	$2.16 \times 10^{+1}$	-1.23×10^{-1}	$-1.09 \times 10^{+1}$	1.23×10^{-2}	$-4.00 \times 10^{+1}$	-2.22×10^{-1}
5	$1.91 \times 10^{+1}$	1.19×10^{-1}	$3.25 \times 10^{+0}$	1.03×10^{-1}	$4.10 \times 10^{+1}$	2.87×10^{-1}

TABLE XVIII.   Jet TF parameters a_i and b_i for Run IIb2 and $1.6 < |\eta| \leq 2.5$.

| | Light jets | | b jets | | b_μ jets | |
i	a_i	b_i	a_i	b_i	a_i	b_i
1	$7.33 \times 10^{+0}$	-1.41×10^{-1}	$2.55 \times 10^{+0}$	-2.48×10^{-1}	$9.25 \times 10^{+0}$	-1.81×10^{-1}
2	$3.16 \times 10^{+0}$	1.35×10^{-1}	$4.56 \times 10^{+0}$	1.13×10^{-1}	$3.35 \times 10^{+0}$	1.53×10^{-1}
3	0	3.51×10^{-3}	0	5.90×10^{-3}	0	1.68×10^{-4}
4	$5.54 \times 10^{+0}$	4.50×10^{-2}	$-1.21 \times 10^{+1}$	2.30×10^{-2}	$2.40 \times 10^{+1}$	2.36×10^{-1}
5	$1.60 \times 10^{+1}$	6.68×10^{-2}	$1.32 \times 10^{+1}$	8.86×10^{-2}	$3.55 \times 10^{+1}$	-1.18×10^{-1}

TABLE XIX.   Jet TF parameters a_i and b_i for Run IIb3 and $|\eta| \leq 0.4$.

| | Light jets | | b jets | | b_μ jets | |
i	a_i	b_i	a_i	b_i	a_i	b_i
1	$-1.87 \times 10^{+0}$	1.94×10^{-2}	$4.64 \times 10^{+0}$	-2.02×10^{-1}	$6.72 \times 10^{+0}$	-1.39×10^{-1}
2	$4.11 \times 10^{+0}$	7.20×10^{-2}	$2.78 \times 10^{+0}$	2.32×10^{-1}	$1.56 \times 10^{+0}$	1.53×10^{-1}
3	0	3.39×10^{-4}	0	7.93×10^{-2}	0	2.60×10^{-4}
4	$1.70 \times 10^{+1}$	-1.47×10^{-1}	$-6.31 \times 10^{+0}$	1.41×10^{-2}	$3.27 \times 10^{+1}$	-3.09×10^{-1}
5	$1.63 \times 10^{+1}$	1.60×10^{-1}	$3.56 \times 10^{+0}$	6.45×10^{-2}	$1.32 \times 10^{+1}$	1.98×10^{-1}

TABLE XX.   Jet TF parameters a_i and b_i for Run IIb3 and $0.4 < |\eta| \leq 0.8$.

| | Light jets | | b jets | | b_μ jets | |
i	a_i	b_i	a_i	b_i	a_i	b_i
1	$-1.70 \times 10^{+0}$	1.67×10^{-2}	$4.22 \times 10^{+0}$	-2.03×10^{-1}	$6.70 \times 10^{+0}$	-1.44×10^{-1}
2	$4.17 \times 10^{+0}$	7.83×10^{-2}	$2.91 \times 10^{+0}$	2.08×10^{-1}	$1.64 \times 10^{+0}$	1.56×10^{-1}
3	0	3.12×10^{-4}	0	4.86×10^{-2}	0	1.98×10^{-4}
4	$1.89 \times 10^{+1}$	-1.77×10^{-1}	$-7.71 \times 10^{+0}$	2.99×10^{-2}	$3.68 \times 10^{+1}$	-2.84×10^{-1}
5	$1.77 \times 10^{+1}$	1.55×10^{-1}	$3.43 \times 10^{+0}$	6.77×10^{-2}	$1.66 \times 10^{+1}$	1.76×10^{-1}

TABLE XXI.   Jet TF parameters a_i and b_i for Run IIb3 and $0.8 < |\eta| \leq 1.6$.

| | Light jets | | b jets | | b_μ jets | |
i	a_i	b_i	a_i	b_i	a_i	b_i
1	$1.56 \times 10^{+0}$	-1.84×10^{-2}	$1.02 \times 10^{+1}$	-2.61×10^{-1}	$8.00 \times 10^{+0}$	-1.33×10^{-1}
2	$5.96 \times 10^{+0}$	1.08×10^{-1}	$4.92 \times 10^{+0}$	1.91×10^{-1}	$6.04 \times 10^{+0}$	1.08×10^{-1}
3	0	3.87×10^{-4}	0	3.34×10^{-2}	0	1.00×10^{-3}
4	$2.12 \times 10^{+1}$	-9.65×10^{-2}	$-9.51 \times 10^{+0}$	-5.50×10^{-3}	$6.00 \times 10^{+1}$	-7.50×10^{-1}
5	$2.06 \times 10^{+1}$	1.08×10^{-1}	$3.00 \times 10^{+0}$	1.16×10^{-1}	$1.00 \times 10^{+1}$	2.00×10^{-1}

TABLE XXII.   Jet TF parameters a_i and b_i for Run IIb3 and $1.6 < |\eta| \leq 2.5$.

	Light jets		b jets		b_μ jets	
i	a_i	b_i	a_i	b_i	a_i	b_i
1	$6.59 \times 10^{+0}$	-1.06×10^{-1}	-3.29×10^{-1}	-1.80×10^{-1}	$2.35 \times 10^{+1}$	-3.25×10^{-1}
2	$2.77 \times 10^{+0}$	1.37×10^{-1}	9.64×10^{-1}	1.47×10^{-1}	$6.73 \times 10^{+0}$	1.00×10^{-1}
3	0	2.01×10^{-3}	0	3.62×10^{-3}	0	3.65×10^{-3}
4	$1.26 \times 10^{+1}$	2.99×10^{-2}	$-6.32 \times 10^{+0}$	1.59×10^{-2}	$9.75 \times 10^{+0}$	-6.83×10^{-2}
5	$1.78 \times 10^{+1}$	5.45×10^{-2}	$1.47 \times 10^{+1}$	7.99×10^{-2}	$1.29 \times 10^{+1}$	9.45×10^{-2}

[1] S. Abachi *et al.* (D0 Collaboration), Phys. Rev. Lett. **74,** 2632 (1995).

[2] F. Abe *et al.* (CDF Collaboration), Phys. Rev. Lett. **74,** 2626 (1995).

[3] The ALEPH, CDF, D0, DELPHI, L3, OPAL, SLC Collaborations, the LEP Electroweak Working Group, the Tevatron Electroweak Working Group, and the SLD electroweak and heavy flavour groups, arXiv:1012.2367.

[4] G. Degrassi, S. Di. Vita, J. E.-M, J. R. Espinosa, G. F. Giudice, G. Isidori, and A. Strumia, J. High Energy Phys. 08 (2012) 098.

[5] F. Bezrukov, and M. Shaposhnikov, Phys. Lett. B **659,** 703 (2008).

[6] A. D. Simone, M. P. Hertzberg, and F. Wilczek, Phys. Lett. B **678,** 1 (2009).

[7] T. Aaltonen *et al.* (CDF and D0 Collaborations), Phys. Rev. D **86,** 092003 (2012).

[8] T. Aaltonen *et al.* (CDF and D0 Collaborations), arXiv:1407.2682, and references therein.

[9] G. Aad *et al.* (ATLAS, CDF, CMS, and D0 Collaborations), arXiv:1403.4427.

[10] In the SM, top quarks decay via $t \rightarrow Wb$ with a branching ratio of 99.9% under the assumption of three quark families [17].

[11] V. M. Abazov *et al.* (D0 Collaboration), Nature (London) **429,** 638 (2004).

[12] T. Aaltonen *et al.* (CDF and D0 Collaborations), Phys. Rev. D **88,** 052018 (2013).

[13] V. M. Abazov *et al.* (D0 Collaboration), Phys. Rev. Lett. **113,** 032002 (2014).

[14] V. M. Abazov *et al.* (D0 Collaboration), Phys. Rev. D **84,** 032004 (2011).

[15] V. M. Abazov *et al.* (D0 Collaboration), Nucl. Instrum. Methods Phys. Res., Sect. A **763,** 442 (2014).

[16] M. L. Mangano, F. Piccinini, A. D. Polosa, M. Moretti, and R. Pittau, J. High Energy Phys. 07 (2003) 001.

[17] K. Olive *et al.* (Particle Data Group), Chin. Phys. C **38,** 090001 (2014).

[18] S. Frixione and B. R. Webber, J. High Energy Phys. 06 (2002), 029.

[19] S. Frixione, P. Nason, and C. Oleari, J. High Energy Phys. 07 (2007) 070.

[20] V. M. Abazov *et al.* (D0 Collaboration), Nucl. Instrum. Methods Phys. Res., Sect A **565,** 463 (2006).

[21] S. Abachi *et al.* (D0 Collaboration), Nucl. Instrum. Methods Phys. Res., Sect. A **338,** 185 (1994).

[22] S. N. Ahmed *et al.*, Nucl. Instrum. Methods Phys. Res., Sect. A **634,** 8 (2011).

[23] The D0 coordinate system is right-handed, with the z axis pointing in the direction of the Tevatron proton beam and the y axis pointing upwards. The angles ϕ and θ are the azimuthal and polar angles relative to the x and z axes, respectively. We also use as an angular variable the pseudorapidity defined by $\eta = -\ln[\tan(\theta/2)]$.

[24] R. Angstadt *et al.*, Nucl. Instrum. Methods Phys. Res., Sect. A **622,** 298 (2010).

[25] V. M. Abazov *et al.*, Nucl. Instrum. Methods Phys. Res., Sect. A **552,** 372 (2005).

[26] M. Abolins *et al.*, Nucl. Instrum. Methods Phys. Res., Sect. A **584,** 75 (2008).

[27] V. M. Abazov *et al.* (D0 Collaboration), Nucl. Instrum. Methods Phys. Res., Sect. A **737,** 281 (2014).

[28] T. Sjöstrand, P. Edén, C. Friberg, L. Lönnblad, G. Miu, S. Mrenna, and E. Norrbin, Comput. Phys. Commun. **135,** 238 (2001).

[29] T. Sjöstrand, S. Mrenna, and P. Skands, J. High Energy Phys. 05 (2006) 026.

[30] M. L. Mangano, M. Moretti, F. Piccinini, and M. Treccani, J. High Energy Phys. 01 (2007) 013.

[31] J. Campbell and R. K. Ellis, Nucl. Phys. B, Proc. Suppl. **10,** 205 (2010).

[32] E. Boos, V. Bunichev, M. Dubinin, L. Dudko, V. Edneral, V. Ilyin, A. Kryukov, V. Savrin, A. Semenov, and A. Sherstnev, Nucl. Instrum. Methods Phys. Res., Sect. A **534,** 250 (2004).

[33] J. Pumplin, D. R. Stump, J. Huston, H.-L. Lai, P. Nadolsky, and W.-K. Tung, J. High Energy Phys. 07 (2002) 012.

[34] V. M. Abazov *et al.* (D0 Collaboration), Phys. Rev. D **90,** 092006 (2014).

[35] CERN Application Software Group, CERN Program Library Long Writeup W5013, CERN, Geneva (1993).

[36] G. Blazey *et al.*, arXiv:hep-ex/0005012.

[37] V. M. Abazov *et al.* (D0 Collaboration), Nucl. Instrum. Methods Phys. Res., Sect. A **750**, 78 (2014).

[38] J. Smith, W. L. van Neerven, and J. A. M. Vermaseren, Phys. Rev. Lett. **50**, 1738 (1983).

[39] V. M. Abazov *et al.* (D0 Collaboration), Nucl. Instrum. Methods Phys. Res., Sect. A **763**, 290 (2014).

[40] P. Bärnreuther, M. Czakon, and A. Mitov, Phys. Rev. Lett. **109**, 132001 (2012).

[41] K. Kondo, J. Phys. Soc. Jpn. **57**, 4126 (1988).

[42] V. M. Abazov *et al.* (D0 Collaboration), Phys. Lett. B **617**, 1 (2005).

[43] T. Aaltonen *et al.* (CDF Collaboration), Phys. Rev. Lett. **103**, 092002 (2009).

[44] V. M. Abazov *et al.* (D0 Collaboration), Phys. Rev. Lett. **103**, 092001 (2009).

[45] Note the difference between x and y which denote detector and parton level quantities, while x, y, and z represent the geometrical axes defined in Ref. [23].

[46] G. Mahlon and S. J. Parke, Phys. Rev. D **53**, 4886 (1996).

[47] G. Mahlon and S. J. Parke, Phys. Lett. B **411**, 173 (1997).

[48] V. M. Abazov *et al.* (D0 Collaboration), Phys. Rev. D **74**, 092005 (2006).

[49] F. A. Berends, H. Kuijf, B. Tausk, and W. T. Giele, Nucl. Phys. **B357**, 32 (1991).

[50] V. M. Abazov *et al.* (D0 Collaboration), Phys. Rev. Lett. **103**, 141801 (2009).

[51] K. E. Atkinson, *An Introduction to Numerical Analysis* (Wiley, New York, 1989).

[52] J. Hammersley and D. Handscomb, *Monte Carlo Methods* (Methuen, London, 1964).

[53] W. Press *et al.*, *Numerical Recipes in Fortran 77: The Art of Scientific Computing*, 2nd ed. (Cambridge University Press, New York, 1992).

[54] O. Brandt, G. Guterrez, M. Wang, and Z. Ye, Nucl. Instrum. Methods, Sect. A **775**, 27 (2015).

[55] Throughout this document, we cite CPU hours for a single core of the XEON E5-2620 CPU with a clock rate of 2 GHz and a 64 bit computation.

[56] J. Bossert, M. Feindt, and U. Kerzel, Nucl. Instrum. Methods Phys. Res., Sect. A **559**, 232 (2006).

[57] P. Bratley and B. L. Fox, ACM Trans. Math. Softw. **14**, 88 (1988).

[58] I. Sobol, I.M. Sobol, Zh. Vychisl. Mat. Mat. Fiz. **7**, 784 (1967).

[59] T. Warnock, LA-UR-01-1950 (2001).

[60] D. Martin, W. J. Stirling, R. S. Thorne, and G. Watt, Eur. Phys. J. C **63**, 189 (2009).

[61] V. M. Abazov *et al.* (D0 Collaboration), Phys. Rev. D **84**, 012008 (2011).

[62] B. Abbott *et al.* (D0 Collaboration), Phys. Rev. D **58**, 052001 (1998), cf. Fig. 27.

[63] G. Corcella, I. Knowles, G. Marchesini, S. Moretti, K. Odagiri, P. Richardson, M. H. Seymour, and B. R. Webber, J. High Energy Phys. 01 (2001) 010.

[64] B. Cooper, J. Katzy, M. L. Mangano, A. Messina, L. Mijovic, and P. Skands, Eur. Phys. J. C **72**, 2078 (2012).

[65] V. M. Abazov *et al.* (D0 Collaboration), Phys. Rev. Lett. **106**, 122001 (2011).

[66] P. Nason, Presentation at the Top LHC WG meeting, (CERN, Geneva, 2014).

[67] P. Z. Skands, Phys. Rev. D **82**, 074018 (2010).P. Z. Skands, arXiv:1005.3457v4

[68] P. Z. Skands and S. Mrenna (private communication).

[69] P. Skands and D. Wicke, Eur. Phys. J. C **52**, 133 (2007).

[70] A. Buckley, H. Hoeth, H. Lacker, H. Schulz, and J. E von Seggern, Eur. Phys. J. C **65**, 331 (2010).

[71] M. G. Bowler, Z. Phys. C **11**, 169 (1981).

[72] Y. Peters, K. Hamacher, and D. Wicke, Fermilab-TM-2425-E (2006).

[73] G. Aad *et al.* (ATLAS Collaboration), arXiv:1503.05427.

[74] G. Aad *et al.* (CMS Collaboration), J. High Energy Phys. 12 (2012) 105.

[75] A. Abulencia *et al.* (CDF Collaboration), Phys. Rev. D **73**, 032003 (2006).